Stress and Microstructure Development in Particle-Based Coatings

A DISSERTATION
SUBMITTED TO THE FACULTY OF THE GRADUATE SCHOOL
OF THE UNIVERSITY OF MINNESOTA
BY

Kyle Kirk-Arthur Price

IN PARTIAL FULFILLMENT OF THE REQUIREMENTS
FOR THE DEGREE OF
DOCTOR OF PHILOSOPHY

Lorraine F. Francis and Alon V. McCormick, Advisors

September 2014

Acknowledgements

First, I would like to thank my advisors Lorraine Francis and Alon McCormick for their advice, guidance, and encouragement during my thesis research. I would also like to thank Kurt Wood and Wenjun Wu with Arkema, Inc. for their contributions and support throughout these projects. I would also like to gratefully acknowledge the National Science Foundation (NSF) GOALI program for financial support of this project under award number CBET 0967348. This work was partially supported by the NSF MRSEC and REU programs under Award Numbers DMR-0754792 and DMR-081988, respectively.

I would also like to thank the many members of the Francis Research group, and the Coatings Process Fundamentals Program (CPFP), both past and present, who have made my experience a great one. Special acknowledgements go to my colleagues: Bryce Williams, Yan Wu, Ankit Mahajan, Katie Crawford, Susanna Baesch, Derek Huang, Stephanie Kong, and Tuoqi Li, and "Jimmy" Bin Huang. Thank you for all of your support, advice, and friendship. I would also like to thank Chris Frethem for his assistance with cryoSEM, and Wieslaw Susynski for his experimental design expertise. They were both invaluable to my success throughout my research.

Finally, I would like to thank my family, without their love and support I would not be where I am today. To my Mother, who has always supported me and who instilled in me the values of hard work and dedication, I owe much of my success to you. To my wife, Maggie, you have been by my side throughout this journey offering your support and encouragement, for this I can't thank you enough. And to my sons, Bennett and Hudson, I wish you all the best in life and hope that you find success.

In loving memory of

Dr. D. W. Leckband

Abstract

Particle-based coatings have a wide range of uses and applications in everyday life. Stress development during the drying process has the potential to impact the performance of the coating. Stress development can be monitored *in-situ* using a cantilever deflection technique with a laser-photodiode combination. Stress development in the film is directly related to the development of the coating microstructure during drying. Cryogenic scanning electron microscopy (cryoSEM) is a powerful characterization method capable of visualizing the microstructure of the coating during the intermediate stages of drying. Using this method, the coating is frozen to arrest microstructure development and solidify the sample so that it can survive the high-vacuum environment of the SEM.

This thesis explores the connections between stress and microstructure development in particle-based coatings during drying. Characterization is often complicated by lateral drying, a common phenomenon in particle-based coatings. To avoid these complications, walled substrates were developed which are used to suppress lateral drying and promote drying uniformity. CryoSEM revealed that latex coatings dried on substrates (with photoresist walls) exhibit a greater degree of drying uniformity. Silicon cantilevers with poly(dimethyl siloxane) (PDMS) walls along the perimeter were used to suppress the effects of lateral drying during stress measurement. The walled cantilevers were used to characterize stress development in ceramic particle coatings and latex films. For the ceramic particle coatings, stress measurements were combined with cryoSEM revealing the origins of stress development in hard particle coatings. Stress development was correlated with the extent of drying and the degree of saturation in the coating. Stress development in latex particle coatings was influenced by the composition and morphology of the latex particles. Additionally, the influence of coalescing aids on stress development was also investigated. The film formation behavior was studied using a variety of techniques including AFM, cryoSEM, and minimum film formation temperature (MFFT) measurements.

Table of Contents

LIST OF TABLES vii

LIST OF FIGURES ix

CHAPTER 1: Introduction

1.1 *Motivation* 1

1.2 *Thesis Outline* 3

CHAPTER 2: Background Information

2.1 *Introduction* 6

2.2 *General Theory of Drying* 7

2.3 *Latex Film Formation* 11

2.4 *Lateral Drying* 16

2.5 *Stress Development* 19

2.6 *Summary* 21

CHAPTER 3: Experimental Methods

3.1 *Introduction* 22

3.2 *Minimum Film Formation Temperature Bar* 23

3.3 *Stress Measurement*

3.3.1 *Theory: Cantilever Bending Technique* 26

3.3.2 *Stress Measurement Apparatus* 28

3.3.3 *Calibration* 31

3.3.4 *Weight Loss Correction* 32

3.4 *Cryogenic Scanning Electron Microscopy*

3.4.1 *Scanning Electron Microscopy (SEM)* 33

3.4.2 *Cryogenic Scanning Electron Microscopy* 34

3.4.3 *Artifacts of CryoSEM Sample Preparation*.....37

3.5 *Summary* 43

CHAPTER 4: Walled Substrates And Drying Uniformity

4.1 *Background and Motivation* 44
4.2 *Materials and Methods*
4.2.1 Latex 46
4.2.2 Substrates 47
4.2.3 Digital Microscopy - Hirox 48
4.2.4 CryoSEM 48
4.3 *Experimental Results*
4.3.1 *Appearance of Drying Coatings* 50
4.3.2 *Microstructure Development: Non-walled Substrate* 52
4.3.2 Microstructure Development: Walled Substrate (Filled) 56
4.3.3 Microstructure Development: Overfilled Walled Substrate 59
4.3.4 Fully Dried Coatings 61
4.4 *Discussion*
4.4.1 Non-walled Substrates 63
4.4.2 Walled Substrates 67
4.5 *Summary* 70
CHAPTER 5: Stress Development in Hard Particle Coatings
5.1 *Background and Motivation* 71
5.2 *Materials and Methods*
5.2.1 Ceramic Particle Suspensions 76
5.2.2 Stress Measurement 77
5.2.3 Microstructure Characterization 80
5.3 *Results and Discussion*
5.3.1 Walled Cantilevers and the Corcoran Equation 81
5.3.2 *Drying and Stress in Alumina Particle Coatings* 84
5.3.3 *Microstructure and Stress Development* 93
5.3.4 *Origins of Stress Development* 103
5.4 *Summary* 107
CHAPTER 6: Stress Development in Latex Particle Coatings
6.1 *Background and Motivation* 108

6.2 *Materials and Methods*
6.2.1 *Acrylic Latex* 112
6.2.2 *PVDF:Acrylic Latex* 113
6.2.3 *Stress Measurement* 114
6.2.4 *Minimum Film Formation Temperature (MFFT) Measurement* ...115
6.3 *Results and Discussion*
6.3.1 *Acrylic Latexes* 115
6.3.2 *PVDF:Acrylic Blends* 122
6.4 *Summary* 129
CHAPTER 7: Stress Development and Film Formation for Core-Shell Latex Coatings
7.1 *Background and Motivation* 131
7.2 *Materials and Methods*
7.2.1 *Core-shell Latex* 135
7.2.2 *Stress Measurement* 136
7.2.3 *Microstructure Characterization Methods* 137
7.2.4 *Paint Properties* 139
7.2.5 *Paint Performance Tests* 140
7.3 *Results and Discussion*
7.3.1 *Core-Shell Particle Morphology* 142
7.3.2 *Film Formation* 144
7.3.3 Stress Development 152
7.3.4 *Paint Performance* 159
7.4 *Summary* 162
CHAPTER 8: Summary and Future Considerations
8.1 *Summary*....164
8.2 *Future Considerations*
8.2.1 *Crack Development and Fracture Toughness in Coatings*....165
8.2.2 *Stress Development in Multi-Layer Coatings*....166
REFERENCES 168
APPENDIX 179

List of Tables

Table 6.1: Sample Characteristics for Acrylic Latexes 113

Table 6.2: Properties of PVDF:Acrylic Blends 114

Table 6.3 Characteristics of Coalescing Aids 121

Table 7.1: Sample characteristics for soft-core/hard-shell latex 136

Table 7.2. High Gloss Paint Formulation 140

Table 7.3 MFFT and AFM Roughness Data 151

Table 7.4 Paint Performance Data 160

Table A.1 Finite Element Analysis Data 183

List of Figures

Figure 2.1 Schematic diagram of particle distributions in particle-based coatings during drying. 8

Figure 2.2 Schematic diagram of particle consolidation during drying. 9

Figure 2.3 Schematic diagram of the latex film formation process. 12

Figure 2.4 Representations of possible deformation mechanisms during latex film formation. 13

Figure 2.5 (a) Visual appearance of a latex particle coating (50:50 PVDF:acrylic) drying on a 5 x 7 mm silicon substrate. (b) Photograph of a "coffee ring" deposit formed during lateral drying. 17

Figure 2.6 Diagram of the lateral drying process for a particle-based coating. 18

Figure 2.7 Schematic diagram of a coating element on a substrate. 20

Figure 3.1 Photograph of the minimum film formation temperature bar, MFFT90 (Rhopoint). A PET film covers the metal temperature gradient bar, which is cooler on the left side and warmer on the right. A latex coating has been fully dried, and the cloudy-clear transition is clearly visible. 25

Figure 3.2 Schematic diagrams of the side view and cross-sectional view of the stress measurement apparatus used in this work to monitor stress development in coating during drying. 29

Figure 3.3 Photograph of the calibration step (left) and a schematic representation of the calibration bar designed to improve accuracy and reproducibility of the calibration step. 30

Figure 3.4 Schematic diagrams showing the deflection of a cantilever under a point load (left) and a bending moment (right). 31

Figure 3.5 The plunge freezing technique used to prepare partially dried samples for cryoSEM imaging involves five steps. I) A coating is applied to the substrate and undergoes a period of drying. II) The sample is plunged into a bath of liquid ethane, which is surrounded by liquid nitrogen. III) Samples are fractured in a high vacuum condition to expose the cross-section of the coating. IV) A thin layer of platinum (~ 5 nm) is sputter coated onto the fracture surface. V) The samples are moved to the microscope and imaged at cryogenic temperatures. 35

Figure 3.6 CryoSEM micrographs of a sample where poor freezing resulted in ice crystal growth and particle rearrangement in the frozen sample. Particle free, and particle rich zones are clearly evident throughout the sample. 38

Figure 3.7 CryoSEM micrographs showing the different appearance of frost contamination on the frozen sample surface. (a) hexagonal ice crystal on the sample surface (b) speckled frost "decoration" covering the fracture surface (c) directional frost "blanketing" and speckled frost "decoration". 40

Figure 3.8 a) CryoSEM micrographs showing the formation of pullouts from a frozen dispersion of latex particles. The "hairy" structure on the pullouts is believed to be a form of ice contamination. b) CryoSEM image of latex particle "pullouts" that have been revealed through sublimation of the frozen water matrix. 42

Figure 4.1 Left: Cross-section of an SU-8 wall on a silicon substrate taken by conventional SEM; in this image the edge of the substrate on the right side. Right: A schematic diagram showing the dimensions of the walled substrates. 48

Figure 4.2 Schematic diagram showing the substrate geometries used in this study: non-walled, walled (filled), and overfilled. 49

Figure 4.3 Digital micrographs of latex coatings during at (a) 2 min, (b) 7 min, (c) 9 min, and (d) 11 min of drying in ambient conditions. For each, the sample on the left is a non-walled silicon substrate (5 mm x 7 mm) and the sample on the right is a walled substrate (filled). 51

Figure 4.4 CryoSEM images of a latex coating prepared on a non-walled silicon substrate and frozen after seven minutes of drying. The low magnification image (a) shows the region of the coating near the edge of the substrate. The higher magnifications images (b) & (c) show the boundary between the suspended region and the consolidated packing (dashed line). 53

Figure 4.5 CryoSEM cross-sections of a latex coating prepared on a non-walled substrate frozen after 12 minutes of drying. The lower magnification image (a) shows the shape of the free surface. The higher magnification image (b) shows the packing front. 55

Figure 4.6 CryoSEM cross-section of a filled walled substrate dried for one minute. During fracture the wall detached from the substrate and is missing from the right side of the images. 57

Figure 4.7 CryoSEM cross-section of a walled substrate (filled) frozen after 12 minutes of drying. The lower magnification image (a) shows the pinned contact line and the concave shape of the free surface. The consolidation of particles near the wall is shown in greater detail in (b). 58

Figure 4.8 CryoSEM cross-sections of a coating prepared on an overfilled walled substrate frozen after 12 minutes of drying. The low magnification image (a) shows the convex shape of the free surface. Greater detail of the coating microstructure near the wall is shown in (b). 59

Figure 4.9 CryoSEM cross-section of an overfilled walled substrate frozen after 25 minutes of drying. The lower magnification image (a) shows the shape of the free surface in the later stages of drying. The higher magnification image (b) shows the detail of the coating microstructure. 60

Figure 4.10 Room temperature SEM cross-sections near the edge of fully dried coatings for the a) non-walled substrate, b) filled walled substrate, and c) overfilled walled substrate. 62

Figure 4.11 Schematic representations of the microstructure development for a latex coating for the three drying geometries: non-walled substrate, walled substrate (filled) , and overfilled walled. The point of contact between the packed region (grey) and the wall is shown at a right angle but was shown experimentally to vary. The intersection of the packed region with the substrate establishes the curved interface as represented. 63

Figure 4.12 Schematic diagram of contact line pinning (circles) and flow within the coating marked by solid lines for coating dried no non-walled substrates and walled substrates. 68

Figure 5.1 a) Plots for the stress development of an aqueous latex coating prepared on a standard cantilever and a cantilever with photoresist walls. b) Plot showing the displacement measured on the photodiode for only water deposited on a cantilever with photoresist walls. 78

Figure 5.2 a) Schematic diagram showing the fabrication procedure for the silicon cantilevers with PDMS walls. b) Schematic top-view of the walled cantilevers showing the dimensions of the cantilever and location of the PDMS walls. c) Photograph showing the semi-circular cross-section of the PDMS wall on the silicon cantilever. 79

Figure 5.3 (a) Schematic diagrams for the three conditions simulated using finite element analysis (b) Simulation results plotting the ratio of the deflection of the reduced area coatings (with and without PDMS walls) to the deflection of the fully coated cantilever as a function of wall width. 83

Figure 5.4 Top: Photographs a)-f) show an alumina coating dried on a silicon cantilever without walls after drying for a) 5 minutes, b) 15 minutes, c) 20 minutes, d) 27 minutes, e) 27 minutes 30 seconds, and f) 35 minutes. The black background was added for clarity. Bottom: Stress development curve for the alumina coating, the corresponding images marked on the plot. 86

Figure 5.5 Top: Photographs a)-f) show an alumina coating dried on a silicon cantilever with PDMS walls after drying for a) 20 minutes, b) 26 minutes, c) 28 minutes, d) 30 minutes, e) 32 minutes, and f) 40 minutes. The black background was added for clarity. Bottom: Stress development curve for the alumina coating is also shown, the corresponding images marked on the plot. 88

Figure 5.6 Fully dried cross-section of an alumina particle coating dried on a walled cantilever showing localized thickness non-uniformity near the wall. 90

Figure 5.7 a) Stress development curves for alumina particle coatings dried on a) standard cantilevers, and b) walled cantilevers of varying width. 92

Figure 5.8 CryoSEM cross-sectional micrographs of alumina particle coatings dried on walled cantilevers for a) 7 minutes and b) 30 minutes. 94

Figure 5.9 Top: Photographs a)-f) show a silica coating dried on a silicon cantilever with PDMS walls after drying for a) 10 minutes, b) 15 minutes, c) 18 minutes, d) 20 minutes, e) 22 minutes, and f) 27 minutes. The black background was added for clarity. Bottom: Stress development curve for the alumina coating is also shown, the corresponding images marked on the plot. 96

Figure 5.10 CryoSEM cross-sectional images for a silica particle coating dried for 1-minute. a) Low magnification view of the cross-section showing particle distribution in the film. b) Particle consolidation along the free surface. c) Uniform particle distribution below the consolidated region. 98

Figure 5.11 CryoSEM cross-sectional images for a silica particle coating dried for 14 minutes. a) Low magnification view of the cross-section showing uniform saturation throughout the coating thickness. b) Curved menisci formed between adjacent particles along the free surface c) Uniform saturation in the consolidated particle packing below the free surface. 99

Figure 5.12 CryoSEM cross-sectional images for a silica particle coating dried for 17 minutes. a) Low magnification view of the cross-section showing fingers of air penetrating throughout the coating thickness. b) Air invasion in the particle packing near the free surface c) Air invasion in the particle packing halfway through the coating thickness. 100

Figure 5.13 CryoSEM cross-sectional images for a silica particle coating dried for 20 minutes. a) Low magnification view of the cross-section showing the distribution of pendular rings of water in the particle packing b) high magnification image of the pendular rings formed between adjacent silica particles. 101

Figure 6.1 Stress development for latex coatings with varying MFFT without coalescing aids. MBA31 and MBA43 form continuous films upon drying at room temperature, whereas MBA1 cracks upon drying. 118

Figure 6.2 Effectiveness of various coalescing aids at lowering the MFFT for MBA43 at a concentration of 3% on the final solids in the coating. Dashed line represents the MFFT of the latex with no coalescing aid. 122

Figure 6.3 Stress development curves for the MBA43 sample (MFFT = 18°C) with various coalescing aids at 3% concentration in the final film. 122

Figure 6.4 Shows the influence of the concentration of a) Texanol™ and b) Optifilm 400 on the stress development in the coating. 123

Figure 6.5 Plot showing the MFFT for blends of the PVDF:acrylic latexes (50:50 and 70:30), compared with mixtures of 70:30 PVDF:acrylic particles with pure acrylic particles. 126

Figure 6.6 Stress development curves for a) the 50:50 and 70:30 PVDF:acrylic latexes, and b) for the 70:30 PVDF latex (with and without Texanol™). 128

Figure 7.1 Room temperature BSE images of (a) BL25 particles stained in solution for 20 minutes and dried on an SEM stub (b) a stained fracture surface from an AL25 film aged for 1 week, and (c) a stained fracture surface from a CL50 film aged for 1 week. 144

Figure 7.2 CryoSEM cross-sectional images CL50 dried in ambient conditions for (a) 8 min (b) 18 min (c) 5 hrs and BL25 dried for (d) 10 min (e) 20 min (f) 5 hrs. The white arrows in (b) and (e) mark the position of frozen water that filled the space between the particles. 147

Figure 7.3 Topographic AFM images, obtained in contact mode, of (a) AL25, (b) AL35, and (c) AL50. For a low shell ratio, individual particles become less discernable and the surface becomes smoother. Each image is 4 μm x 4μm. 149

Figure 7.4 Topographical AFM images, obtained in contact mode, of (a) AL25, (b) AS25, (c) CL50, and (d) CS50, illustrate the influence of particle size on the film roughness. Each image is 4 μm x 4μm. 151

Figure 7.5 Stress development and weight loss data for coatings of AL25 dried at 22°C and 40% RH. The dried thickness of the coating was approximately 80 μm. 153

Figure 7.6 (a) Photographs of the films formed from the AL25 and AL50 latex samples. (b) Effect of shell ratio on the stress development profile for AL25, a film forming latex, and AL50, a non-film forming latex. The dried thicknesses of the films are approximately 80 μm. 155

Figure 7.7: Effect of ΔT_g on the stress development profile for AL25 and BL25. BL25 has a smaller ΔT_g compared to AL25. The dried thicknesses of the films are approximately 80 μm. 158

Figure 7.8 Effect of particle size on the stress profiles for AL25 and AS25. AL25 and AS25 have D_v=146 nm and D_v= 63 nm, respectively. The dried thicknesses of the coatings are approximately 80 μm. 159

Figure A.1 Deflection in a composite beam due to stress in a coating. Cross-sections show the area of the coating with and without walls. 180

Chapter 1

INTRODUCTION

1.1 *Motivation*

Coatings are ubiquitous in everyday life and are used in variety of industries to alter the surface properties or characteristics of the underlying substrate. Coatings typically serve a critical design purpose, such as protection of the substrate from scratches or corrosion like paints or varnishes,[1,2] providing engineered optical properties like anti-reflection coatings,[3] or delivering specific functionality to a product like magnetic coatings for storage media[4] or drug-release coatings.[5] The complexity of these coatings can vary from simple single layer systems (e.g. latex paints) to complex multi-layered coatings systems (e.g. automotive refinish systems). Engineering coatings that perform specific functions requires an understanding of how the coating is formulated, how it is applied to the substrate, and the process in which the coating undergoes solidification.

Many industrial coatings are particle-based, which contain particles ranging in size from a few nanometers to tens of microns. Particle-based coatings generally have three main components, the solvent, the particles, and additives. The solvent may be

either organic or aqueous and is used to suspend the particles and to facilitate the application of the particle suspension onto the substrate. The particles may be inorganic (ceramics or metals) or organic (latex particles), or a combination of both. For example, architectural paints contain insoluble polymer particles (latex) that act as a binder, as well as inorganic pigment particles that provide hiding and color to the final film.[1] Finally, many coatings also contain additives like plasticizers, rheology modifiers, surfactants, defoamers, and biocides that play specific functions in the coating.

Particle-based coatings are typically applied to the substrate in liquid form and allowed to dry (or solidify), forming the final coating. Drying is a critical process that influences the coating microstructure and ultimately affects the performance of the coating. During drying, stress develops in the coating that has the potential to initiate coating defects like cracking, curling, warping, wrinkling, and delamination. One of the main objectives of this thesis is to investigate how stress development is connected to the coating microstructure. If these complex relationships are well understood, coatings systems can be engineered that are more robust and more resistant to defects like cracking.

To monitor stress development *in-situ,* a stress measurement apparatus based on the cantilever deflection technique was developed by past researchers at the University of Minnesota. This apparatus and has been used to investigate stress development for a variety of coatings systems.[6–9] Results from these studies have advanced the understanding of stress development for drying and curing coatings. Researchers at the University of Minnesota have also pioneered the use of cryogenic scanning electron

microscopy (cryoSEM) as a tool for investigating microstructure development during drying. CryoSEM is a powerful characterization tool that allows visualization of the transient stages of microstructure development that occur while the coating is still wet. This is accomplished by freezing the samples at various extents of drying, and imaging the coatings in an SEM. This method provides high-resolution snapshots of the microstructure development in the coating. Past researchers have used cryoSEM to investigate many complex phenomena including latex film formation,[10–12] freeze-thaw stability,[13] particle distributions,[14,15] and cracking.[16]

1.2 *Thesis Outline*

The results presented in this thesis build upon the work of previous researchers and advance the understanding of stress and microstructure development in particle-based coatings. This was accomplished by combining measurements of stress development with microstructure characterization using a variety of techniques. Chapter 2 provides some of the essential background information needed to understand the drying process, latex film formation, and stress development. Chapter 3 gives an overview of some of the unique characterization methods and experimental techniques used in this research.

In this research, stress development was monitored using a cantilever deflection technique. A major limitation of this technique is that only an average stress may be calculated from a measurement of the cantilever deflection. Particle-based coatings often dry non-uniformly, which results in non-uniform stress development across the cantilever. Non-uniform drying complicates the interpretation of stress measurements

made using the cantilever deflection technique. To avoid these complications, a uniform drying condition is desired. To achieve this, walled cantilevers were developed that suppress lateral drying, and allow measurements of coating stress without these complications. CryoSEM was used to monitor the microstructure development of latex coatings dried on walled substrates with photoresist walls. The results are discussed in Chapter 4. CryoSEM revealed that the use of walled substrates limits lateral drying and results in more uniform coatings. However, contact line pinning at the wall resulted in localized thickness non-uniformities near the wall.

Chapter 5 discusses stress development in hard particle coatings. Stress measurements were made with standard cantilevers and cantilevers modified with poly(dimethyl siloxane) (PDMS) walls. The walled cantilevers suppress lateral drying and provide a more uniform drying condition. In the case of extreme uniformity, stress developed sharply when the coating reached a critical extent of drying followed by a gradual decay in stress as the coating continued to dry. CryoSEM was used to image the coating microstructure during the intermediate stages of drying. Combining stress measurements (using walled cantilevers) and cryoSEM characterization, the mechanism of stress development for hard particle coatings was revealed.

Chapters 6 and 7 discuss the film formation behavior and stress development of latex particle coatings. In Chapter 6, the stress development for latex particle coatings was studied as a function of particle composition. The addition of coalescing aids on the film formation behavior and the stress development was also investigated in Chapter 6. Similarly, Chapter 7 investigates the influence of a core-shell particle morphology on the

ability of latex particles to undergo film formation and the stress development in the film. Results show that film formation was enhanced for particles with thin shells, small particle sizes, and similar glass transition temperatures for the core and shell polymers. The core-shell latex particles were also prepared in a practical paint formulation to study the performance of the corresponding coatings. The performance results for the paints were correlated to the film formation behavior and the stress measurement results for the latex-only coatings. Finally, Chapter 8 offers some possible directions for future research.

Chapter 2

BACKGROUND INFORMATION

2.1 *Introduction*

Drying is a critical processing step for particle-based coatings. For example, in ceramic particle coatings, the drying process influences the green density (microstructure) of the ceramic film, which impacts the final fired product.[17] Likewise, for latex particle coatings, the removal of water is one of the driving forces for latex film formation.[1,18] The drying process can also generate concentration gradients in the drying film, which is a major problem in paper coatings[19] and battery electrode manufacturing[20]. In these examples, "binder migration" during drying results in a binder rich layer along the free surface and a depletion of binder near the substrate causing poor adhesion of the coating to the substrate. Achieving optimal performance from particle-based coatings requires an understanding of the drying process and how it impacts the microstructure of the film.

Section 2.2 describes a general theory of the drying process for particle-based coatings. Although the drying process is similar for all particle-based coatings, soft latex particles undergo a process known as film formation, which is described in Section 2.3.

Furthermore, particle-based coatings often dry non-uniformly from the edges inward; Section 2.4 explains the origin and formation of lateral drying fronts. Finally, Section 2.5 describes the process of stress development in coatings undergoing solidification (drying, curing, etc.). Throughout this chapter, the liquid phase of the particle suspensions is assumed to be water, which is often the case; however, analogies can be made for other solvents.

2.2 *General Theory of Drying*

Immediately after a liquid coating is spread onto the substrate, evaporation begins. With evaporation, the free surface of the coating descends toward the substrate with a velocity set by the evaporation rate, $\dot{E}$. Beneath the free surface, the suspended particles exhibit Brownian motion. For monodisperse spherical particles, the Stokes-Einstein diffusion coefficient, D_o, estimates the diffusion coefficient for particles with radius R, in a fluid with viscosity μ, at a temperature T, the Boltzmann constant is k:

$$D_o = \frac{kT}{6\pi\mu R} \tag{2.1}$$

As the free surface descends, it encounters particles that can either diffuse away from the free surface, or become trapped forming what is termed a "consolidation front". The dimensionless Peclet number, Pe, can be used to predict whether or not a consolidation front is likely to form. The Peclet number balances the rate of particle diffusion, D_o, with the evaporation rate, $\dot{E}$, for a coating with an initial thickness of H_o:[15,21]

$$Pe = \frac{H\dot{E}}{D_o} = \frac{6\pi\eta R_o H\dot{E}}{kT} \tag{2.2}$$

When the evaporation rate is much faster than the diffusion rate, $Pe >> 1$, particles may accumulate along the free surface. Likewise, if the diffusion rate is high compared to the evaporation rate, $Pe << 1$, the particles will tend to diffuse away from the free surface and maintain a uniform particle concentration. These two conditions are shown schematically in Figure 2.1. Consolidation fronts along the free surface have been shown to promote ordering in drying colloidal dispersions.[22] Consolidation fronts can also form along the edges of a coating in a phenomenon commonly known as lateral drying. Non-uniform drying will be discussed in greater detail in Section 2.4

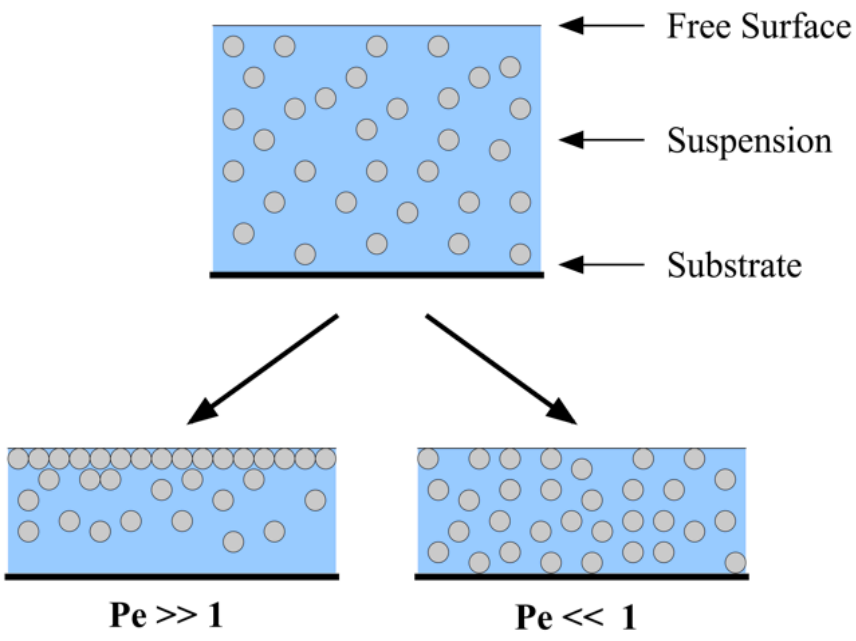

Figure 2.1 Schematic diagram of particle distributions in particle-based coatings during drying.

With further evaporation, the volume of the coating continues to shrink and the average distance between particles in the coating decreases. Eventually the particles come into touching contact and form a close-packed network, this process is known as consolidation. Assuming no particle concentration gradients form during drying, the consolidation process is shown schematically in Figure 2.2.

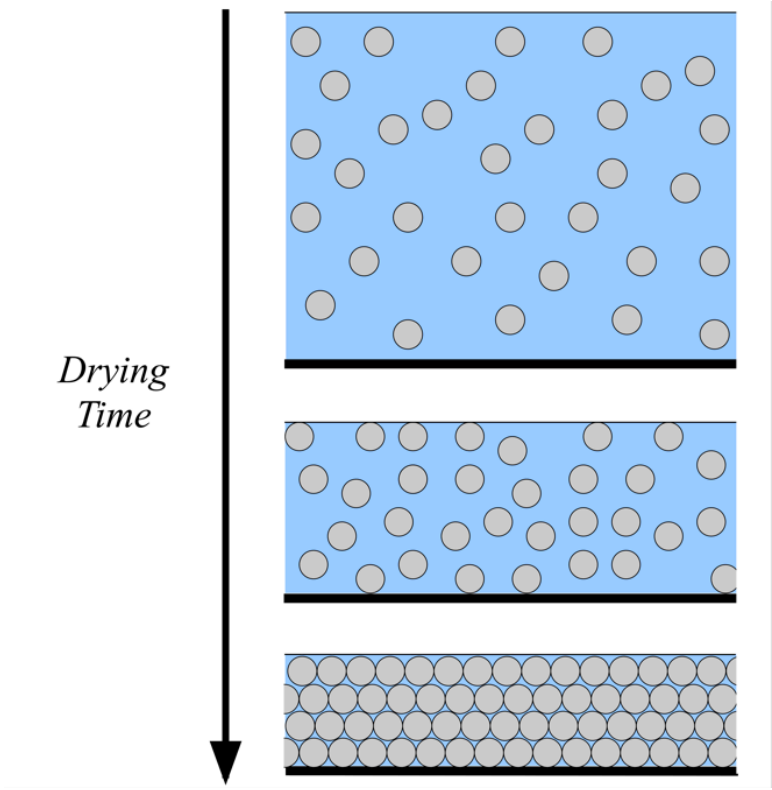

Figure 2.2 Schematic diagram of particle consolidation during drying.

After consolidation, water continues to evaporate from the saturated particle network. At the free surface, the volume of water lost to evaporation must be replenished or the free surface must descend into the particle packing. The recession of the free surface would raise the energy of the system because $\gamma_{solid\text{-}vapor} > \gamma_{solid\text{-}liquid}$, where γ represents the surface energy.[23] Hence, to avoid entering the porespace, and to avoid

exposing the solid surface, the air-water interface becomes curved. The pressure drop across the curved interface can be estimated with the Young-LaPlace equation:[24]

$$P_{liq} - P_{gas} = \frac{2\gamma}{R}\cos(\theta) \tag{2.3}$$

where P represents the pressure, γ is the surface tension, θ is the contact angle, and R is radius of curvature of the meniscus. Assuming the water wets the particle surface, the curvature of the menisci results in a lower pressure below the menisci, which generates a flow of water in the coating despite the resistance to flow imposed by the porespace.[23,25]

If the resistance to flow is balanced by the pressure gradient, the flow will be sufficient to maintain the curvature of the meniscus. However, if they are not balanced, the curvature of the meniscus will increase (in order to increase the driving force for flow) and the interface descends into the porespace.[25] The maximum curvature of the meniscus will depend on the size and geometry of the pores. When curvature of the menisci becomes too high (smaller R), the meniscus moves to a new location in the porespace that allows a larger curvature. This process is commonly known as a Haine's jump.[26] After the Haine's jump, the water beneath the meniscus redistributes, equalizing the pressure in that region. As the coating continues to dry, this process is repeated and the remaining water is removed from the porespace.

In the later stages of drying, the residual water in the coating forms pendular rings that bridge adjacent particles.[27,28] These pendular rings hold the coating together and give the film mechanical strength. Lampenscherf et al.[27] used ESEM to image pendular rings of water between large spherical particles. They found that the size of the pendular

rings was depended on the relative humidity. For coatings made of hard particles, a small amount of water is expected to remain in the coating in the form of pendular rings.

The description of drying presented here assumes that the particles are uniform elastic spheres; however, in practice the particles may be non-uniform in shape and have a variety of mechanical properties. For soft particle coatings, like the polymer particles used in latex coatings, the particles are soft enough to deform under the forces present in the coating during drying. For latex coatings, this process is known as latex film formation.

2.3 *Latex Film Formation*

Latex film formation is generally described as having three main stages: consolidation, compaction, and coalescence.[1,2,29,30] A schematic representation of the film formation process is shown in Figure 2.3. The consolidation stage begins as soon as the suspension is deposited and water begins evaporating. The consolidation process for latex particles is analogous to the general process described in Section 2.1 for particle-based coatings. The consolidation stage continues until the particles form a close packed particle network.

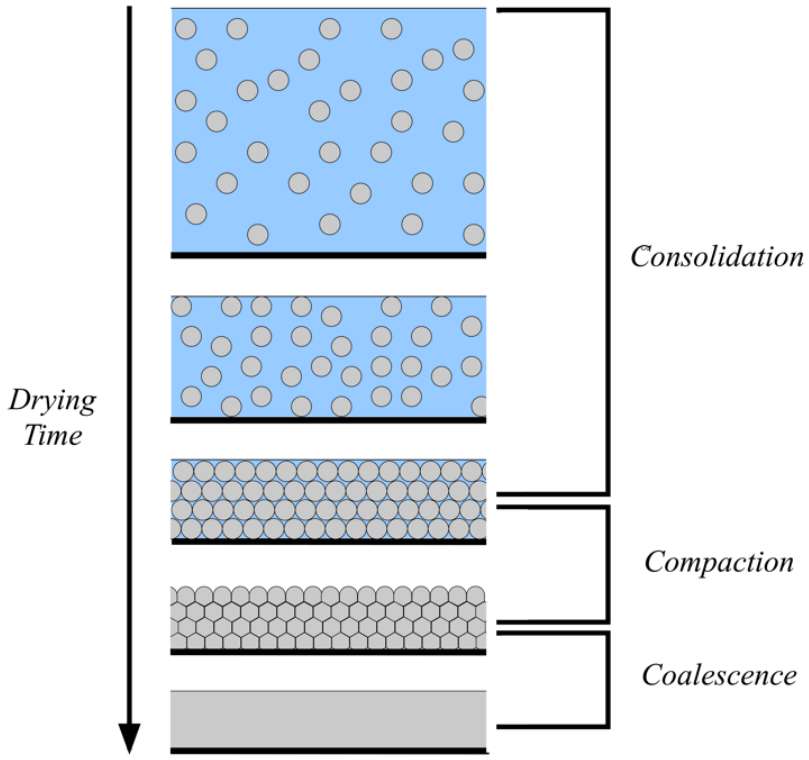

Figure 2.3 Schematic diagram of the latex film formation process.

After consolidation, the compaction stage begins as forces develop in the film, which are capable of causing particle deformation. For hard particle coatings, these forces are not sufficient to deform the particles, and air invasion into the coating is likely to occur. However, soft latex particles can deform under these forces and film the void space in the particle packing. A number of possible driving forces for particle deformation have been proposed including wet sintering,[31] dry sintering,[32] capillary deformation,[18] Sheetz deformation,[33] and even compaction due to van der Waals forces.[12] The most common deformation mechanisms are represented schematically in Figure 2.4.

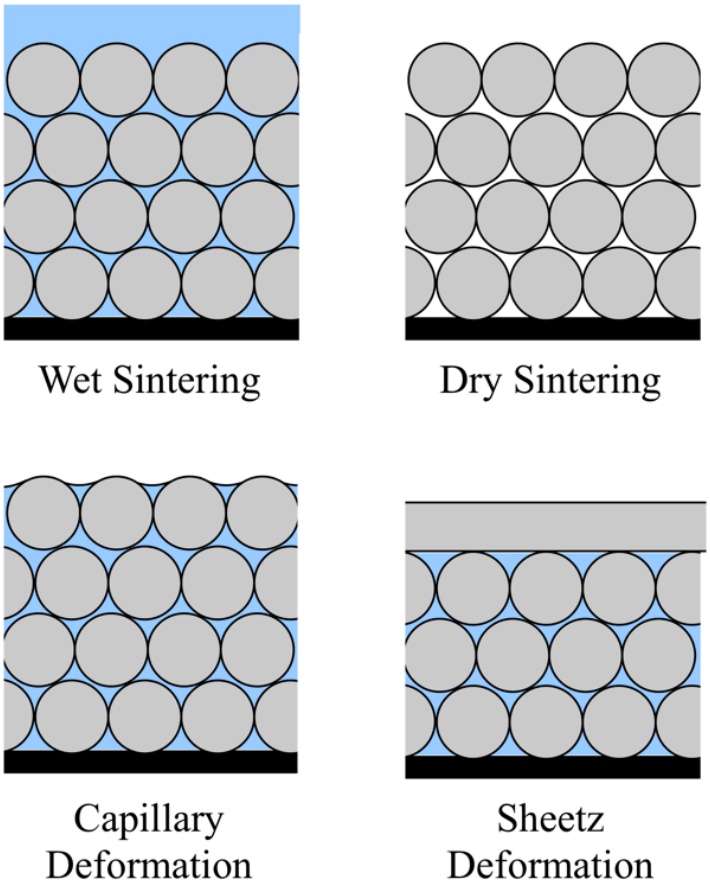

Figure 2.4 Representations of possible deformation mechanisms during latex film formation.

Vanderhoff et al.[31] were the first to propose the wet sintering mechanism of particle deformation. In this mechanism, the interfacial tension between the polymer particles and the water, $\gamma_{p\text{-}w}$, is the dominant driving force for particle deformation. When two latex particles touch, the interfacial area between them is eliminated; this situation is comparable to the coalescence of oil droplets in water. Here, particle deformation occurs while the coating is still saturated with water. The mechanism of wet sintering has been shown experimentally by Eckersley and Rudin,[34] Sheetz,[33] and later by Dobler et al.[35]

The mechanism of dry sintering is analogous to wet sintering except that the driving force for particle deformation is the polymer-air interfacial tension, $\gamma_{p\text{-}a}$. This mechanism or deformation for latex particles was first proposed by Dillon et al.[32] Using a minimum film formation temperature (MFFT) bar, Sperry et al.[36] showed experimentally that a wet film and a pre-dried film (containing the same latex particles) would have the same cloudy-clear transition when placed onto an MFFT bar, regardless of the water content. At least for the acrylic latexes used in their studies, the polymer-air interfacial tension was sufficient to deform the particles and form a clear, crack-free film.

Similarly, Gong et al.[12] showed that van der Waals forces alone could cause particle deformation. In these experiments, a latex suspension was frozen and freeze-dried to create a "bone-dry" particle film that saw no capillary forces. Under vacuum, the freeze-dried films were annealed at various temperatures and the extent of particle deformations were characterized with room temperature SEM. The results show that, at least for some latex systems, attractive van der Waals forces can be sufficient to cause particle deformation.

Brown[18] was the first to propose the capillary mode of deformation during latex film formation. In this mechanism, the driving force for particle deformation is the capillary pressure, due to curvature of liquid-air interface. In his work, Brown[18] derived a criterion for particle deformation by balancing the capillary pressure with the elastic response of the particles, based on shear modulus, *G*. From this relationship, particle deformation is expected when:

$$G < A\frac{\gamma_{wa}}{R} \tag{2.4}$$

for particles with radius R and a multiplier A = 35. Several other authors have developed similar relationships with slightly different limits, with the multiplier A ranging from 30 to 300.[37,38] The role of capillary forces during latex film formation were discussed in detail in the work by Pekurovsky and Scriven.[28]

The final deformation discussed here is Sheetz deformation. Sheetz[33] noted a polymer skin often forms during drying, which surrounds the fluid suspension beneath. In his original argument, Sheetz hypothesized that diffusion of water through the polymer film would produce a compressive force on the film below. However, many researchers find it more likely that the polymer film significantly slows the evaporation rate, giving the particles sufficient time to deform by wet sintering.[1] Vertical inhomogeneity in film formation has important implications on the final microstructure of the coating, so Sheetz deformation is generally reserved as a separate deformation mechanism.

All of the deformation mechanisms outlined above can be observed in latex films and occur under different experimental conditions. The rate of evaporation, which dictates the total drying time of the coating, and the drying temperature, which controls the viscous response of the polymer, are the easiest process parameters to control experimentally. Routh and Russel[39] developed a deformation map which predicts the mechanism of particle deformation based on the mechanical properties of the particles and the drying conditions. Their deformation map, which includes all the deformation mechanisms outlined above (except for van der Waals deformation), has been verified experimentally for different latex coatings.[40,41]

Regardless of the dominant deformation mechanism, once intimate contact is achieved between adjacent latex particles, polymer chains begin to diffuse across particle boundaries in a process known as coalescence. During coalescence, the film gains mechanical strength and toughness as the particle boundaries become less distinguishable and the film becomes more homogeneous. The degree of interdiffusion and coalescence in a latex film is dependent of the molecular weight of the polymer, the degree of branching of the polymer chains, the drying temperature, latex particle size, and morphology of the latex particles.[1]

2.4 Lateral Drying

A common observation of particle-based coatings is that they do not dry uniformly.[42–44] Instead there are often visually identifiable fronts that pass laterally across the film as it dries. Changes in the appearance of the coating (translucent, clear, turbid, opaque, etc.) arise due to variations in the coating microstructure that affect the efficiency of light scattering from the film.[43] For example, the appearance of latex coatings changes from turbid and opaque after deposition to clear and transparent when the film is dry, see Figure 2.5 The lateral propagation of drying fronts, normally identified from the visual appearance, is commonly referred to as lateral drying. Lateral drying can also be identified by the formation of thick edges, or deposits near the edge of a coating or drying drop. A common example of lateral drying is the formation of "coffee rings", where suspended particles are deposited at the edge of a drying drop, forming a familiar dark ring left behind when a drop of coffee or wine dries, see Fig 2.5b. The "coffee ring" effect was first described by Deegan et al.[42]

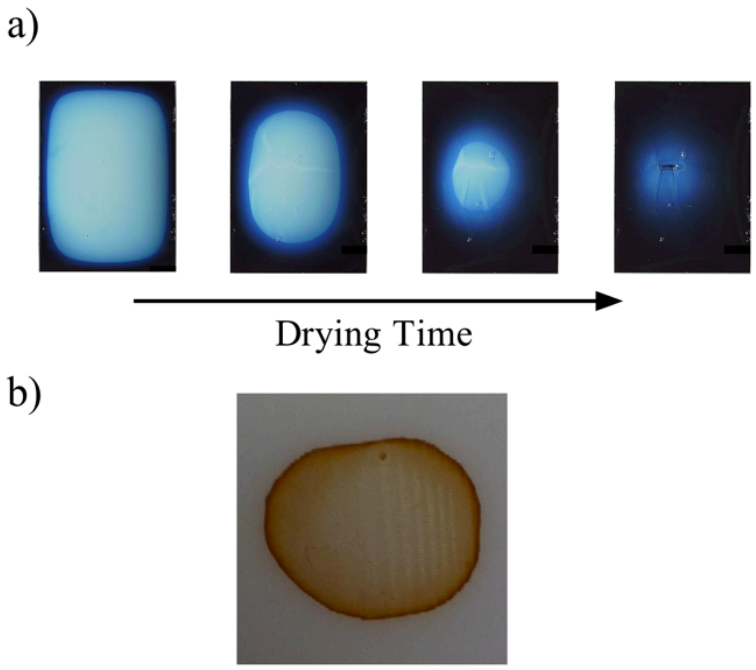

Figure 2.5 (a) Visual appearance of a latex particle coating (50:50 PVDF:acrylic) drying on a 5 x 7 mm silicon substrate. (b) Photograph of a "coffee ring" deposit formed during lateral drying.

As particle-based coatings dry, the coating achieves consolidation first wherever the coating is thinnest, which often occurs near the edges where the coating meets the substrate. Further drying from the consolidated edges results in the formation of curved menisci between adjacent particles, which induces a capillary pressure in the liquid. The pressure gradient in the coating generates a flow of liquid (and particles) from the bulk of the coating toward the consolidated network to replace the liquid lost to evaporation. Consequently, particles are deposited near the edge of the consolidated region and the particle network grows. The boundary between the consolidated region and the suspended region is often referred to as the "consolidation front".

Sutanto et al.[11] used cryogenic scanning electron microscopy (cryoSEM) to image the formation of a consolidation front during the early stages of drying for a latex coating.

Eventually, the flow of water through the particle network becomes restricted as the latex particles deform or the consolidated region becomes too large. When this occurs, the flow of water to the edge is not sufficient to replace the volume lost to evaporation. Consequently, the liquid-air interface must move into the particle packing, emptying the pores, and leaving behind a dry particle network. The boundary between the dry particle network and the consolidated network is often referred to as the drying front. A schematic diagram of the lateral drying process is shown in Figure 2.6. In most cases, the drying front propagates from the edges of the coating inward; however, if the coating is thinnest near the center of a coating, drying fronts can propagate from the center toward the edge.[45]

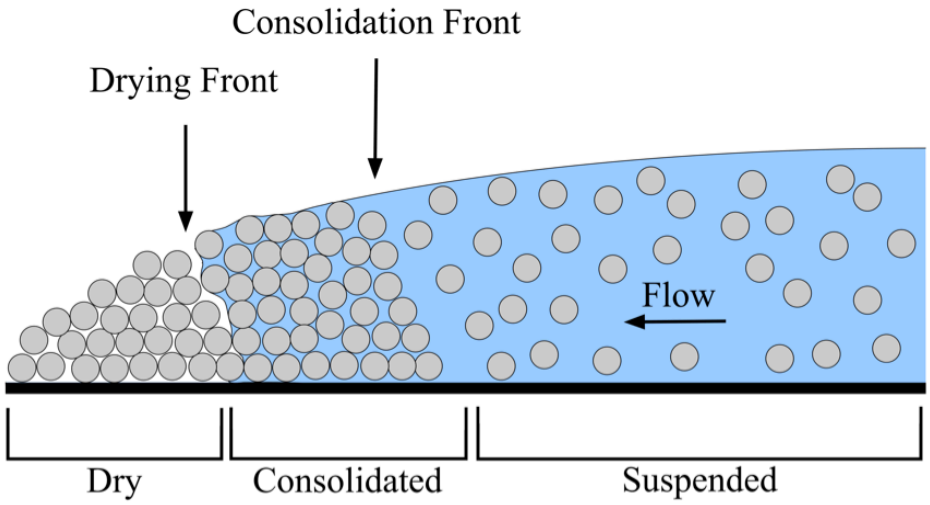

Figure 2.6 Diagram of the lateral drying process for a particle-based coating.

Lateral drying was first observed by Hwa[46] in 1964, and subsequently by others[29,30,33,42]. A comprehensive discussion of past research on lateral drying can be found in the review article by Holl et al.[29] Similar to the model proposed above, Winnik and Feng[47] suggest that continued drying from the consolidated network drives the lateral

propagation of the consolidation front and subsequent lateral drying. In contrast, the models proposed by Deegan et al.[42] and Parisse and Allain[48] suggest that the base of the coating cannot shrink due to contact line pinning and flow toward the edge is generated by the need to retain the shape of the drop. Routh and Russell[44] developed a model to describe the formation and propagation of both consolidation and drying fronts in dilute dispersions. In their model, they define a dimensionless capillary pressure, p_{cap}, which balance the capillary pressure with the characteristic pressure needed for flow through a packed particle bed. Salamanca et al.[49] systematically varied p_{cap} and found that lateral drying is promoted for small particle sizes, fast evaporation rates, and thick coatings.

It is possible for coatings to exhibit both top-down drying and edge in drying simultaneously. This condition was observed by Okubo et al.[50] where an acrylic latex coating exhibited both lateral drying and the formation of a polymer skin over the central wet region. This behavior was also observed in the cryoSEM experiments of Sutanto et al.[11] This behavior was also seen in the experimental results presented in Chapter 4. CryoSEM, revealed that latex coatings dried on silicon chips can exhibit both particle accumulation near the edge as well as top-down accumulation[51]

2.5 *Stress Development*

Generally, coatings are applied in liquid form and undergo some form of solidification to achieve the final coating. Solidification may occur by many different mechanisms including, drying (removal of solvent), aggregation, coalescence, crystallization, and chemical reaction (curing). Regardless of the mechanism, the solidification process produces a shrinkage or reduction in volume of the coating. If the

coating were allowed to shrink freely, there would be no stress development in the coating. However, due to adhesion of the coating to the substrate the coating cannot shrink in the plane of the substrate. This constrained shrinkage results in the development of an in-plane biaxial tensile stress in the coating.[6,52,53]

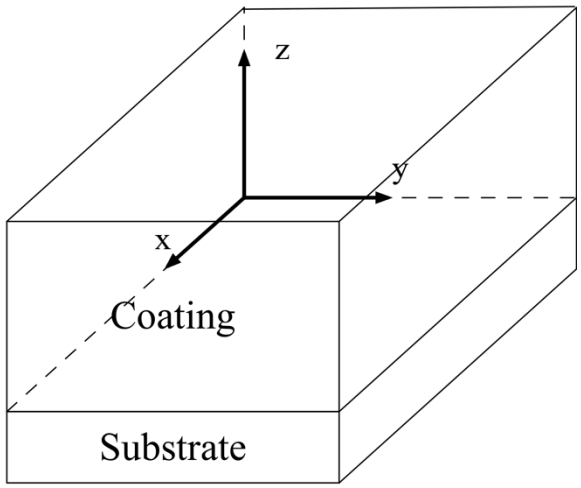

Figure 2.7 Schematic diagram of a coating element on a substrate.

As explained above, stress develops due to constrained shrinkage of the coating. Consider a single coating element, Figure 2.7, during solidification the coating is allowed to shrink in the z-direction, therefore $\sigma_{zz} = 0$. This gives the condition of plane stress for the coating. In the other two directions, the stress is non-zero due to the strain created due to shrinkage. The constrained in-plane shrinkage of the film is related to the stress components by:

$$\sigma_{xx} = \frac{E}{(1-\nu^2)}\left(\varepsilon_{xx} + \nu\varepsilon_{yy}\right) \tag{2.5}$$

$$\sigma_{yy} = \frac{E}{(1-v^2)}\left(\varepsilon_{yy} + v\varepsilon_{xx}\right) \tag{2.6}$$

If the coating material is assumed to be isotropic in nature then:

$$\varepsilon_{yy} = \varepsilon_{xx} = \varepsilon \tag{2.7}$$

Therefore, the stress in the coating can be expressed by:

$$\sigma = \sigma_{xx} = \sigma_{yy} = \frac{E\varepsilon}{(1-v)} \tag{2.8}$$

The stress, σ, in Eq. 2.8, is the averaged bi-axial in-plane stress. Other stresses are present including shear and peeling stresses; however, these stresses are concentrated near the edges of the coating. Additionally, when the coating is much wider and longer than it is thick, the shear and peeling stress can be assumed to be negligible.[7,8] A thermal expansion mismatch between the coating and the substrate can also give rise to stress in the coating; however, these stresses are negligible when the drying experiments are conducted at constant temperature.

2.6 *Summary*

This chapter outlines many of the important features of the drying process including a general theory of drying for hard particle coatings, the fundamentals of latex film formation, lateral drying, and stress development. The drying process and the resulting microstructure development are dynamic processes that depend on many variables. The experimental results presented in this thesis aim to make connections between stress development in particle-based systems and the developing coating microstructure. The basic concepts outlined in this chapter provide a foundation for further discussion throughout this thesis.

Chapter 3

EXPERIMENTAL METHODS

3.1 *Introduction*

The main objective of this thesis is to investigate the relationships between stress development and microstructure development in particle-based coatings during drying. Both microstructure and stress develop as the coating dries, which necessitates the need for experimental methods that can provide dynamic measurements of the coating stress and characterize the microstructure during drying. Cryogenic scanning electron microscopy (cryoSEM) allows high-resolution imaging of the coating microstructure during the intermediate stages of the drying process. To monitor coating stress, a cantilever deflection technique is used which provides *in-situ* measurements of stress during drying.

The coating systems explored in this thesis include ceramic particle coatings, latex particle coatings (high and low glass transition temperature polymers), and structured multiphase latex particles. To fully characterize these coatings a number of

experimental techniques were used including digital (light) microscopy, scanning electron microscopy (SEM, cryoSEM), atomic force microscopy (AFM), stress measurements, and minimum film formation temperature measurements. Many of these techniques are commonly used to characterize coatings and other materials. This chapter will highlight some of the unique techniques that were used in this work.

3.2 *Minimum Film Formation Temperature Bar*

The minimum film formation temperature (MFFT) bar is one of the most common and simplest techniques used to study the film formation behavior of latex coatings. The main components of the MFFT measurement is a flat bar (typically made of metal) on which a temperature gradient is formed where one end is cooler and the other end is warmer. In this work, a polyethylene terephthalate (PET) film was first placed on the temperature gradient bar and the coating was applied to the PET substrate, not directly on the metal bar. After coating the PET, the film was allowed to dry on the temperature gradient bar.

As the name implies, the MFFT bar determines the lowest temperature at which a latex coating forms a film upon drying. The MFFT can be described by three different transitions: the cloudy-clear transition, the crack point, or the knife point.[1] The cloudy-clear transition is the most commonly used transition, and serves as an indicator of the extent of particle deformation in the film. Above the MFFT, latex particles deform to close the voids between particles. This prevents light scattering from the film and the coating appears transparent. At temperatures below the MFFT, particle deformation is limited and light is scattered from the dry film giving it an opaque appearance. The

temperature at which this transition occurs is the MFFT. Often, the MFFT is close to the glass transition temperature (T_{ag}) of the latex particles. This is reasonable because below the T_g the modulus of the polymer increases and therefore particle deformation is restricted. An example of the cloudy-clear transition is shown in Figure 3.1. For this sample, the location of the transition is very clear; however, for some samples the exact location is more difficult to determine.

The crack point transition can also be used to define the MFFT. The crack point is the temperature at which cracks are no longer observed in the dried latex film. The crack point can be thought of as the lowest temperature at which polymer molecules can diffuse across the particle interfaces. Often the cloudy-clear transition and the crack point transition occur simultaneously. A third transition, the knife point, is less commonly used and is defined as the minimum temperature at which the film can resist mechanical shearing.

The ASTM procedure for determining the MFFT does not specify a specific transition. Additionally, the ASTM standard does not specify a standardized drying time. For some systems, the latex particles may undergo dry sintering, and the location of the MFFT may move to slightly lower temperatures. However, dry sintering generally occurs slowly over time. Therefore it is important to keep the drying time constant when conducting MFFT experiments. Another concern is that determining the exact location of the transition is subjective in nature. Therefore, it is helpful if the same person conducts the experiments on the entire series of samples so that the objectivity in the

measurement is the same from sample to sample. The experimental apparatus used in this work is an MFFT90 (Rhopoint) shown in Figure 3.1.

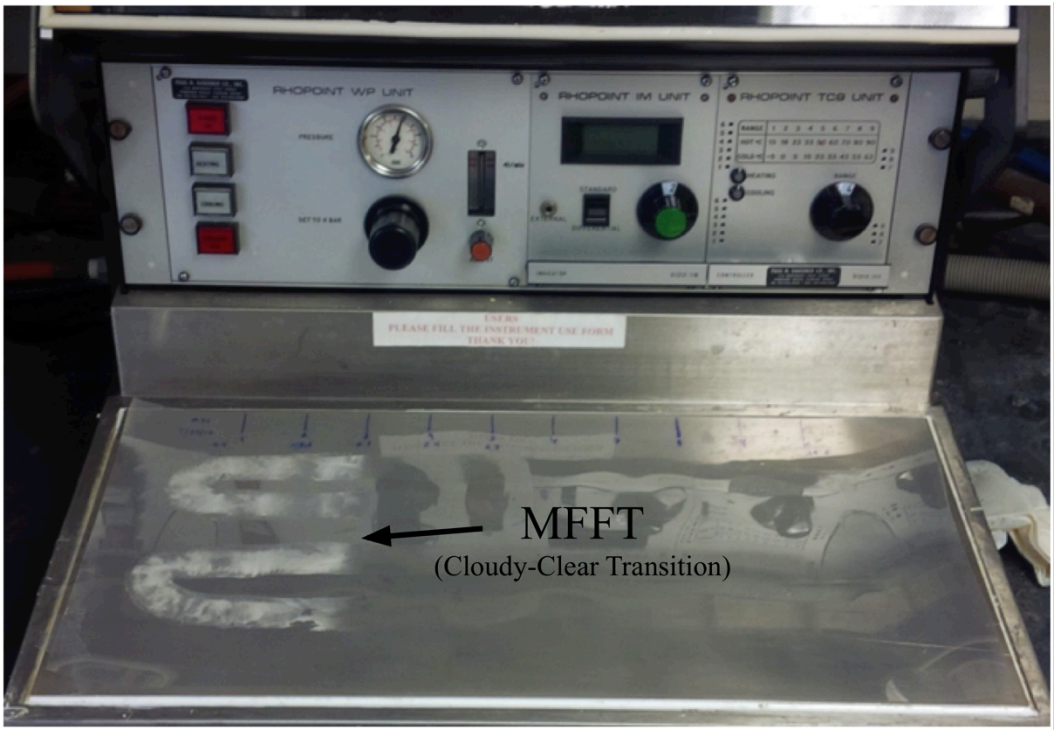

Figure 3.1 Photograph of the minimum film formation temperature bar, MFFT90 (Rhopoint). A PET film covers the metal temperature gradient bar, which is cooler on the left side and warmer on the right. A latex coating has been fully dried, and the cloudy-clear transition is clearly visible.

3.3 *Stress Measurement*

Stress development in thin films on rigid substrates has been studied by a variety of techniques.[8,43,54–58] Many of these techniques monitor stress development in a coating by measuring the curvature or deflection of the substrate during drying. Substrate curvature may be measured by optical interference methods,[43,58] capacitive deflection measurements,[27] or with laser-photodiode combinations.[56,59–62] To monitor stress development, *in-situ,* an apparatus based on the cantilever deflection technique was designed.[6–8] The following section introduces the classical theory behind the cantilever

deflection technique, and discusses some limitations of the technique as well as strategies to overcome these limitations.

3.3.1 *Theory: Cantilever Deflection Technique*

Many of the early studies on stress development focused on stress generated in electrodeposited metal films. Stoney,[54] using classical beam theory, derived an expression relating coating stress to the deflection of a coated cantilever beam:

$$\sigma = \frac{E_s t^2 d}{3cL^2} \tag{3.1}$$

where E_s is the Young's modulus of the substrate, t is the substrate thickness, d is the deflection of the cantilever, c is the coating thickness, and L is the free length of the cantilever. In this analysis, Stoney assumed that stress was uniaxial, the moduli of the coating and substrate were similar, and the substrate was much thicker than that coating.

Improving upon the work by Stoney, Corcoran[55] derived a modified equation for the bi-axial stress in the coating using plate theory:[63]

$$\sigma = \frac{dE_s t^3}{3cL^2(t+c)(1-v_s)} + \frac{dE_c(t+c)}{L^2(1-v_c)} \tag{3.2}$$

where v_s is the Poisson's ratio of the substrate, E_c is the Young's modulus of the coating, and v_c is the Poisson's ratio of the coating. The second term in Eq. 3.2 accounts for the relaxation in coating stress that results from the bending action of the cantilever. The measured stress would be higher if the substrate was rigid and did not bend. Corcoran also assumed that the coating is perfectly adhered to the substrate, that the deflection of the cantilever is spherical, that the elastic limits of the materials are not exceeded, that the

material properties of the coating and the substrate are isotropic, and that any stress gradients in the thickness of the coating are negligible.

Using the full form of Eq. 3.2 requires that the Young's modulus and Poisson's ratio of the coating are known. However, these values are difficult to measure for thin films, and may differ from the properties of the bulk material. Corcoran[55] showed that for thin coatings relative to the substrate thickness ($t >> c$) and for rigid substrates ($E_s >> E_c$) that the second term in Eq. 3.2 can be neglected without introducing significant error into the calculation. Assuming the coating has and elastic modulus, E_c = 3 GPa[64], and a typical coating thickness used in these experiments , c =50 μm, neglecting the second term in results in an error of less than one percent. The results presented in this work are calculated by using only the first term of Eq. 3.2 to calculate the coating stress.

Additionally, the coating thickness, c, used in the calculations is not the instantaneous thickness of the coating during drying. Instead, the average thickness of the dry coating is used in the calculations. The use of the dry thickness provides a reasonable estimate for the coating stress because stress cannot develop until the coating reaches consolidation. After consolidation, only small changes in the coating thickness are expected.

One limitation of the cantilever deflection technique is that only an average stress in the coating can be determined from a measurement of the cantilever deflection. However, particle-based coatings often exhibit non-uniform (lateral) drying from the edge-in. The phenomenon of lateral drying was discussed in greater detail in Chapter 2. When lateral drying fronts are present, stress development occurs non-uniformly across

the substrate.[57] Therefore, when using the cantilever deflection technique, efforts should be taken to suppress lateral drying. To achieve this, a novel cantilever design and a modified version of Eq. 3.2 are used to determine the coating stress. This will be discussed in greater detail in Chapter 5.

3.3.2 *Stress Measurement Apparatus*

The stress measurement apparatus used in this work was designed[6] and then modified by past researchers.[7,8] For the current research, several modifications were made to the experimental apparatus to increase the sensitivity of the measurement. These improvements included a new fiber-optic coupled diode laser (λ= 670 nm, Melles Griot) and beam collimator, a new position sensitive photodiode with USB connectivity (Spot-On Analog, Duma Optronics), a modified sample holder, and a new calibration bar.

The diode laser and collimator reduce the noise in the signal by providing increased pointing stability and reducing the angular drift of the laser spot. Additionally, the new photodiode reduces signal noise due to the increased position sensitivity of the detector. An added benefit of the new Spot-On system is the USB connectivity, allowing the capability to directly interface with computer software for data collection. Figure 3.2 shows a schematic diagram of the stress measurement apparatus.

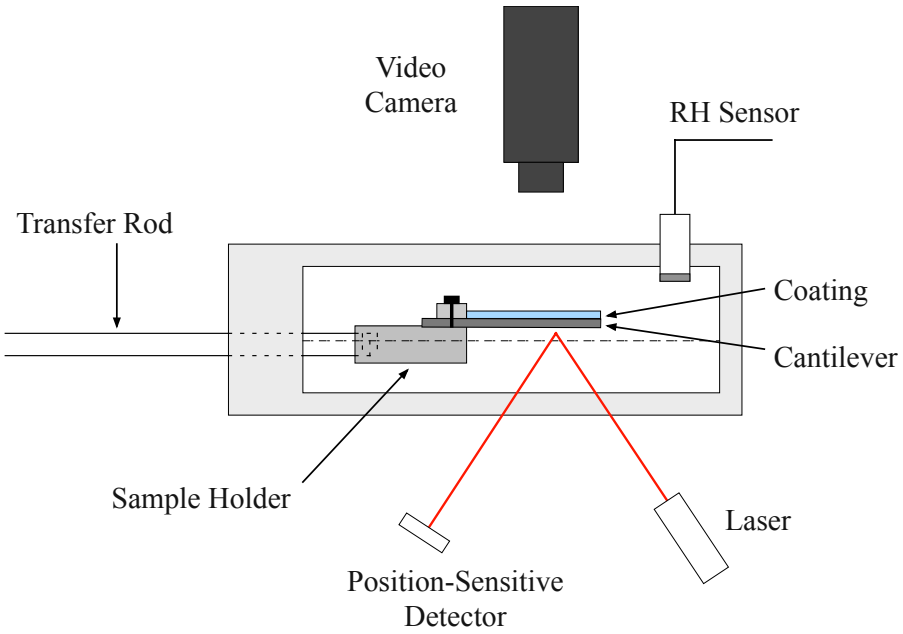

Side View

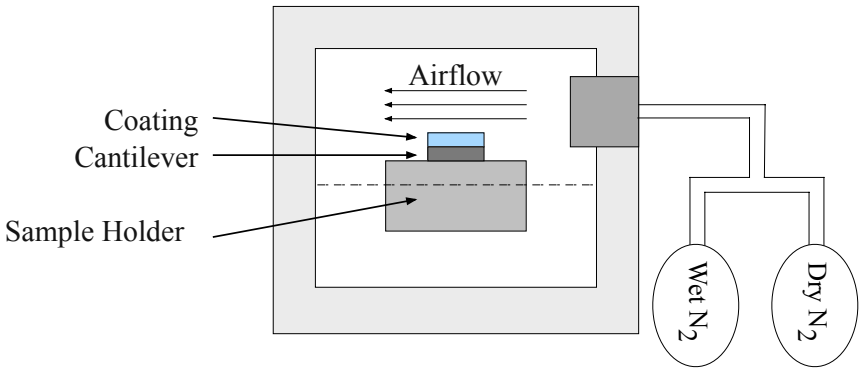

Cross-Section View

Figure 3.2 Schematic diagrams of the side view and cross-sectional view of the stress measurement apparatus used in this work to monitor stress development in coating during drying.

The measurement process involves several steps. First, a cantilever is fixed into the sample holder and moved into the sample chamber. The cantilever is then calibrated by applying a series of known deflections with a micrometer and recording the movement of the laser spot on the position sensitive detector (PSD). Previous researchers used a hook attached to the end of a micrometer to provide the deflection to the end of the cantilever. While this technique was effective, the hook needed to be placed directly in the center of the cantilever at the very end to achieve reproducible results. To remedy this, a calibration bar was designed which decreases human error and increases the reproducibility of the calibration results. A photograph of the calibration step and a schematic representation of the calibration bar are shown in Fig. 3.3.

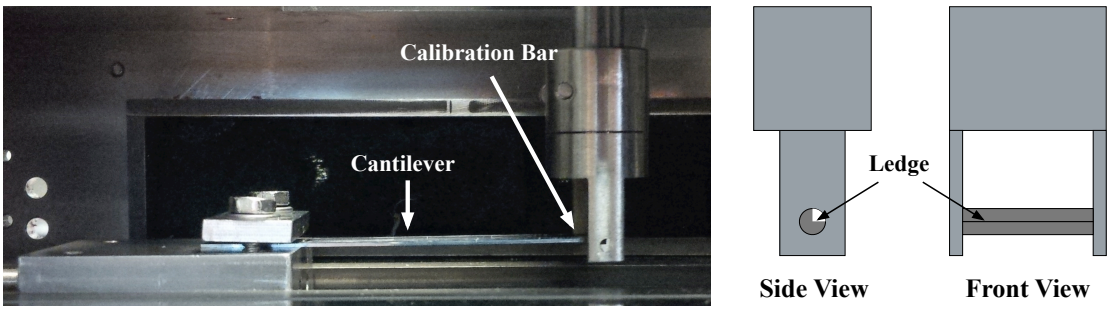

Figure 3.3 Photograph of the calibration step (left) and a schematic representation of the calibration bar designed to improve accuracy and reproducibility of the calibration step.

For each cantilever, a calibration curve is generated by applying a deflection to the cantilever and recording the location of the laser spot on the position sensitive detector. The slope of the calibration curve is used to transform the position data recorded by the PSD into a cantilever deflection. After calibration is complete, the sample holder (with the cantilever still attached) is carefully removed from the controlled

environment chamber and placed in a plasma cleaner where the cantilever is cleaned for approximately 15 seconds. The sample holder is then carefully returned to the controlled environment chamber where the coating is applied to the cantilever. Several methods can be used to apply the coating onto the cantilever including: blade coating, wire-wound rod coating, and controlled volume deposition by micropipette. After the coating is applied, the sample holder is moved into the controlled environment chamber and data acquisition begins. Inside the controlled environment chamber, the temperature and relative humidity (RH) are controlled by mixing dry nitrogen and partially saturated nitrogen gas.

3.3.3 *Calibration*

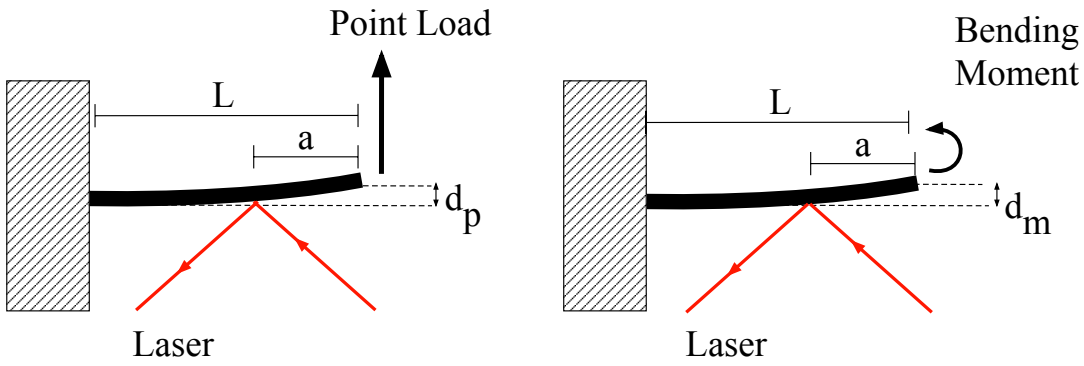

Figure 3.4 Schematic diagrams showing the deflection of a cantilever under a point load (left) and a bending moment (right).

Calibration is an important step in the stress measurement process as it relates the position of the laser on the PSD to the actual deflection of the cantilever. As described by Payne[6], the deflection of a cantilever depends on the loading situation (e.g. a point load vs. a distributed load), Figure 3.4. The calibration curve will only be accurate when the angle of the deflection where the laser spot is positioned, is the same for both the stress in the coating (bending moment at the end of the beam) and a point load (used for

the calibration step). The equations for the slope, θ, at a distance, *a,* from the end of the beam for both conditions are:

$$\theta_p = \frac{3d_p}{3L^3}(L^2 - a^2)$$
$$\theta_m = \frac{3d_m}{L^2}(L - a) \tag{3.3}$$

here, d_p and d_m are the deflections measured during calibration (point load) and stress measurement (bending moment), respectively. Assuming that the slopes are equal one can obtain:

$$\frac{d_p}{d_m} = \frac{4L}{3(L + a)} \tag{3.4}$$

Then assuming $d_p = d_m$,

$$a = \frac{L}{3} \tag{3.5}$$

Therefore, the laser spot is positioned one third of the length inward from the end of the cantilever (e.g. for a 45 mm cantilever the laser is positioned 15 mm from the free end).

3.3.4 *Weight Loss Correction*

The coating suspensions used in these studies have a volume fraction of solids ranging from 20% to 50%. As water evaporates, the weight of the coating decreases, which causes an upward deflection of the cantilever. The weight change in the coating can be converted into a deflection, d_{wt}, with the relationship[7,65]:

$$d_{wt}(t) = \frac{m(t)g}{2LEwh^3}(x^4 - 4L^3x + 3L^4) \tag{3.6}$$

where g, is the gravitational acceleration, w, is the width of the cantilever, x is the distance from the free end of the cantilever, $m(t)$, is the mass of the coating as a function of time t, and h is the cantilever thickness. For the coatings investigated in this work, the correction due to weight loss is negligible; therefore the measured deflections were not corrected for weight loss in the results presented in this thesis. However, for thick coatings, coatings with high water content, or coatings prepared on thinner cantilevers this correction may become significant and should considered.

3.4 *Cryogenic Scanning Electron Microscopy*

One of the goals of this research is to understand how the coating microstructure develops during drying. Since the size of the particles used in particle-based coatings ranges between tens of nanometers to tens of microns, a high-resolution imaging technique is needed. Several experimental techniques are available that are capable of probing the coating microstructure of a fully dried film such as electron microscopy and atomic force microscopy. However, to fully understand the development of the microstructure with time, it is necessary to image the intermediate stages of drying. Cryogenic scanning electron microscopy (cryoSEM), uses the same principles as conventional scanning electron microscopy (SEM), but allows the intermediate stages of drying to be imaged, in a high vacuum environment, before the sample is completely dry.

3.4.1 *Scanning Electron Microscopy (SEM)*

Electron microscopy is a useful characterization tool and one of the most widely used methods for obtaining high-resolution images of solid surfaces. A scanning electron

microscope forms an image of the surface by scanning a focused beam of electrons across a specified area of the sample. Contrast is mainly achieved through the topography of the sample, and to a lesser extent the electron density (atomic number) of the atoms in the sample.

When the electron beam interacts with the sample surface, two signals are produced which can be used to form the image. The standard detector used in SEM is the secondary electron detector. Secondary electrons (SE) are low-energy electrons (~50eV), which have interacted inelastically with the sample before being expelled from the surface. The SE signal gives mostly topographic information about the sample surface. Backscattered electrons (BSE) are elastically scattered from the sample and can have energy close to that of the impinging beam. The BSE signal is highly dependent on the atomic number of the atoms (higher electron density), which gives the BSE detector increased sensitivity to compositional differences in the sample.

SEM is a versatile technique that can accept a wide variety of sample types. However, samples must withstand the high vacuum environment of the sample chamber in the SEM (~ 1 x 10^{-6} Pa), which does not allow liquids to be imaged in a conventional SEM without evaporating the liquid and contaminating the microscope.

3.4.2 *Cryogenic Scanning Electron Microscopy*

CryoSEM is a technique that was developed by biologists to image cells without the need for chemical fixation, which dehydrates the cells and destroys the native cellular structure. For a cryoSEM study, the samples are vitrified before they are imaged at cryogenic temperatures in a conventional SEM equipped with a stage cooled with liquid

nitrogen. Vitrification, rather than freezing, is desired because during freezing, the formation and growth of ice crystals rearranges the native microstructure in the sample. Proper vitrificaton requires a quench rate of approximately 10,000 $K \cdot s^{-1}$.[66] In this work the sample size is too large to ensure that proper vitrification has taken place. However, visualization of the microstructure indicates that no rearrangement of the particles occurred.

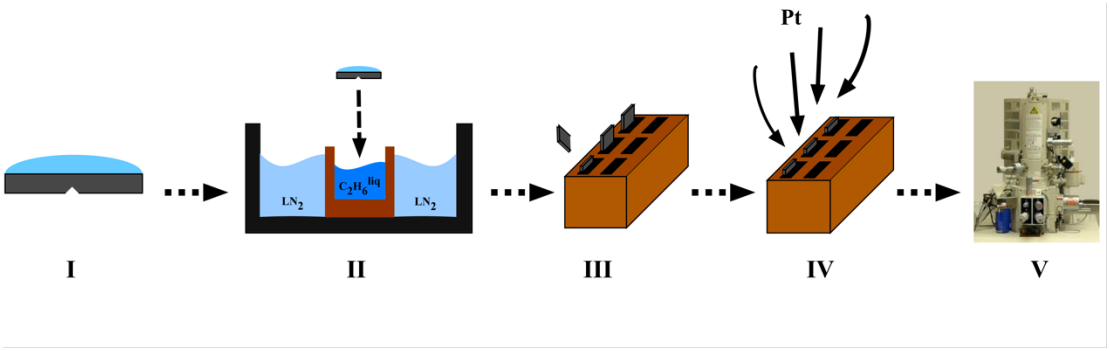

Figure 3.5 The plunge freezing technique used to prepare partially dried samples for cryoSEM imaging involves five steps. I) A coating is applied to the substrate and undergoes a period of drying. II) The sample is plunged into a bath of liquid ethane, which is surrounded by liquid nitrogen. III) Samples are fractured in a high vacuum condition to expose the cross-section of the coating. IV) A thin layer of platinum (~ 5 nm) is sputter coated onto the fracture surface. V) The samples are moved to the microscope and imaged at cryogenic temperatures.

Samples for cryoSEM analysis were prepared in a method similar to that used by previous researchers[10–12,15,67]. A schematic diagram of the sample preparation process is shown in Figure 3.5. The plunge-freezing technique involves a series of five steps; first, a coating was applied to the substrate (5 x 7 mm silicon chip, 6 x 45 mm silicon cantilever, etc.) that was pre-scored for more reliable fracture. The coating was allowed to dry for some amount of time before it was frozen. Samples are frozen by plunge

freezing the silicon chip into a bath of liquid ethane that was surrounded by liquid nitrogen. Liquid ethane is the preferred cryogen for these studies because of the large difference between the boiling temperature (-89°C) and the freezing point (-172° C), which maximizes the heat transfer from the sample. Extensive research was performed by Gee et al.[68] to show that vitrification is optimized when the sample is plunged at an angle of 75° from the horizontal. This freezing method was reported for 30 μm thick films; however, the coatings in this study may be as thick as 250 μm. When thick films were tilted during plunging, it caused the coating to flow, altering the coating thickness and microstructure. For this reason, samples were not tilted during the plunge-freezing step in this research.

After freezing, the samples were kept under a bath of liquid nitrogen to minimize exposure to atmospheric moisture. While under liquid nitrogen, the samples were loaded into the cryoSEM sample holder, Fig 3.5. The sample holder was then transferred into a high vacuum environment inside the Emitech cryoSEM preparation chamber. After the samples are in the chamber, the substrates were fractured. Under certain conditions it is desirable to etch away some of the frozen water from the frozen fracture surface in order to enhance topographic contrast. To do this, the temperature is raised to -96°C, where the etch rate of pure vitreous ice is on the order of 10 $nm \cdot s^{-1}$.[69] The high vacuum environment of the Emitech cryo preparation chamber prevents the recrystallization of sublimed moisture onto the frozen sample surface. Before transferring the samples into the microscope, the fracture surface was sputter coated with a thin layer (approximately 5 nm) of platinum. Finally, the samples are transferred to a Hitachi S-4700 FESEM,

equipped with a stage cooled by liquid nitrogen and held at a temperature of approximately -150°C during imaging.

3.4.3 *Artifacts of CryoSEM Sample Preparation*

CryoSEM is a unique characterization method; however, artifacts that arise during sample preparation and imaging often complicate analysis. This section will explore some of the common artifacts that are encountered when preparing samples for cryoSEM. It is important to understand the origin of these artifacts so that they can be prevented whenever possible. When freezing artifacts are present, it is important to recognize these features as artifacts for proper characterization of the coating microstructure.

Freezing Artifacts:

When the freezing rate of samples is slow, ice crystals form in the sample and solids are pushed to the crystal grain boundaries. Rearrangement of the solids in the coating destroys the microstructure that was present before freezing. Poor freezing is identifiable by the presence of particle-free zones surrounded by a particle-rich zone where the excluded particles were deposited. Poor freezing typically occurs when the sample was too thick, or the sample was frozen in a poor cryogen (cooling rate was too slow). To reduce these artifacts, the sample thickness should be kept as thin as possible and liquid ethane should be used as the cryogen.

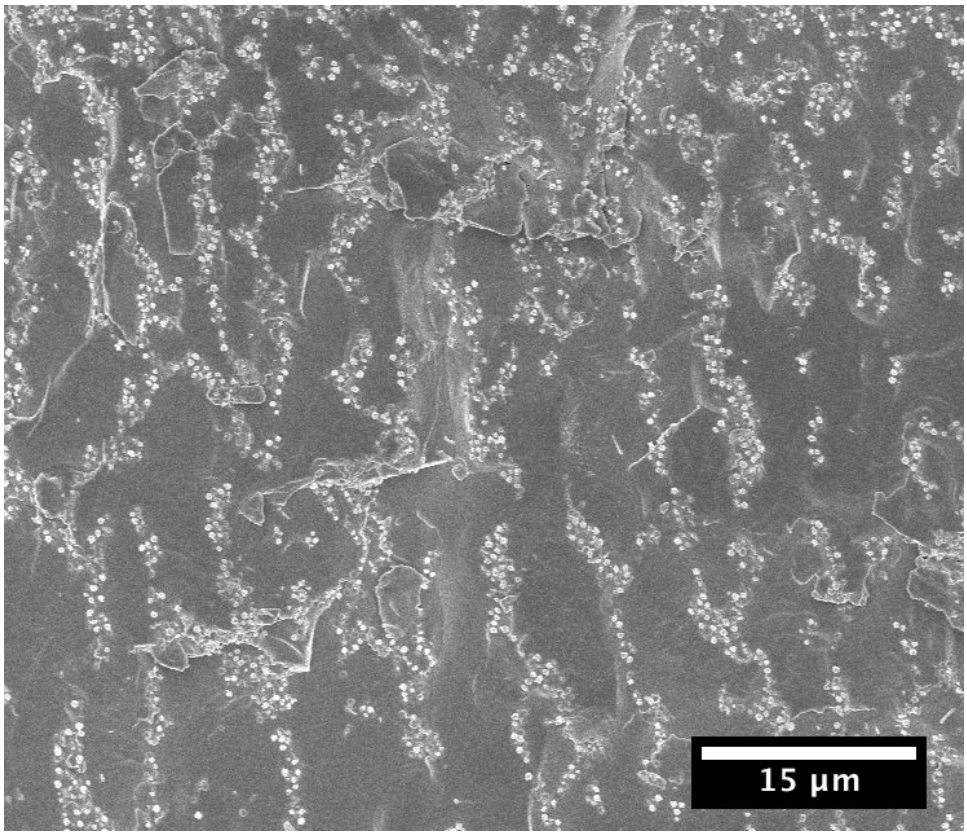

Figure 3.6 CryoSEM micrographs of a sample where poor freezing resulted in ice crystal growth and particle rearrangement in the frozen sample. Particle free, and particle rich zones are clearly evident throughout the sample.

Frost Contamination:

If the cryoSEM sample is exposed to the ambient atmosphere after it is frozen, moisture in the air will likely condense onto the sample surface. Frost contamination can take many forms and has a wide variety of appearances. Figure 3.7 shows cryoSEM micrographs with various forms of frost and ice contamination. Frost contamination may appear as large crystals on the sample surface (hexagonal ice, cubic ice, etc.), a "blanketing" effect where a layer of ice covers the sample surface or particles, or a speckled "decoration" of the sample surface where small frost particles randomly

distribute themselves on the sample surface. Identifying frost contamination and differentiating frost from particles in the sample can be difficult depending on the coating system being studied. One strategy for identifying frost contamination is to examine the fracture surface of the silicon substrate. If the silicon surface is decorated with frost contamination the sample surface will likely have similar contamination. From contamination on the sample surface is not detrimental to the microstructure of the coating. However, when frost contamination is extensive it may be difficult to accurately characterize the microstructure. To avoid frost contamination, efforts should be taken to protect the samples from being exposed to ambient air during the sample preparation procedure.

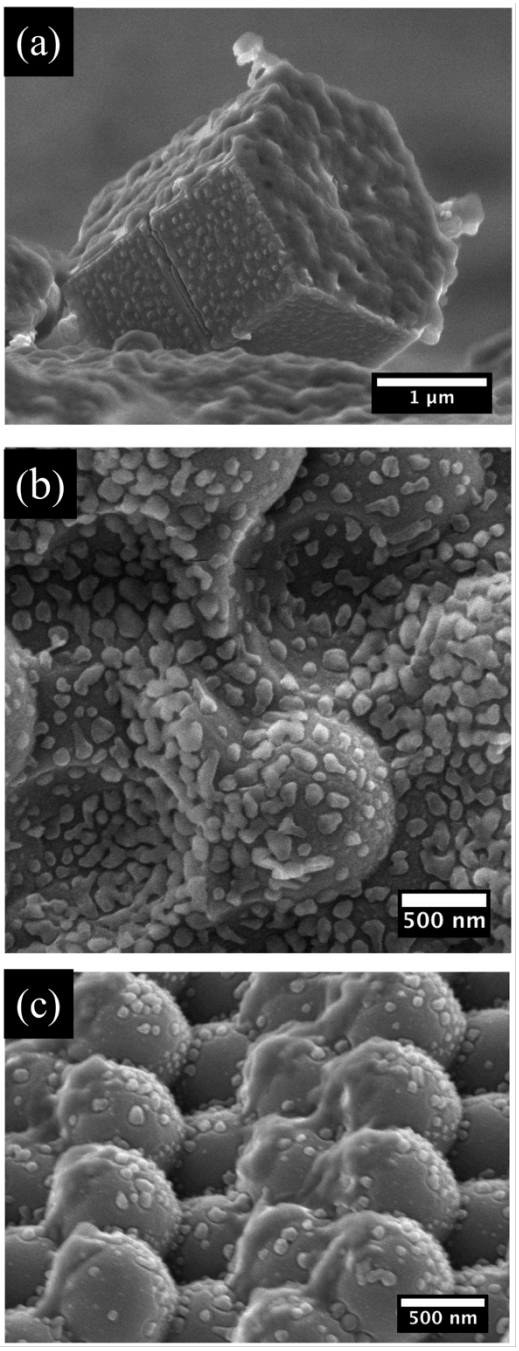

Figure 3.7 CryoSEM micrographs showing the different appearance of frost contamination on the frozen sample surface. (a) hexagonal ice crystal on the sample surface (b) speckled frost "decoration" covering the fracture surface (c) directional frost "blanketing" and speckled frost "decoration".

"*Pullouts*"

When a frozen latex dispersion is fractured, the latex particles embedded in the frozen matrix deform plastically forming an artifact referred to as a "pullout". The formation of these artifacts is unusual since the latex particles are fractured well below their glass transition temperatures. A complete investigation of the formation of these artifacts was performed by Ge et al.[13,70] The formation of these pullouts are often helpful during sample characterization, as their appearance is an indicator of the degree of film formation in the coating. When the latex particles are fully dispersed. the particles are strongly adhered to the surrounding frozen matrix. As the fracture surface travels through an embedded particle the particle is stretched into "horn" or "dog-bone" type shapes. The cryoSEM micrograph shown in Figure 3.8 shows the appearance of pullouts from a latex in the dispersed state. It is also possible that a particle is removed from the sample surface during fracture, leaving behind a socket or crater-like structure on the frozen fracture surface.

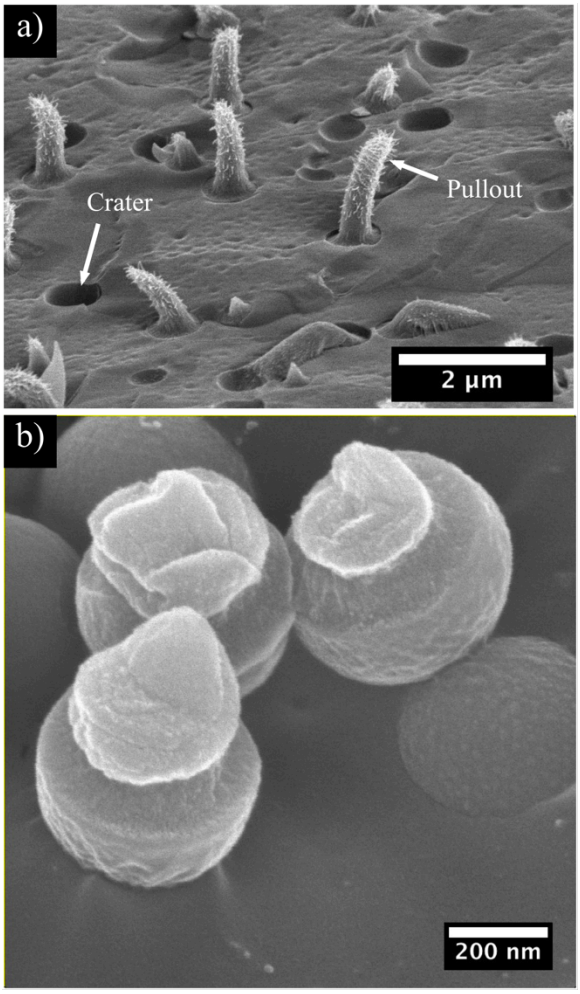

Figure 3.8 a) CryoSEM micrographs showing the formation of pullouts from a frozen dispersion of latex particles. The "hairy" structure on the pullouts is believed to be a form of ice contamination. b) CryoSEM image of latex particle "pullouts" that have been revealed through sublimation of the frozen water matrix.

Once the latex particles have reached touching contact, compaction begins and the particles flatten against each other. At this stage of drying, the latex particles are held together by van der Waals forces and small amounts of residual water that remains in the porespace. Since adhesion between particles is weak, the fracture surface often travels along particle boundaries and pullouts do not form; however, some pullouts are still possible depending on the amount of coalescence.

Later in the film formation process, latex particles have deformed and polymer chains have had sufficient time to diffuse across particle boundaries. Consequently, pullouts that form during this stage of drying bridge multiple particles. Bridged pullouts often form a web-like structure on the fracture surface. When coalescence is complete, particle boundaries are no longer discernable and the facture surface will appear smooth, without pullouts.

3.5 *Summary*

This Chapter outlines some of the characterization tools that were used in this research to monitor stress development and characterize the coating microstructure. By themselves, each of these techniques can give interesting results. However, the real power comes when these techniques are combined. By combining the results from various characterization methods a more comprehensive understanding of the samples can be achieved. For instance, to understand the relationships between the coating microstructure and the evolution of stress, both stress measurement and microstructure characterization (by SEM, cryoSEM, or AFM) should be combined. This strategy was to fully characterize the coatings systems investigated in this thesis.

Chapter 4

WALLED SUBSTRATES AND DRYING UNIFORMITY[1]

4.1 *Background and Motivation*

Many technological applications require the ability to precisely control the particle distribution (and subsequent coating uniformity) of a colloidal suspension drying drying.[71–74] Achieving this level of control can be difficult, especially for coatings cast on small substrates or for small coating volumes (small drops) where thickness non-uniformities may dominate and have adverse consequences in the final product. An example of this, is the use of inkjet printing as a means to produce low-cost large area flexible organic light emitting devices.[71] For this application, a solution is printed in discrete areas to generate pixels for a display. Precisely controlling the coating thickness is important for having pixels with a uniform appearance.

The distribution of particles in a drying drop of colloidal suspension on a non-walled substrate has been studied previously. The so-called "coffee-ring" effect was first explained by Deegan et al.[42] who describe the origin of ring-like deposits left behind after drop of dilute colloidal suspension dries. They attributed this behavior to faster

[1] This chapter was published in adapted form:
Price, K. K.; McCormick, A. V; Francis, L. F. CryoSEM Investigation of Latex Coatings Dried in Walled Substrates. *Langmuir* **2012**, *28*, 10329–10333.

evaporation rates near edge (where the curvature of the coating surface is greatest) and to contact line pinning of the drying drop. Considering more concentrated suspensions, Routh and Russel[44] developed a model that predicts particle deposition at the edge of a coating by coupling evaporation near the edge and contact line pinning. Their model also includes capillary induced pressure gradients near the edge, that are the driving force for fluid flow in the drying coating.

Suppressing edge effects is especially important when working with small sample sizes, like those used experimentally where lateral drying represents the dominant mode of drying. Previous efforts to achieve uniformity include controlling surfactant concentration, substrate temperature, and generating Marangoni flows in the coating to counteract flow to the edge.[72,75,76] Other attempts have improved uniformity by including a raised wall or other topography at the edges of a coating or printed feature. [8,9,73,77–81] When a coating is deposited into a shallow well, the presence of the edge or border alters the equilibrium shape of the wet coating eliminating the thin edges where the coating meets the substrate. Consequently, the drying behavior and subsequent particle deposition is altered.

Some studies have been conducted which describe the dried thickness profile of a polymer solution deposited on a walled substrate.[73,77] When the coating is fully dry, the polymer film is thicker near the wall; the authors attribute this behavior to flow from the central region to the wall, which concentrates polymer there. Particle image velocimetry (PIV) measurements of drying polymer solutions also came to similar conclusions.[82] Due to their importance in printed organic electronics applications, polymer solutions have

received much of the attention in the literature, while microstructure development of particle-based coatings dried on walled substrates has not received the same level of interest.

In this study, cryogenic scanning electron microscopy (cryoSEM) was used to characterize the development of the coating microstructure during drying. A waterborne latex coating was used for these experiments. In past studies, cryoSEM has been used to monitor the microstructure development of drying latex coatings, allowing direct observation of structural changes in the coating that are inaccessible by other experimental techniques.[9–11,83] CryoSEM, was used to investigate the influence of the walled substrate geometry on both the particle distribution and microstructure formation during drying. Understanding the relationships between the drying geometry, microstructure development, and drying uniformity is crucial for controlling the drying behavior of coatings deposited on walled substrates.

4.2 *Materials and Methods*

4.2.1 Latex

A monodisperse, poly(methyl methacrylate-co-n-butyl acrylate) (PMMA-co-PBA) latex was synthesized by Dr. Wenjun Wu with Arkema Coatings Resins (Cary, NC). The latex was synthesized via a surfactant-free emulsion polymerization in a batch reaction scheme similar to the method reported by Grunlan et al.[84] The ratio of MMA:BA in the latex was 48.4:51.6 and the suspension was 17.9 %wt. solids. The reported particle size (Anorak UPA150) was a number average particle size (D_n) of 737 nm, and a polydispersity of (D_v/D_n) of 1.1.

4.2.2 Substrates

The substrates used for these studies are 5 mm x 7 mm silicon chips cut from a standard (100) silicon wafer. For the latex coatings prepared on non-walled substrates, the silicon chips were plasma cleaned and the latex suspension was applied without any further treatment. To fabricate the walled substrates, standard photolithographic techniques were used to pattern photoresist walls onto the silicon chips.

To fabricate the walled substrates, the photoresist, SU-8 2100 (Microchemist Corp.) was spin-coated onto a clean (100) silicon wafer at 500 rpm for 10 seconds followed by 1500 rpm for 30 seconds. The wafer was then "soft baked" at 65°C for 5 minutes and then heated to 95°C for 40 minutes. Using a mask aligner (Suss Microtech), the coated wafer was exposed to UV light for 25 seconds. The post-exposure bake was performed on a hot plate at 65°C for 5 minutes, and 95°C for 15 minutes. To remove the unexposed photoresist, the wafer was developed with glycol monomethyl ether acetate (PM acetate) for approximately 20 minutes or until the undeveloped photoresist was completely removed. Following development, the wafer was baked on a hotplate at 150°C for 15 minutes. After cooling, the wafer was cut into 5 mm x 7 mm pieces with a wafer saw (Disco). The photoresist walls were approximately 280 μm high and 500 μm wide. Figure 4.1 shows a cross-section of the photoresist wall and a schematic diagram of the walled substrates used in this work. The "overhang" which appears in the cross-section image in Figure 4.1 was not universally observed.

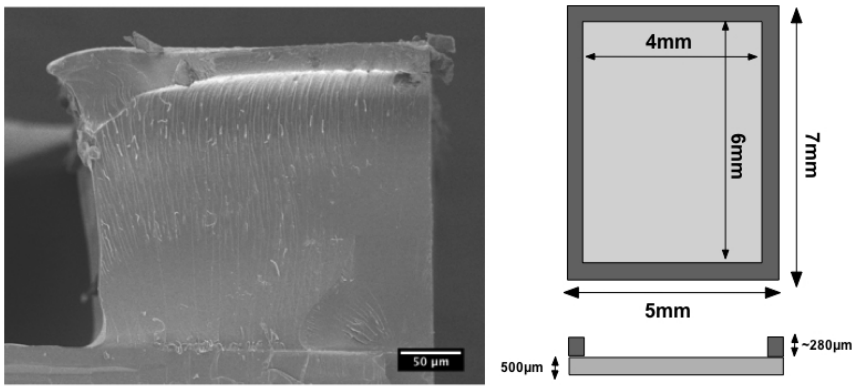

Figure 4.1 Left: Cross-section of an SU-8 wall on a silicon substrate taken by conventional SEM; in this image the edge of the substrate on the right side. Right: A schematic diagram showing the dimensions of the walled substrates.

4.2.3 Digital Microscopy - Hirox

To monitor the appearance coatings during the drying process, a Hirox digital microscope was used. Images were obtained using the MX(G)-MARCOZVI lens at 5x magnification. To monitor the drying process, images were taken every 20 seconds during drying. The samples were illuminated on two sides from above using white light point source illuminators.

4.2.4 CryoSEM

CryoSEM was used to characterize the microstructure development of latex coatings during drying. A micropipette was used to deposit a controlled volume of the latex suspension onto either a non-walled or a walled substrate. For the non-walled substrate, 7 µL was deposited, while 5 µL was used for the walled substrate (filled) case. For the overfilled walled substrates 10 µL was deposited. Figure 4.2 shows schematic diagrams of the three coating conditions studied: non-walled, walled (filled), and overfilled.

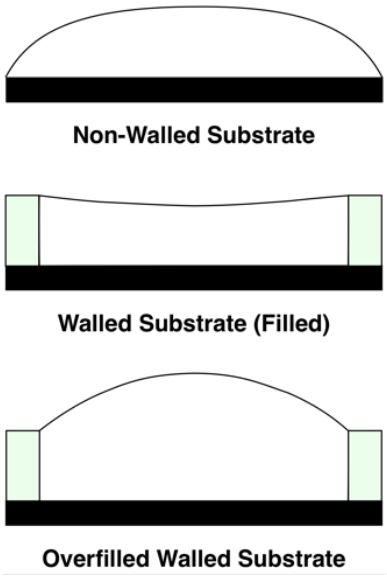

Figure 4.2 Schematic diagram showing the substrate geometries used in this study: non-walled, walled (filled), and overfilled.

To characterize the developing microstructure, the samples were dried in ambient conditions for various times before plunging them into a bath of liquid ethane. By rapidly freezing the sample, particle motion is arrested and the microstructure of the coating is preserved. Once frozen, the samples were placed in a cryoSEM sample holder and transferred to an Emitech K-1250 preparation chamber, which is under high vacuum. The samples were fractured along their mid-section to expose the frozen cross-section. The samples were then sublimed at -96°C for 5 min to etch away some of the frozen matrix, which improves topographical contrast. Approximately 5 nm of platinum were sputter-coated onto the frozen fracture surface to reduce charging. After sample preparation was complete, the samples were transferred to a Hitachi S-4700 FESEM and imaged on a stage cooled by liquid nitrogen.

4.3 *Experimental Results*

4.3.1 *Appearance of Drying Coatings*

As latex coatings dry, they typically undergo dramatic changes in their appearance. The appearance of latex coatings prepared on a non-walled substrate and a walled substrate (filled) are shown in Figure 4.3. Following deposition of the latex suspension, both coatings have a similar opaque appearance. In each image, the non-walled substrate is on the left and the walled substrate is on the right. After two minutes of drying, the coating on the non-walled substrate has a fairly homogeneous appearance (Figure 4.3a). However, with further drying (Figures 4.3b and 4.3c), a slightly brighter region appears near the edges, forming a ring that grows with time, moving toward the center. During this time period, the central region of the coating becomes more translucent. After nine minutes of drying (Figure 4.3c), the center of the coating and the "ring" around it appear slightly opalescent. With continued drying (Figure 4.3d), the coating appears to have a uniform opalescent appearance.

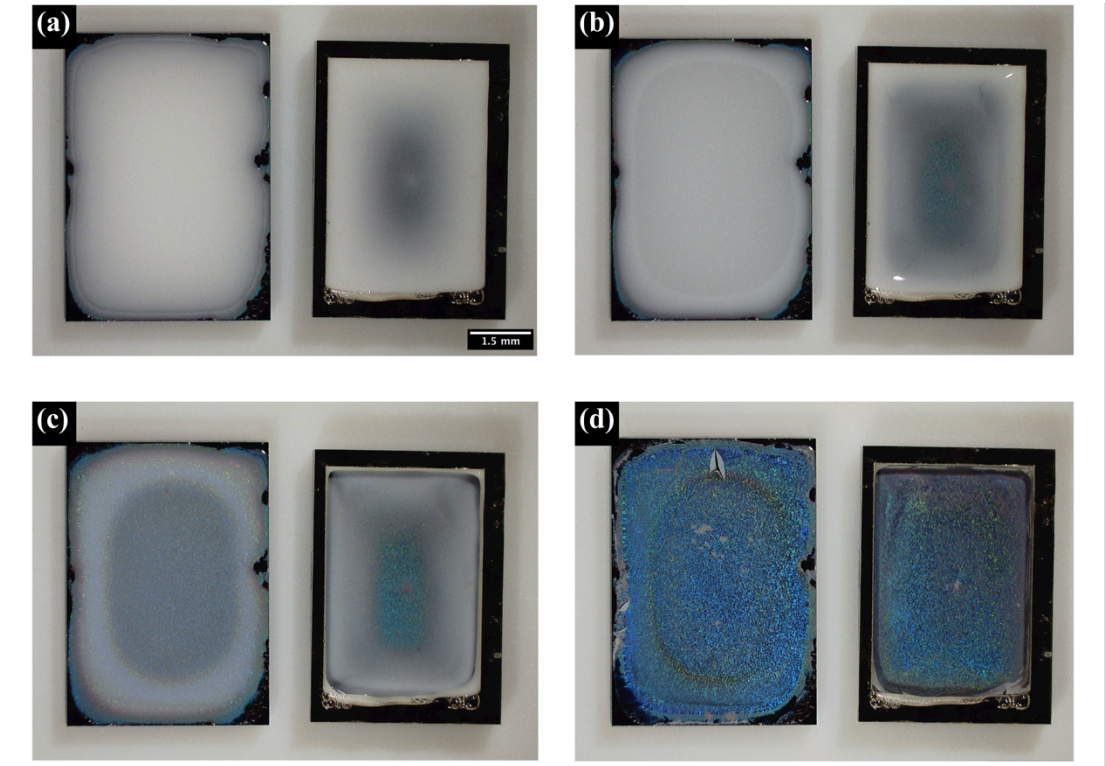

Figure 4.3 Digital micrographs of latex coatings during at (a) 2 min, (b) 7 min, (c) 9 min, and (d) 11 min of drying in ambient conditions. For each, the sample on the left is a non-walled silicon substrate (5 mm x 7 mm) and the sample on the right is a walled substrate (filled).

For the coating dried on the walled substrate, the central region becomes transparent earlier in the drying process than the coating dried on the non-walled substrate (Figures 4.3a and 4.3b). This occurs even though the initial (wet) coating thicknesses were approximately the same for both samples at the start of the experiment. For the coating dried on the walled substrate, a clear region forms near the center that grows outward toward the wall with further drying. After drying for nine minutes, the center of the coating appears clear and opalescent. With continued drying, the coating takes on a uniform opalescent appearance.

4.3.2 *Microstructure Development: Non-walled Substrate*

Figure 4.4 shows a series of cryoSEM cross-sectional images of a coating prepared on a non-walled substrate and frozen after seven minutes of drying. The frozen coating has a drop-like shape, which is expected for coatings prepared on non-walled substrates. It is clear that the coating is thinnest near the edges where the coating liquid meets the substrate. The higher magnification images (Figures 4.4b and 4.4c) clearly reveal the details of the microstructure. In Figure 4.4c, sublimation of ice from the frozen fracture surface has exposed the embedded latex particles, which now protrude from the fracture surface, making them appear bright in the secondary electron images. Additionally, crater-like structures on the fracture surface indicate the location where an embedded latex particle was removed during fracture. Ice, formed by condensation of atmospheric moisture on the surface, and debris, formed during sample preparation and fracture, is also present on the fracture surface. Ice contamination and debris are artifacts of cryoSEM sample preparation and do not indicate microstructural development in the coating.

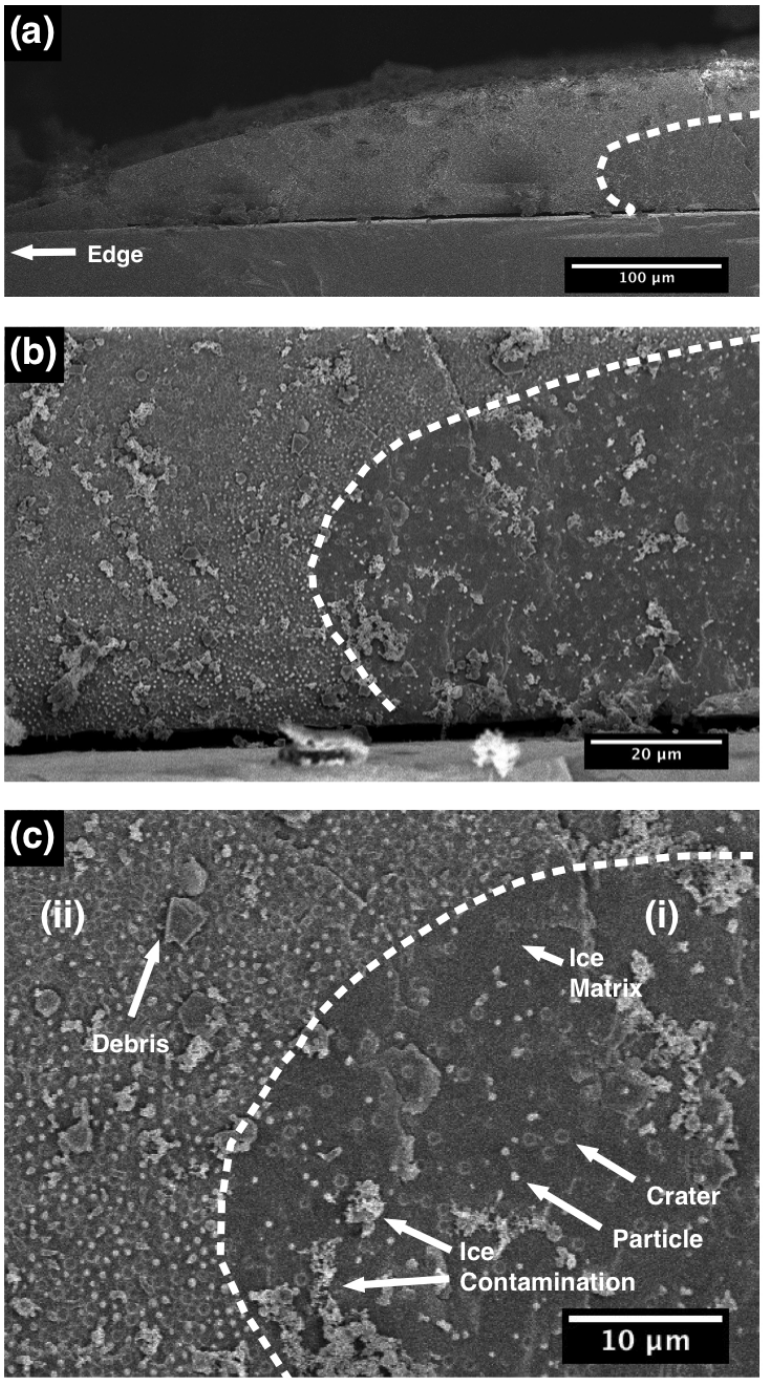

Figure 4.4 CryoSEM images of a latex coating prepared on a non-walled silicon substrate and frozen after seven minutes of drying. The low magnification image (a) shows the region of the coating near the edge of the substrate. The higher magnifications images (b) & (c) show the boundary between the suspended region and the consolidated packing (dashed line).

In Figure 4.4c, two regions are easily identifiable in the microstructure: (i) a suspension of particles in a frozen water matrix, and (ii) a region of closely packed (consolidated) particles with frozen water between them. The boundary between the suspended and consolidated particle regions is referred to as the packing front. Particle consolidation was observed both near the free surface and near the edges as shown in the low magnification images, Figures 4.4a and 4.4b.

Far from the edge, the packing front (dashed line) is horizontal, marking a region of accumulation along the free surface. Accumulation near the edge is marked by a packing front that curves downward toward the substrate. Interestingly, the packing front curves more sharply near the substrate; however, the origin of this behavior is unclear. After seven minutes of drying, the packing front is approximately 405 μm from the edges of the substrate and approximately 31 μm from the free surface as measured through the cryoSEM images.

A cryoSEM cross-section of a latex coating dried on a non-walled substrate for 12 minutes is shown in Figure 4.5. Here, the coating separated from the substrate during the fracture process; the substrate is not visible in the images. Compared to the sample dried for seven minutes (Figure 4.4), the size of the consolidated regions grew both from the top-down and from the edge-in. Measured from the cryoSEM images, the distance from the edge of the substrate to the packing front is approximately 650 μm after 12 minutes of drying. The change in the thickness of the consolidated region near the free surface after 12 minutes was less dramatic; after 12 minutes, the packing front was 42 μm below the

free surface. From Figures 4.4 and 4.5, the free surface near the central region begins to drop as water and particles flow from the central regions to the edges of the coatings.

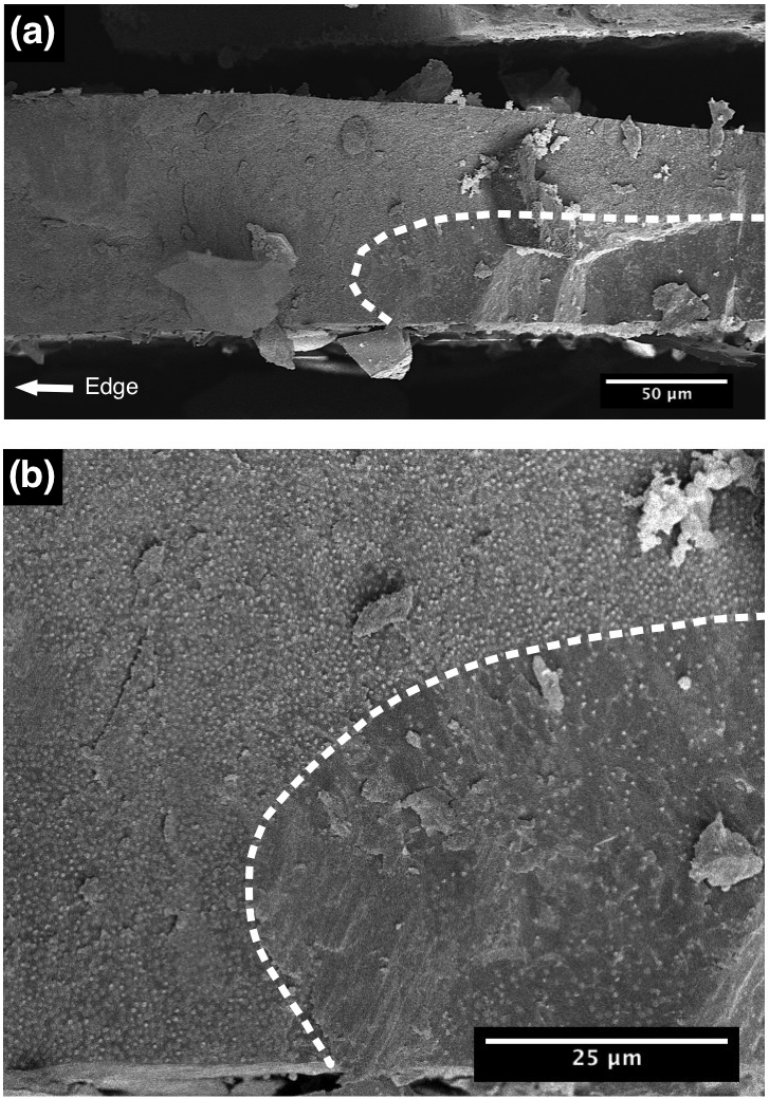

Figure 4.5 CryoSEM cross-sections of a latex coating prepared on a non-walled substrate frozen after 12 minutes of drying. The lower magnification image (a) shows the shape of the free surface. The higher magnification image (b) shows the packing front.

4.3.2 Microstructure Development: Walled Substrate (Filled)

CryoSEM cross-sectional images show the microstructure development for coatings prepared on walled substrates where the liquid just fills the well created by a photoresist wall, see Figures 4.6 and 4.7. After only one minute of drying (Figure 4.6), the free surface of the coating has begun to descend near the center of the coating, but the contact line remains pinned to the wall. The right edge of the coating in Figure 4.6 was originally adjacent to the wall, which is missing from the image as it broke away from the substrate during the fracture process The frozen coating has a curved contour that mimics the wall geometry. Figure 4.6b is a higher magnification image that reveals particle accumulation near the top of the wall and along the free surface of the coating. The consolidated region along the free surface is fairly uniform in thickness (approximately 8 μm), except near the wall where it is slightly thicker.

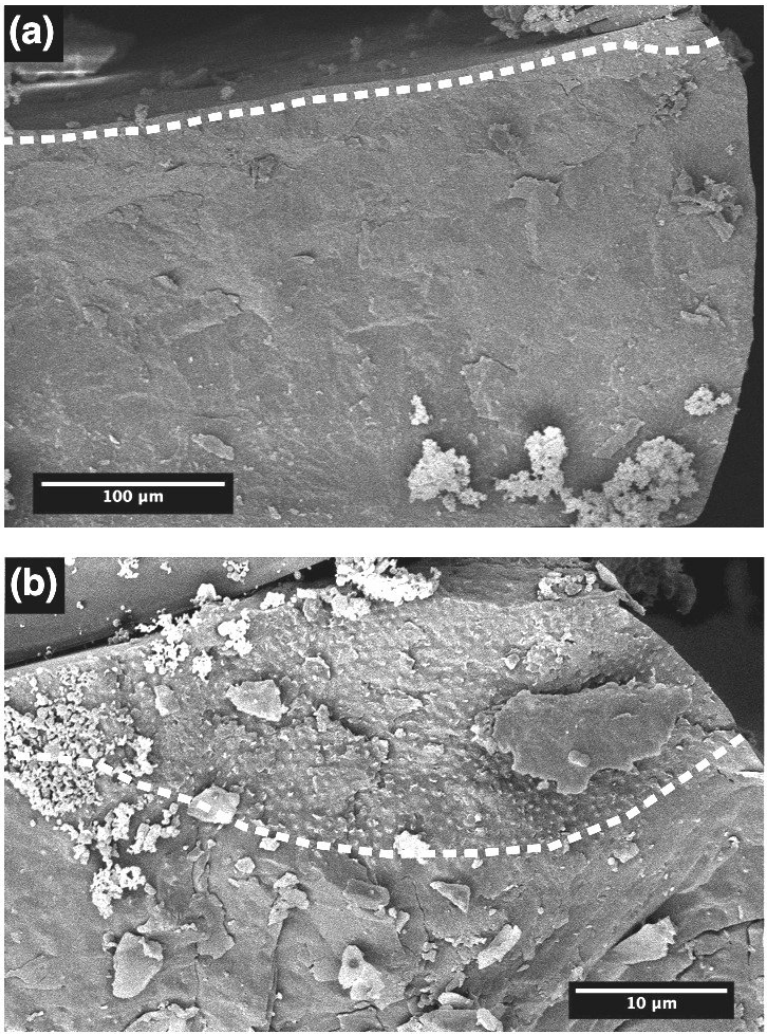

Figure 4.6 CryoSEM cross-section of a filled walled substrate dried for one minute. During fracture the wall detached from the substrate and is missing from the right side of the images.

A frozen cross-section of a coating dried for 12 minutes on a walled substrate (filled) is shown is Figure 4.7. It is evident that the coating remains pinned at the top of the wall, creating the concave shape of the frozen coating. Here, the photoresist wall can be seen in the images; however, during sample preparation, the coating separated from the wall and fractured some distance from it. Away from the wall, approximately 340 µm toward the center, the packing front has reached the substrate. Near the wall, a region of

latex suspension remains below the consolidated packing that formed along the free surface. A curved packing front, similar to the in Figures 4.4 and 4.5, can be seen in the cryoSEM image (Figure 4.7). Figure 4.7b shows the changes in thickness of the consolidated region. Next to the wall, the consolidated packing is approximately 145 μm thick. Far from the wall the particle packing, 41 μm thick, has already reached the substrate.

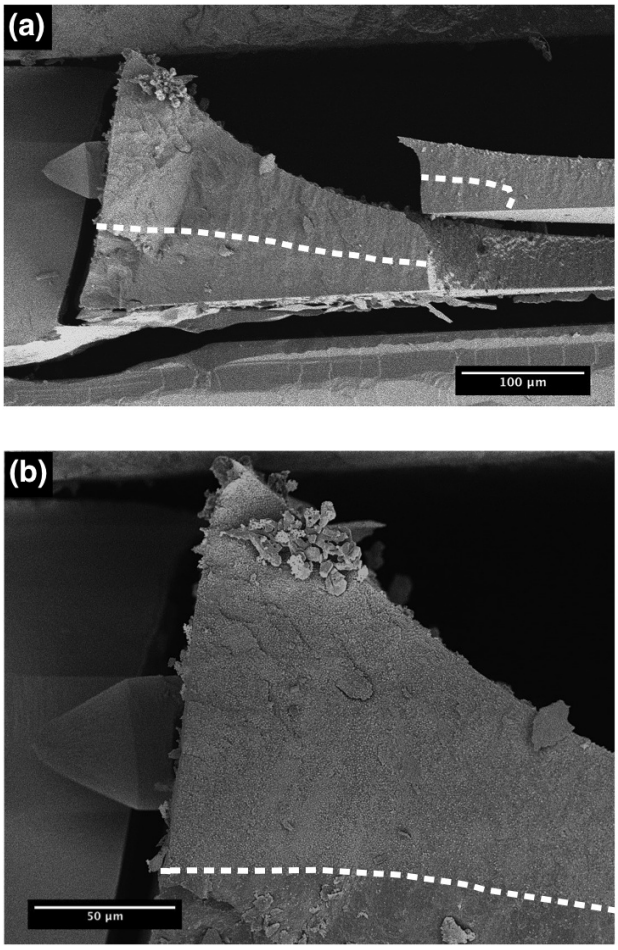

Figure 4.7 CryoSEM cross-section of a walled substrate (filled) frozen after 12 minutes of drying. The lower magnification image (a) shows the pinned contact line and the concave shape of the free surface. The consolidation of particles near the wall is shown in greater detail in (b).

4.3.3 Microstructure Development: Overfilled Walled Substrate

Figures 4.8 and 4.9 show cryoSEM cross-sectional images of coatings prepared on walled substrates were the latex suspension is filled above the level of the photoresist walls. Above the wall, the free surface of the coating forms a convex shape, as shown in Figure 4.2, that resembles the shape of a coating cast on a non-walled substrate. The coating in Fig 4.8 was frozen after 12 minutes of drying. Again, regions of consolidated particles are found both along the free surface of the coating and near the wall. Far from the wall, the consolidated region along the free surface is approximately 35 μm thick; near the wall, the consolidated region is slightly thicker (see Figure 4.8b).

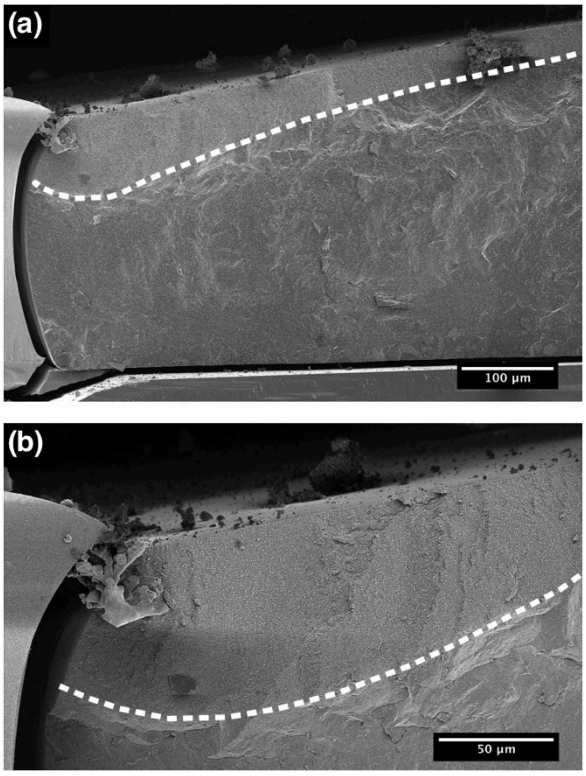

Figure 4.8 CryoSEM cross-sections of a coating prepared on an overfilled walled substrate frozen after 12 minutes of drying. The low magnification image (a) shows the convex shape of the free surface. Greater detail of the coating microstructure near the wall is shown in (b).

A cryoSEM cross-sectional image of an overfilled walled substrate dried for 25 minutes is shown in Figure 4.9. As water evaporates from the coating, the free surface drops below the wall, and the pinned contact line creates the concave free surface as shown in Figure 4.9a. Away from the wall, the particle packing has not yet reached the substrate and no curved packing front is present. One feature to note in Figure 4.9 is the dark region near the substrate, which is believed to form due to local over-sublimation and is considered an artifact of sample preparation.

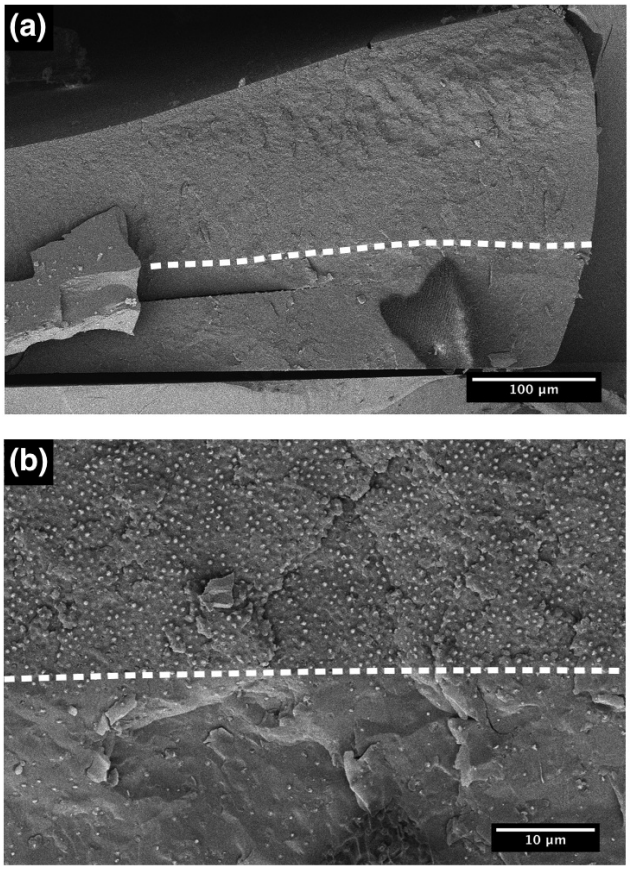

Figure 4.9 CryoSEM cross-section of an overfilled walled substrate frozen after 25 minutes of drying. The lower magnification image (a) shows the shape of the free surface in the later stages of drying. The higher magnification image (b) shows the detail of the coating microstructure.

4.3.4 Fully Dried Coatings

Figure 4.10 shows room temperature SEM images of the edge regions for the fully dried coatings. The area near the edge for a coating dried on a non-walled substrate is shown in Figure 4.10a. A raised "rim" of material can be clearly seen close to the edge of the substrate. This structure is likely a result of the "ring" that developed during drying, shown in the Hirox images, Figure 4.3. This region of thickness non-uniformity is approximately 1.1 mm wide. Near the center of the coating, away from the rim, the thickness is fairly uniform at 20 μm.

Figure 4.10b shows the thickness profile for the coating dried on a walled substrate (filled). Even after drying, the coating remains adhered to the top of the wall, causing the coating thickness to increase dramatically in the vicinity of the wall. Away from the wall, the coating thickness is relatively uniform at 24 μm. The dried thickness profile for an overfilled walled substrate is shown in Figure 4.10c. The thickness profile of this coating is similar to the walled substrate (filled) case; however, the decrease in coating thickness as you move away from the wall is more gradual and the coating thickness is greater near the center (approximate 30 μm). Overall, coatings prepared in the walled substrates display a greater region of uniform coating thickness compared to coatings prepared on non-walled substrates.

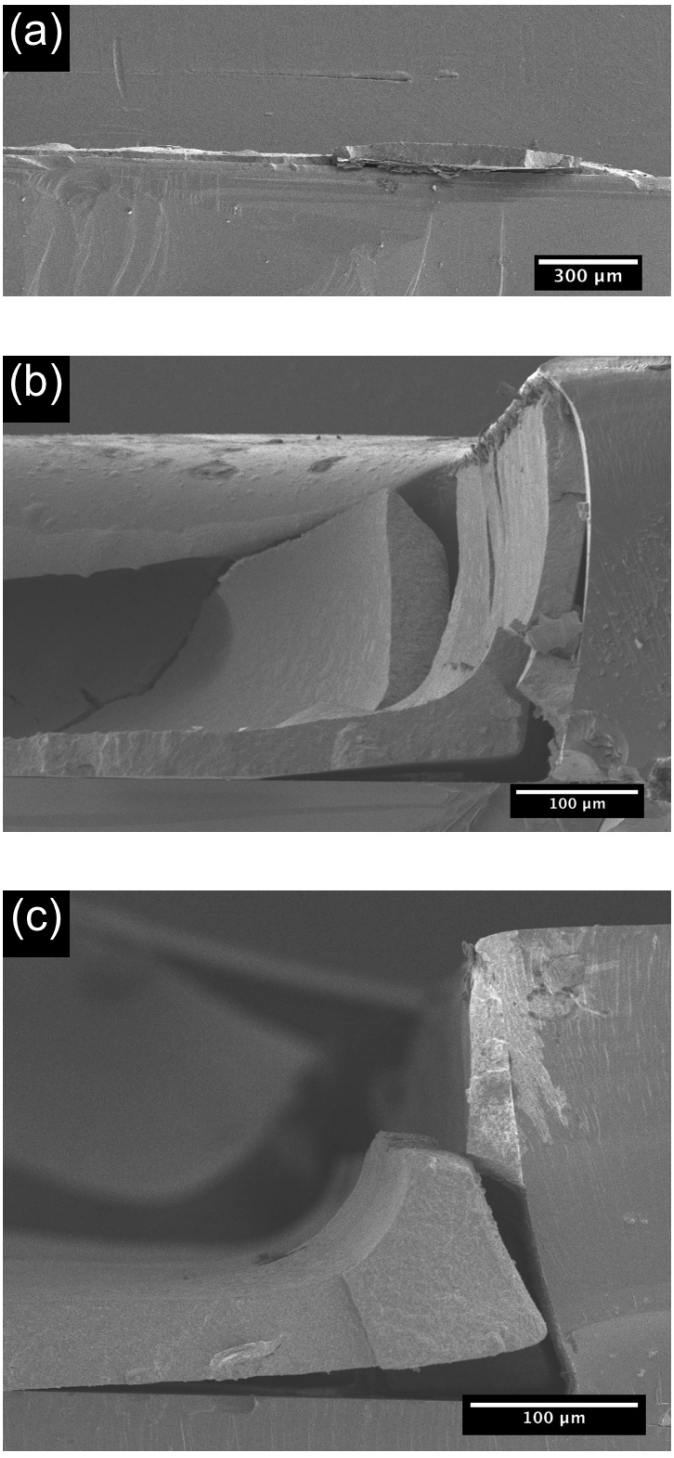

Figure 4.10 Room temperature SEM cross-sections near the edge of fully dried coatings for the a) non-walled substrate, b) filled walled substrate, and c) overfilled walled substrate.

4.4 *Discussion*

The effect of drying geometry on the microstructure development of the latex coatings is discussed in this section. Based on digital microscopy and cryoSEM results, the microstructure development sequence for each of the three coating geometries is shown schematically in Fig 4.11.

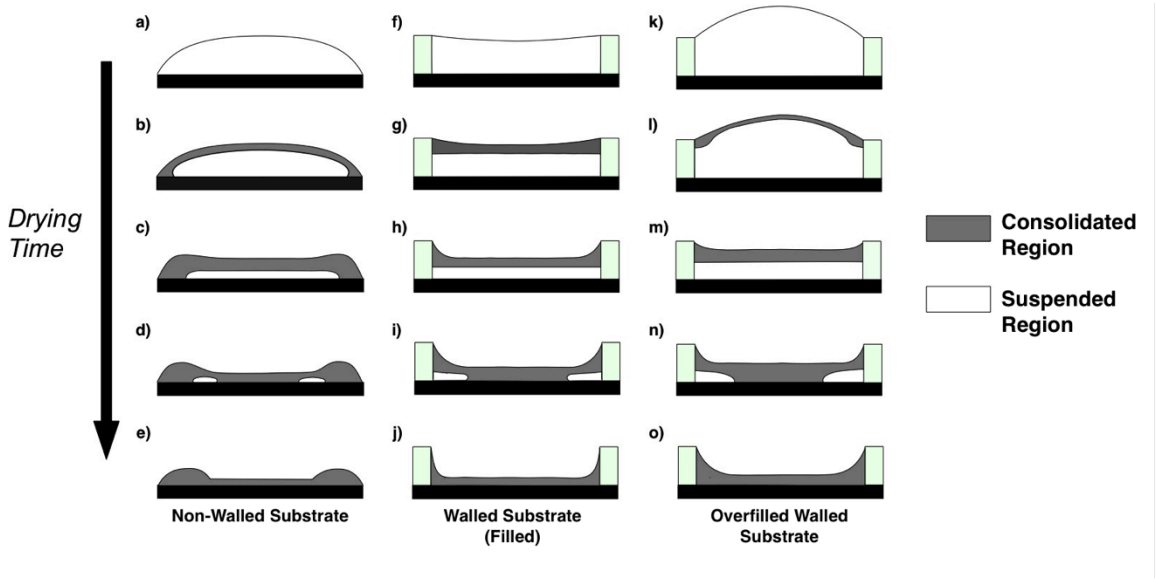

Figure 4.11 Schematic representations of the microstructure development for a latex coating for the three drying geometries: non-walled substrate, walled substrate (filled) , and overfilled walled. The point of contact between the packed region (grey) and the wall is shown at a right angle but was shown experimentally to vary. The intersection of the packed region with the substrate establishes the curved interface as represented.

4.4.1 Non-walled Substrates

First, considering the coating prepared on the non-walled substrate, the initial latex suspension deposited on the substrate has a uniform particle distribution and forms a convex drop shape, as shown in Figure 4.11a. The coating appears opaque (Figure 4.3) due to light scattering from the dispersed latex particles in suspension. As the coating dries, (Figure 4.11b) the latex particles begin to accumulate along the free surface and

near the edges of the substrate, as shown in the cryoSEM images (Figures 4.4 and 4.5). During drying, water evaporates and the free surface descends toward the substrate. The latex particles accumulate along the free surface developing a top-down packing front. As previously stated in Chapter 2, this accumulation can be predicted using the Peclet number, *Pe*, which is defined as[15,21]:

$$Pe = \frac{H\dot{E}}{D_o} = \frac{6\pi\eta R_o H\dot{E}}{kT} \tag{4.1}$$

where, $\dot{E}$ is the evaporation rate, η is the water viscosity, H is the wet coating thickness, R_o is the particle radius, and kT is the thermal energy. The diffusion coefficient, D_o, is approximated for spherical particles by the Stokes-Einstein equation. When $Pe \gg 1$, the evaporation term ($\dot{E}$) dominates the diffusion term (D_o/H) and particles are predicted to accumulate along the free surface. For ambient drying conditions, the evaporation rate can be estimated to be 5 μm/min by weight loss experiments.[85] From Eq. 4.1, the Peclet number for the latex was 39, which predicts particle accumulation at the free surface.

Not only do particles accumulate along the free surface, particle accumulation also occurs near the edges of the coating on the non-walled substrate, as shown in Figures 4.4 and 4.5. Accumulation at the edge is also apparent in the digital microscopy sequence (Figure 4.3), where a brighter rim forms and grows inward as the coating dries. Accumulation near the edges of drying coatings has been observed and studied by many researchers.[42,44,47,86] This "edge effect" may be described generally by the coffee-ring theory proposed by Deegan and coworkers.[42,86] In the theory proposed by Deegan et al.[42], particles pin the contact line of a drying drop. Since the base of the drop cannot shrink, volume lost to evaporation must be replaced by a flow of water from the bulk of the

coating; see Figure 4.12. This flow of water from the central suspended region to the edge also carries particles where they are deposited at the packing front, forming the observed particle packing. Routh and Russel[44] modeled the formation and propagation of particle fronts on non-walled substrates. In their model, the pinned contact line requires the volume fraction of particles near the edge (where the coating is thin) to rise quickly with evaporation. Further evaporation from the edge areas draws water (and particles) from the dispersion to the edge causing the particle front to grow. An important feature observed in the experimental results shown here is the competition between accumulation at the free surface and at the edge.

Due to accumulation at the edge and along the free surface, the packing front develops a curved shape near the edge as shown in Figures 4.4, 4.5, and 4.7. This occurs because the packing front along the surface is parallel to the free surface, which is nearly horizontal; while the accumulation near the edge has a front that one would expect to be vertical. However, this packing front is curved sharply near the substrate. Although the origin of its shape is unclear, one possible explanation is that the free surface compresses the packing front as it descends. In the consolidated regions, water remains between the particles allowing the packing to respond to external forces, possibly changing the shape of the packing front.

As the consolidated regions grow, there exists a competition for the latex particles with some particles being captured by the descending surface, while others are swept to the edges. The consolidated regions near the edge and along the free surface grow as the coating continues to dry. As the volume of the coating is reduced, the height near the

center drops below the height of the packing near the edges (see Figures 4.5 and 4.11c). Particle accumulation near the edges results in the formation of a rim or ring of material along the perimeter of the substrate where the contact line was pinned during drying. The formation and growth of this rim was observed by both digital microscopy (Fig 4.3) and though cryoSEM (Figures 4.4 and 4.5).

Near the center of the substrate, the digital microscopy images reveal that the appearance of the coating changes from turbid and opaque to clear and opalescent. This opalescence is a result of the long-range order formed by the close packing of monodisperse spherical particles.[87] When the central region of the coating begins to clear, the packing on the free surface has reached the substrate and there is no longer a liquid suspension beneath. At this point, the growth of the rim stops, as shown in Figure 4.3 and also schematically in Figure 4.11d. As the remaining water evaporates, the entire coating appears opalescent (See Figure 4.3d). A schematic representation of the fully dried coating is shown in Figure 11e.

A cross-section of the fully dried coating on a non-walled substrate, Figure 4.10a, confirms that accumulation near the edge results in a non-uniform coating thickness. The coating thickness near the center is approximately 20 μm whereas the thickness of the rim is approximately 65 μm. The non-uniform regions near the edges cover nearly 45% of the entire coating cross-section length.

4.4.2 Walled Substrates

For the walled substrates, two conditions were studied: the filled case and the overfilled case. For the filled case, the coating suspension takes the initial shape shown in Fig 4.11f. The presence of the photoresist wall makes the initial coating thickness fairly uniform. As the coating begins to dry, Fig 4.11g, evaporation causes the free surface to descend and particles to accumulate along the free surface. Accumulation near the wall early in the drying process is shown in the cryoSEM micrographs in Figure 4.6.

Away from the wall, the free surface descends and particles accumulate due to the high Peclet number as described previously. However, at the wall, the contact line remains pinned and does not descend during drying. Interestingly, the thickness of the particle packing near the wall is thicker than in the center of the coating where the free surface is mobile. Near the wall, particles do not accumulate due to a descending free surface; instead, particles must be transported by flow from the bulk of the coating to the wall. Particle accumulation near the pinned contact line can by described by a vertical case of the coffee-ring theory discussed for the non-walled substrate.[88]

Near the wall, contact line pinning restricts the ability of the coating to shrink in response to evaporative losses. Consequently, for the contact line to remain pinned, a flux of water from the bulk must replace the volume of water lost to evaporation near the wall; see Fig 4.12. As water flows toward the wall, particles are transported to the wall and the consolidated packing near the wall grows. Flow towards the wall is consistent with results obtained for polymer solutions dried in walled substrates.[73,77,82] Near the center of the substrate, away from the walls, volume is lost to local evaporation and also

to lateral transport toward the walls. The consolidated packing in the center of the coating reaches the substrate first, as shown in Figure 4.7 and schematically in Figure 4.11i. In the digital microscopy sequence (Figure 4.3), the coating on the walled substrate achieves a clear appearance first near the center that expands outward (toward the walls) during drying.

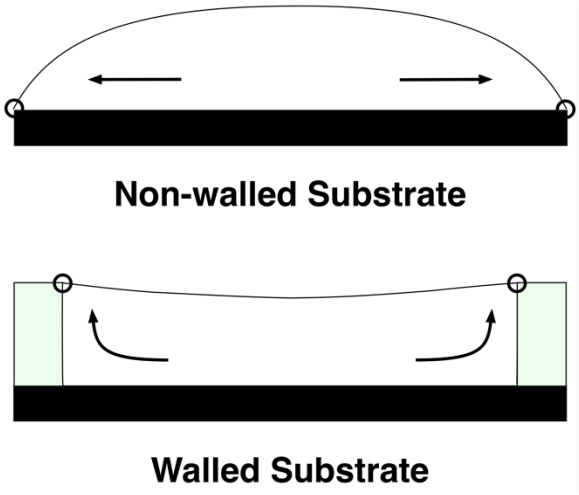

Figure 4.12 Schematic diagram of contact line pinning (circles) and flow within the coating marked by solid lines for coating dried no non-walled substrates and walled substrates.

A cross-section of the fully dried coating for the case of the filled walled substrate is shown in Figure 4.10b and schematically in Figure 4.11j. Even after drying, the coating remains pinned to the top of the photoresist wall. The coating thickness decreases from 300 μm at the wall to approximately 50 μm thick at a distance of 200 μm from the wall. The coating thickness reduces gradually to 25 μm far from the wall. The regions of non-uniform thickness near the wall make up approximately 16% of the entire coating cross-section length.

One might hope that providing more suspension near the center of the substrate may compensate for migration to the edges. Therefore, the third condition, an overfilled walled substrate was studied. In this case, the free surface of the coating forms a convex shape, shown schematically in Figure 4.11k. For the early drying times, the convex shape resembles a coating deposited on a non-walled substrate. The coating is pinned near the edges at the top of the wall throughout the drying process (See Figures 4.8 and 4.9). As water evaporates, cryoSEM results show that particles accumulate at the both along the free surface and near point of contact line pinning, Figure 4.11l.

As drying continues, the volume of the coating decreases and the free surface drops below the height of the wall. At this stage of drying, Fig 4.11m, the shape of the coating resembles the filled walled substrate geometry. With further drying, particles accumulate near the walls due to the pinned contact line. Again, the particle packing far from the wall reaches the substrate first as shown schematically in Figure 4.11n.

A cross-section of the fully dried coating for the overfilled walled substrate case is shown in Figure 4.10c, and schematically in Figure 4.11o. Despite having a greater wet thickness far from the wall, the final dried coating had similar profile to the filled walled substrate case. The thickness of the dried coating far from the wall in the overfilled case is approximately 30 μm. The regions non-uniform thickness near the wall extends out approximately 300 μm, comprising 24% of the coating cross-section length.

4.5 *Summary*

This chapter investigated the influence of the walled substrate geometry on the drying uniformity for latex coatings. In this study, digital microscopy and cryoSEM were used to characterize the development of the coating microstructures for three drying conditions: a non-walled substrate, a filled walled substrate, and an overfilled walled substrate. CryoSEM revealed that the microstructures of these coatings do not develop uniformly. The results confirm the existence of competing packing fronts near the edges or walls and along the free surface. In all cases, pinning of the contact line generates lateral transport of water and particles. For coatings dried on non-walled substrates, our results support the models of microstructure development predicted by others.[42,44,86] For the walled substrate cases, the principles of contact line pinning are extended to explain how pinning at the top of a wall generates non-uniformities in the final coating. However, for the particular coatings and drying conditions studied here, the final dried coatings in walled substrates are more uniform than coatings dried on a non-walled substrate. The results also point to possible directions for improving uniformity, including modifying wall surfaces to prevent pinning and increasing suspension loading to slow particle migration to the edges.

Chapter 5

STRESS DEVELOPMENT IN HARD PARTICLE COATINGS[2]

5.1 *Background and Motivation*

Hard particles coatings are used in a variety of industrial applications including battery electrodes,[20,81] nanoparticle inks,[89,90] photonic crystals,[91,92] and antireflective coatings.[3] The particles may be metal nanoparticles (Ag, Au) used in metallic inks for printed electronics, high glass transition (T_g) latex particles, or ceramic particles like silica particles used to make photonic crystals and anti-reflective coatings. To manufacture these coatings, the typical process is to apply a fluid colloidal suspension onto a substrate and allowing the coating to dry. Drying is a crucial processing step that influences the thickness uniformity of the coating, the coating microstructure, and the formation of coating defects. Stress development in the coating during drying has the potential to generate defects like cracking, curling, warping and delamination, which are detrimental to the coating performance. Achieving optimal performance from these

[2] An adapted form of this chapter is in preparation:
Price, K., Wu Y., McCormick, A., Francis, L. *Stress Development in Hard Particle Coatings in the Absence of Lateral Drying*, Journal of the American Ceramics Society (In Preparation)

materials requires a fundamental understanding of how the drying process is related to stress development in the film.

Stress development has been investigated for various coating systems, including ceramic films,[27,43,58,93] latex particle suspensions,[57,60,61,94–97] and coatings made from ceramic particles and organic binders.[62,98–101] Past studies on stress development in hard particle coatings offer a basis on which to describe the origins of stress development during drying. Chiu and Cima[43,93] investigated both the stress development and the cracking behavior of films made from electrostatically stabilized suspensions of alumina particles. The authors investigated the influence of various experimental parameters on the critical cracking thickness (CCT), the thickness at which the films to form cracks spontaneously during drying. For coatings cast on rigid substrates, the variables that had the greatest impact on the cracking behavior were the particle size, liquid surface tension, and the degree of particle aggregation. Additionally, they proved the importance of the substrate on stress development by showing that coatings cast on a pool of mercury did not form cracks during drying. This experiment demonstrated that stress gradients alone do not result in cracking, because these gradients would be present regardless of the substrate. Therefore, they conclude that cracking is mainly a results of the constrained in-plane shrinkage generating a biaxial tensile stress in the coating.

Second, the authors investigated the influence of the capillary pressure in the liquid to the measured stress in the coating. They found that the maximum stress in the films was proportional to the liquid surface tension and inversely dependent on particle size, supporting a capillary origin for stress development. From weight loss

measurements, it was also shown that the stress maximum occurred when the ceramic film reaches 100% saturation.

In a related study, Guo and Lewis[58] conducted *in-situ* measurements of the drying stress for coatings of silica particle suspensions with various degrees of particle aggregation. The degree of aggregation affects the pore structure in the coating and the capillary pressures that are achievable during drying. Their results also support a capillary origin for stress development in these coatings. Using conventional SEM, the authors also demonstrated the importance of particle aggregation on the final microstructure of the coating. Coatings made from flocculated (aggregated) particles contain larger pores than coatings made from dispersed particles. They also concluded that the measured stress is the coating was comparable to the estimated microstructure-dependent capillary pressure. Stress measurements have also been conducted for coatings of zirconia[99] and calcium carbonate[98] particles, which have arrived to similar conclusions on the capillary origins of stress development.

Stress development in the film is often measured by monitoring the curvature or deflection of a rigid substrate though optical interference methods,[43,58,99] capacitive deflection measurements,[27,101] or with a laser-photodiode combination. [60–62,96–98,100] Measurements of the substrate deflection can then be used to estimate the stress in the coating. Improving on the work by Stoney,[54] a useful expression was developed by Corcoran[19]:

$$\sigma = \frac{dE_s {t_s}^3}{3t_c L^2 (t_s + t_c)(1 - v_s)} + \frac{dE_c (t_s + t_c)}{L^2 (1 - v_c)} \qquad (5.1)$$

where E is the Young's Modulus, t is the thickness, L is the cantilever length, v is the Poisson's ratio, d is the deflection of the cantilever, and the subscripts s and c denote the substrate or coating, respectively. Applying the full form of the Corcoran equation (Eq. 4.1) requires one to know the mechanical properties of the coating, which are dynamic quantities that develop during drying and are difficult to measure experimentally. Because of this, experimental conditions are often chosen so that the second term in equation can be neglected without introducing significant error.[55,56]

Interpretation of stress measurements in particle-based coatings is often complicated by laterally non-uniform drying behavior. [43,44,58,93,99] Drying often occurs first at the edges of the substrate where the coating is thinnest, and then propagates inward from the edge; this phenomenon is commonly known as lateral drying. In the case of lateral drying, stress development does not occur uniformly across the substrate. Using a deformable membrane, Koenig and Johannsmann[57] observed the local fluctuations in stress during lateral drying and demonstrated that stress development in the film is highest at the position of the drying front. Unfortunately, substrate-deflection techniques, like that used in this work, cannot account for variations in stress development; only an average stress can be calculated from a measurement of substrate deflection. This limitation complicates the interpretation of stress measurement data using substrate-deflection technique in the presence of lateral drying.

Uniform drying can be promoted under certain experimental conditions.[43,49,99,102] However, even under these circumstances the microstructure of the coating often develops non-uniformly. Roth and Russel[44] proposed a theoretical model for the

formation and propagation of a lateral drying front. They predict that slower evaporation rates, thinner coatings, and larger particle sizes will promote a condition of uniform saturation before drying occurs. Their predictions were confirmed experimentally by Salamanca et al.[49] Controlling lateral drying by manipulating the experimental conditions in order to achieve saturation can be successful for specific cases. However, approaching the problem in this way limits the system variables and processing conditions that can be accessed experimentally.

Drying uniformity can also be promoted by a border along the perimeter of the substrate.[73,77,79,80,103] The border promotes uniform drying by eliminating the thin edges present without the border, and allows the microstructure to develop uniformly across the substrate. In Chapter 4, cryoSEM was used to show that the use of walled substrates leads to greater drying uniformity in latex coatings. In this Chapter, the effects of lateral drying on stress measurement will be explored through the use walled cantilevers. Model systems of electrostatically stabilized ceramic particles (alumina, silica) will be used for these studies.

Past studies indicate that stress development is dependent upon the degree of saturation in the coating. However, these conclusions were established without direct high-resolution imaging of the wet coating microstructure.[43,58,99] Using cryoSEM, the microstructure development of the coatings can be imaged during the intermediate stages of drying. [10,15,67,104] CryoSEM reveals the distribution of frozen water (degree of saturation) within the coating and provides direct evidence for the origins of stress development in hard particle coatings.

This chapter explores the stress and microstructure development in drying ceramic particle coatings using a modified cantilever deflection technique and cryoSEM. Using walled cantilevers to limit lateral drying, stress measurements are conducted without the complications imposed by lateral drying. The stress measurements are coupled with cryoSEM characterization to reveal the evolution of the coating microstructure, the degree of saturation in the particle network, and the impacts on coating stress.

5.2 *Materials and Methods*

5.2.1 Ceramic Particle Suspensions

Aqueous suspensions of alumina particles were prepared from a commercial powder (Ceralox SPA-0.5). As reported by the manufacturer, the particle size distribution ranges from 0.2 μm to 0.8 μm with an average particle size of 0.4 μm. A 20 vol% alumina suspension was prepared by adding the dry alumina powder, as-received, to distilled water, adjusting the pH to 4.0 with nitric acid, and the sonicating for 20 minutes. After sonication, the pH was readjusted to 4.0 and the suspension was stirred on a magnetic stir plate. Prior to coating, the suspension was sonicated for approximately five minutes.

Aqueous dispersions of silica particles were prepared in a similar manner. Monodisperse spherical silica particles (diameter, d=1.01 μm and d=1.57 μm) were purchased from Polysciences, Inc. (Warrington, PA). Smaller 500 nm diameter particles were synthesized using a standard Stöber synthesis procedure[105]. For all particle sizes,

silica suspensions, 30 vol%, were prepared by adding the dry particles to distilled water and adjusting the pH to 9.0 with an ammonium hydroxide solution. The suspensions were sonicated in five-minute increments until the particles were dispersed. Prior to coating, the suspensions were sonicated for a minimum of five minutes.

5.2.2 Stress Measurement

The evolution of stress in the coating during the drying process was monitored *in-situ* using a cantilever beam deflection technique. Details of the experimental apparatus can be found in Chapter 3, a schematic diagram of the experimental apparatus is shown in Figure 3.2. Silicon cantilevers (6 mm x 60 mm) were cut from (100) silicon wafers. The Young's modulus and Poisson's ratio of the cantilevers were taken to be E = 169 GPa, v = 0.064, repectively.[106] For standard cantilevers, the coating suspensions are applied directly to the silicon cantilevers; walled cantilevers were also prepared for these studies.

Based on the results from previous experiments with rope caulk borders,[8] and substrates with photoresist walls,[51] see Chapter 4, walled cantilevers were developed with photoresist walls (SU-8 2100, MicroChem Corp.), in a procedure similar to that outlined in Section 4.2.2. However, initial investigations of stress development with these cantilevers revealed that the photoresist swells when exposed to water. This causes the walls to expand and the cantilever to deflect downward, which would suggest a compressive stress in the coating, see Fig 5.1. However, as shown in Figure 5.1, depositing distilled water onto the cantilever with photoresist walls yielded the same response. Hence, poly(dimethy siloxane) (PDMS, Sylgard® 184, Dow Corning) was

chosen as the wall material because of its low Young's modulus, good adhesion to silicon, and low water absorption.

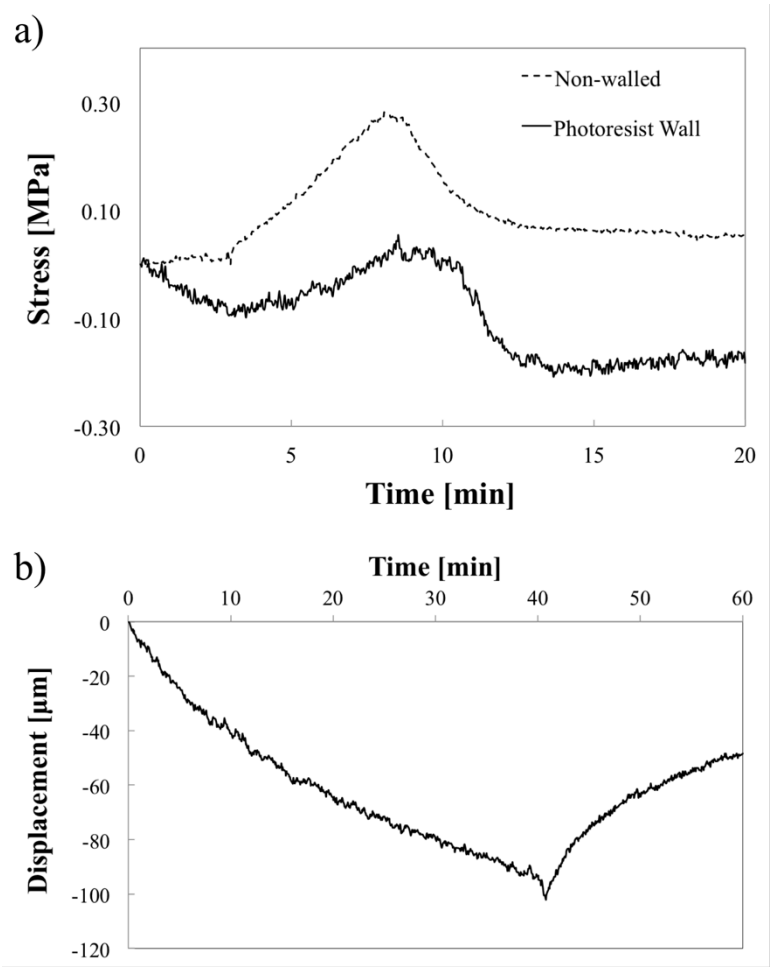

Figure 5.1 a) Plots for the stress development of an aqueous latex coating prepared on a standard cantilever and a cantilever with photoresist walls. b) Plot showing the displacement measured on the photodiode for only water deposited on a cantilever with photoresist walls.

The walled cantilevers used for the stress measurements in this study were fabricated by molding PDMS walls onto silicon cantilevers, Figure 5.2a. The PDMS was prepared according to the specifications of the manufacturer and was used to completely fill the aluminum molds. Prior to placing the silicon cantilevers onto the mold, the

cantilevers were plasma cleaned (Harrick Plasma) for 15 seconds, which promotes adhesion of the PDMS to the silicon surface. The cleaned silicon cantilever was then positioned on the mold and cured at 100°C for 1 hour. After curing, the cantilevers with PDMS walls were removed from the mold and any excess PDMS was manually removed. The PDMS walls have semi-circular cross-section, are approximately 300 µm high, and form a perimeter around the free end of the cantilever (6 mm x 45 mm), see Figure 5.2.

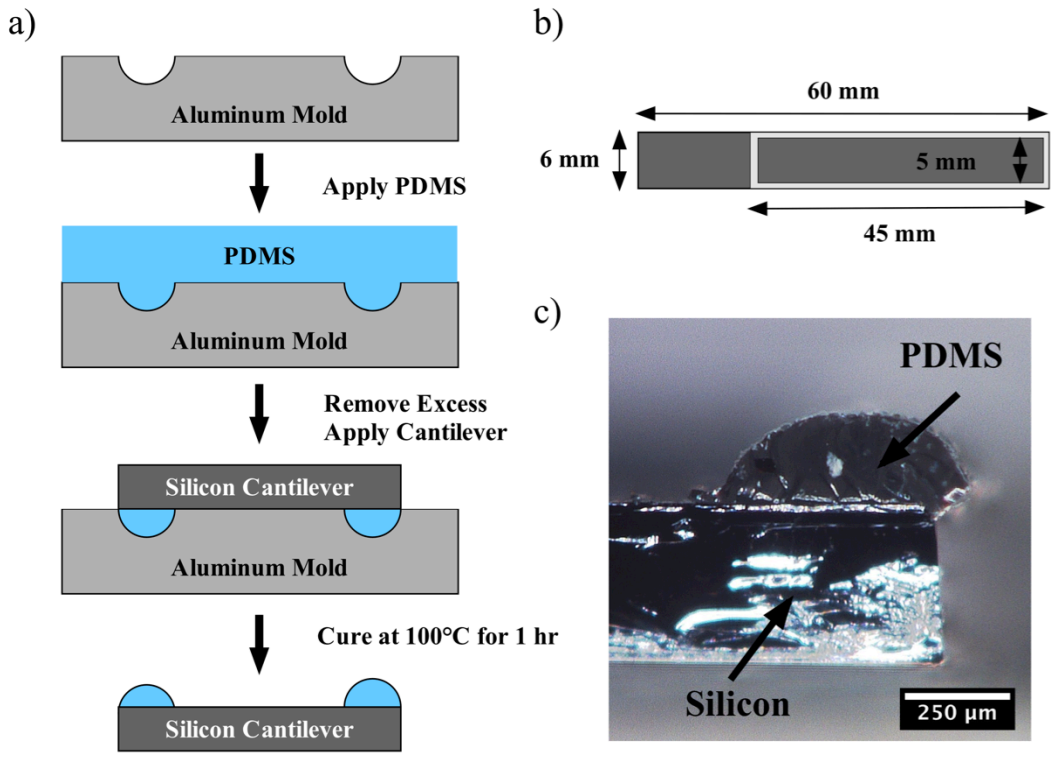

Figure 5.2 a) Schematic diagram showing the fabrication procedure for the silicon cantilevers with PDMS walls. b) Schematic top-view of the walled cantilevers showing the dimensions of the cantilever and location of the PDMS walls. c) Photograph showing the semi-circular cross-section of the PDMS wall on the silicon cantilever.

The stress measurement procedure involves several steps and was discussed at length in Chapter 3. For these studies, approximately 40 µL of the suspension were

applied to the cantilever using a micropipette. The relative humidity and temperature in the controlled environment chamber were maintained at 21°C ± 1°C, and 40%RH ± 2%, respectively during the experiments. A video camera positioned above the drying cantilever in the controlled environment chamber was used to observe the appearance of the coating on the cantilever simultaneously during the stress measurement.

Following the experiment, the dried coating thickness as measured with a micrometer. The final dried thickness of the coating was used to calculate the coating stress according to Eq. 5.1. The dried coating thicknesses in these experiments ranged from 30-100 μm. The use of the dried coating thickness in the stress calculations is reasonable because stress development is assumed to begin only after the particles have formed a consolidated network. After consolidation, only small changes in the coating thickness are expected. Due to the reasons outlined in Chapter 3, the second term of Eq. 5.1 was not used to calculate the coating stress for the results presented here.

5.2.3 Microstructure Characterization

CryoSEM was used to characterize the development of the wet coating microstructure throughout the drying process. Coatings prepared on cantilevers with PDMS walls were dried for various times before plunge freezing into a small container of liquid ethane surrounded by a bath of liquid nitrogen. Due to the use of liquid ethane as the cryogen, the plunge freezing procedure was carried out in a fume hood for safety. Freezing arrests the drying process, preserves the native microstructure, and allows imaging in the high vacuum environment of the SEM. After freezing, the samples were

fractured to expose their cross-sections and transferred to an Emitech K-1250 (Emitech, Kent, UK) preparation chamber. No intentional sublimation was performed for these samples so that the frozen water in the coatings could be imaged. Approximately 5 nm of platinum were sputtered coated onto the frozen fracture surfaces to reduce charging. After coating, the samples were transferred to a Hitachi S-4700 FESEM (Hitachi, Pleasanton, CA) and imaged at approximately -150°C on a liquid nitrogen cooled stage.

5.3 *Results and Discussion*

5.3.1 Walled Cantilevers and the Corcoran Equation

Corcoran[55] developed a useful expression, Eq. 5.1, for relating the curvature or deflection or a coated substrate to the average stress in the film. Several critical assumptions are made during the derivation of Eq. 5.1, which includes a uniform state of stress in the coating. The derivation also assumes that the coating covers the entire surface of the cantilever beam. When walled cantilevers are used, both the wall material (PDMS) and the reduction of coated area on the cantilever due to the wall will impact the deflection of the coated cantilever and hence the calculated stress. To explore the influence of the PDMS walls on the deflection of the coated cantilever, Yan Wu, a graduate student at the University of Minnesota, conducted finite element simulations (ANSYS) for coated cantilevers with and with PDMS walls.

The simulations were based on a thermal stress model in ANSYS where stress is generated through constrained shrinkage of the coatings due to a mismatch in the thermal expansion coefficients of the coating and the substrate. The details of the simulations

were chosen so that the simulations closely match the conditions of the cantilevers used experimentally. To simplify the thermal stress model, the thermal expansion coefficients for silicon and PDMS were set to zero, while the thermal expansion coefficient for the coating and the temperature change were chosen to yield a deflection similar to those measured experimentally. The width of the silicon cantilever (6.0 mm) was fixed, while the PDMS walls in the used in the simulations have a square cross-section with a height of 200 μm and a variable width between 0 – 1.0 mm.

To understand influence of both the PDMS walls and the reduction in coating area on the deflection, three conditions were simulated: a fully coated cantilever, a cantilever with a reduced coating area (no coating where PDMS wall would be), and a coated cantilever with PDMS walls, see Fig 5.3a. The simulation results are summarized in Figure 5.3b, where the ratio of deflection for the cantilever with reduced area (with and without walls) and the fully coated cantilever is shown as a function of the wall width. From Figure 5.3b it can be seen that the PDMS itself has little effect on the deflection of the cantilever. However, the reduction in coated area due to the presence of the wall results in smaller cantilever deflections compared to the fully coated cantilever. For example, 0.5 mm wide PDMS walls are used experimentally have a ratio of deflection that is approximately $d_{walled}/d_{fully\ coated} = 0.82$.

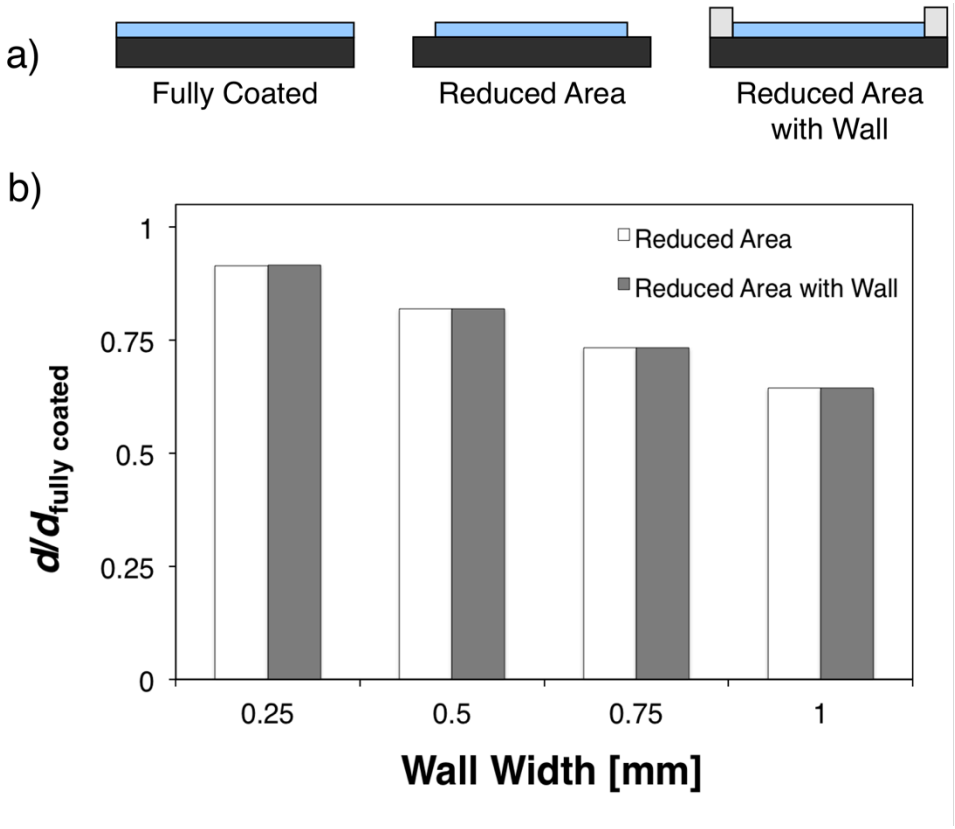

Figure 5.3 (a) Schematic diagrams for the three conditions simulated using finite element analysis (b) Simulation results plotting the ratio of the deflection of the reduced area coatings (with and without PDMS walls) to the deflection of the fully coated cantilever as a function of wall width.

The deflection, *d*, used in Eq. 5.1 assumes that the cantilever is fully coated. Therefore, simply inputting the deflections measured for the walled cantilever will result in an underestimation of the true coating stress. To account for this, a correction factor of, $d_{fully\ coated}/d_{walled}$ = 1.22, was determined from the simulation results for the 0.5 mm wide PDMS walls. As a further step a relationship was derived which accounts for the affect of the reduction in coated area caused by the wall:

$$\sigma_{avg} = \frac{Et^3 d}{3cL^2(1-v)(t+c)} \left(\frac{w_s}{w_c}\right) \tag{5.2}$$

where σ_{avg} is the average stress in the coating, w_s is the width of the cantilever, and w_c is the width of the coating. This results is similar to correction factors used by others conducting stress measurements on standard cantilevers that are not fully coated.[96,97] Equation 5.2 is essentially the first term of Eq. 5.1 with the additional term (w_s/w_c); a full derivation of Eq. 5.2 can be found in Appendix A. Because of the experimental conditions used for these experiments (i.e., $E_s >> E_c$, $t_s >> t_c$), the second term in Eq. 5.1 was omitted for this analysis. For the walled cantilevers used here, the correction factor, $w_s/w_c = 1.20$. This factor accounts for the area of the coating along the long edges of the cantilever, but does not account for the reduced area along the short edges. For the range of wall widths investigated with finite element simulations, the ratio of deflections, $d_{fully\ coated}/d_{walled}$, and the correction term in Eq. 2, w_s/w_c, agree to within 3%. For the stress measurement results presented in this Chapter, Eq. 2 was used to calculate the coating stress.

5.3.2 *Drying and Stress in Alumina Particle Coatings*

Throughout the drying process the appearance of the alumina coatings changes due to differences in the efficiency of light scattering from the coatings.[43,58,99,107,108] The effects of light scattering were also discussed for latex particle coatings in Chapter 4. The photographs shown in Figure 5.4 show these appearance changes for an alumina particle suspension dried on a silicon cantilever without walls. The series of photographs plainly demonstrations that for a cantilever without walls (standard cantilever), the coating dries non-uniformly from the edges inward. The images also show clearly that drying occurs preferentially from the end of the cantilever compared to the long edges.

Several models predict the maximum dimensions of the coating that can be sustain a condition of saturation without the formation of a pore-emptying or drying front.[43,44] In this case, the long dimension of the cantilever is above that critical dimension and a drying front forms at the ends of the cantilever. Three separate regions are identifiable in Figure 5.4 based on the appearance of the coating: a suspended region, a consolidated region, and a dry region.

The suspended region has a similar appearance to the original dispersion and forms the central region of the coating. It is presumable that in the suspended region, the particles are evenly dispersed and that the coating is fluid. With further drying, another region forms that surrounds the suspended region, and has a more translucent appearance. It is assumed that in this region, the particles have formed a touching network but remain saturated with water; this area is defined as the consolidated region. In the later stages of drying, Figure 5.4d, a more opaque region develops just outside the translucent consolidated region. When the pore structure of the coating begins to empty, air invasion into the particle network increases the difference in the index of refraction that leaves the coating with an opaque appearance. Because the pores are presumed to be emptying, the opaque area of the coating is defined as the dry region.

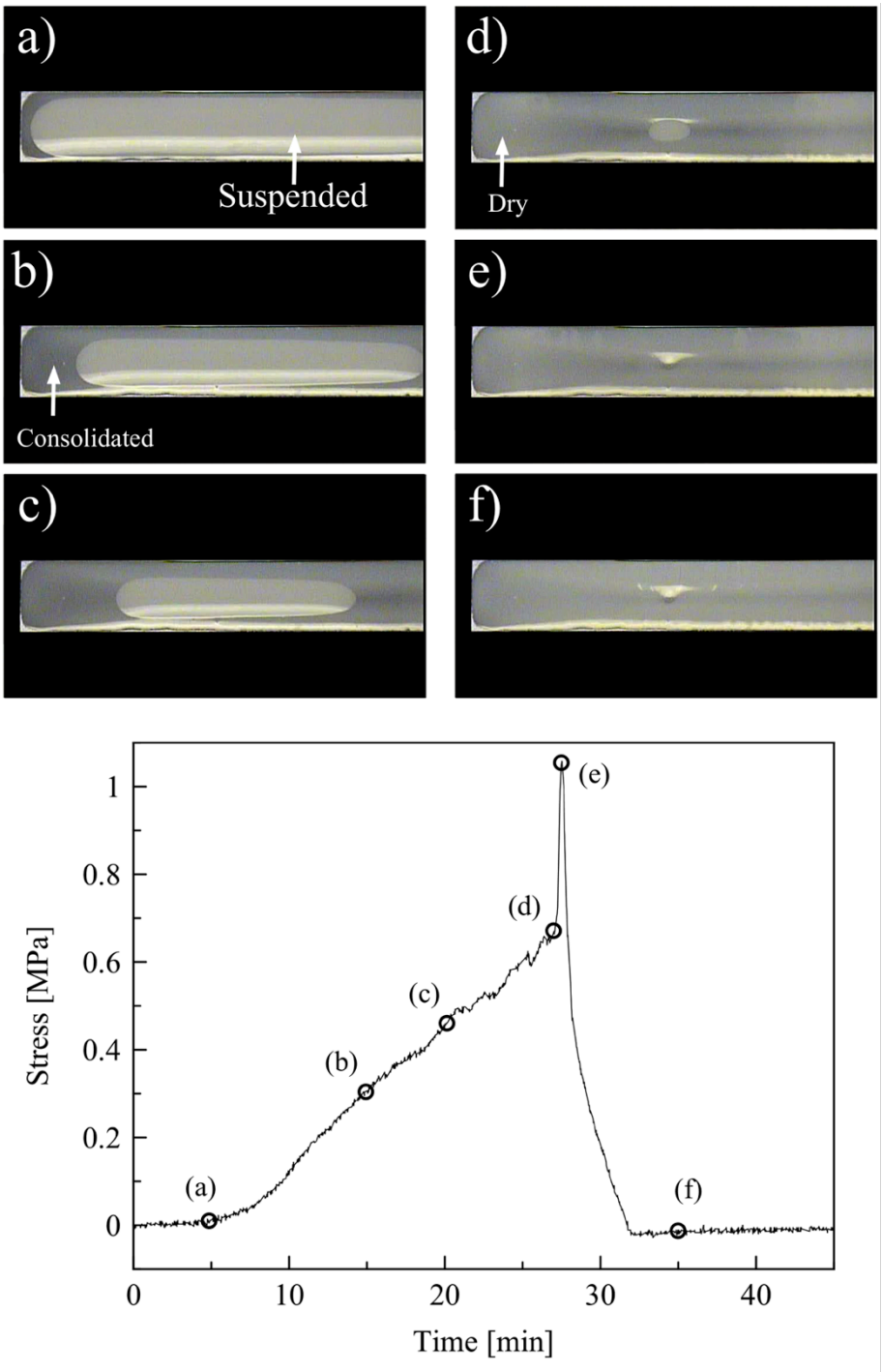

Figure 5.4 Top: Photographs a)-f) show an alumina coating dried on a silicon cantilever without walls after drying for a) 5 minutes, b) 15 minutes, c) 20 minutes, d) 27 minutes, e) 27 minutes 30 seconds, and f) 35 minutes. The black background was added for clarity. Bottom: Stress development curve for the alumina coating, the corresponding images marked on the plot.

Simply based on the appearance of the coating, the stress measurements can be coupled to the presumed microstructure development. Examining the results shown in Figure 5.4, it can be seen that stress development begins once the consolidated region forms. The stress magnitude rises with further drying and the growth of the consolidated region. The sharp rise in stress to the maximum value (around 26 minutes of daring) coincides with the disappearance of the suspended region. At this point, the consolidated region covers a substantial fraction of the cantilever surface. After the peak in stress, the coating begins to dry uniformly from the consolidated region. As the area of the dry region increases, the stress decays rapidly to a negligible value. The drying behavior displayed by the coating dried on a standard cantilever demonstrates a general case of lateral drying, which was described in detail in Chapter 2.

Non-uniform drying, and the microstructure development that accompanies lateral drying, results in stress variations across the cantilever.[57] This non-uniformity complicates the interpretation of stress measurements made using the cantilever beam deflection technique, since this technique yields only an average stress over the entire coating. Using a walled cantilever limit the degree of lateral drying, increases drying uniformity, and directly impacts the stress measured using the cantilever beam deflection method.

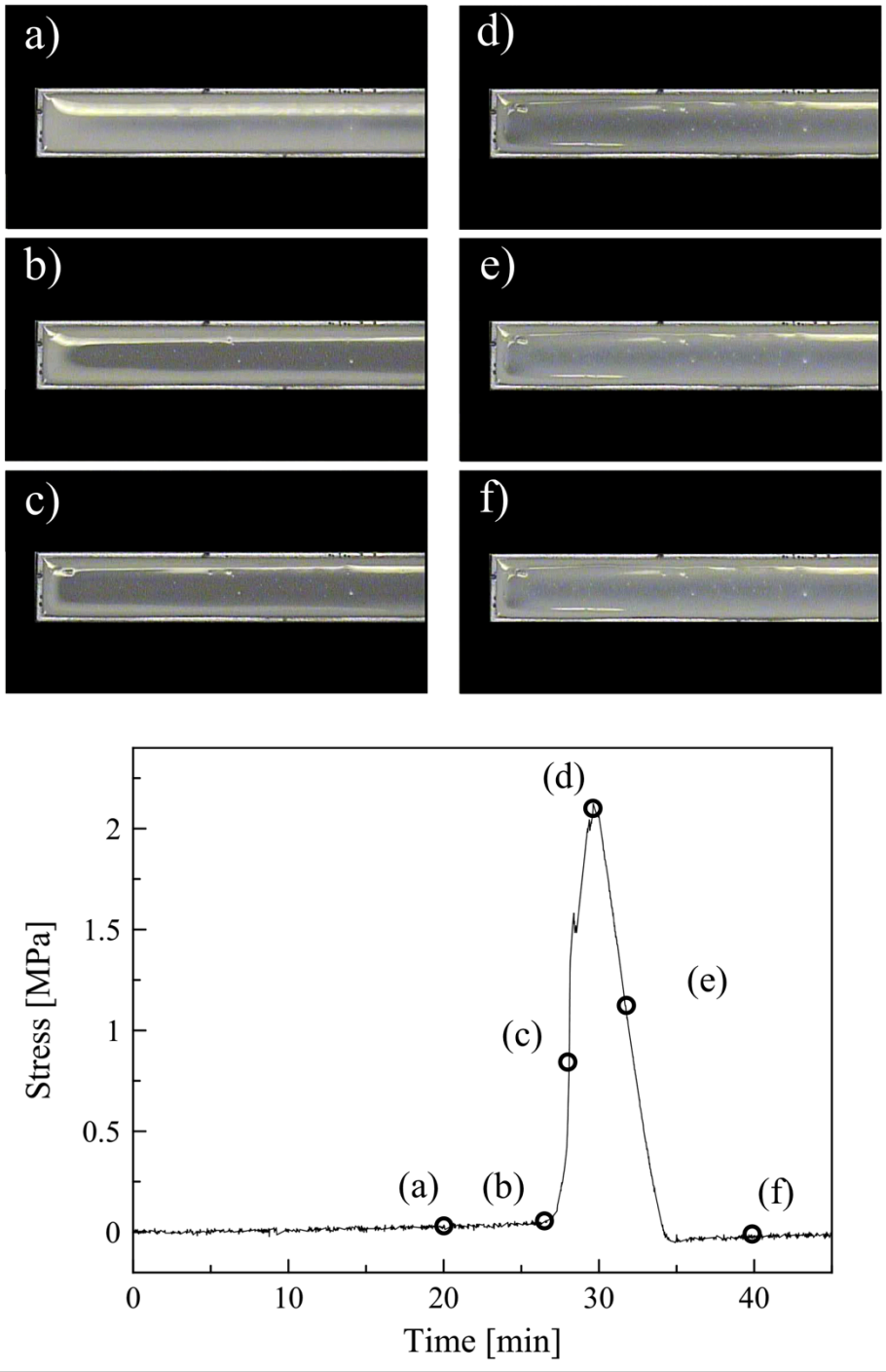

Figure 5.5 Top: Photographs a)-f) show an alumina coating dried on a silicon cantilever with PDMS walls after drying for a) 20 minutes, b) 26 minutes, c) 28 minutes, d) 30 minutes, e) 32 minutes, and f) 40 minutes. The black background was added for clarity. Bottom: Stress development curve for the alumina coating is also shown, the corresponding images marked on the plot.

The photographs in Figure 5.5 show the appearance of an alumina particle coating dried on a silicon cantilever with PDMS walls along the perimeter. Compared to the coating on the standard cantilever, changes in appearance happen more evenly, suggesting that coatings prepared on walled cantilevers dry more uniformly. Similar to the coating on a standard (non-walled) cantilever, changes in the appearance of the coating can be coupled to the stress measurement results, see Figure 5.5. During the early stages of drying, Figures 5.5a and 5.5b, the suspended region covers the entire coated area of the cantilever and there is no significant stress detected in the coating. In Figure 5.5c, a translucent region forms down the center of the cantilever. However, near the wall the coating still as the appearance to be in the suspended state. Like the coatings described in Chapter 4, the thickness of the coating is greatest at the wall due to contact line pinning of the coating liquid. The maximum stress occurs when the consolidated region covers the majority of the cantilever surface, Figure 5.5d. As the coating continues to dry, the measured stress decreases and the coating takes on a more opaque appearance, see Figures 5.5e and 5.5f. A photograph of the cross-section for a fully dry alumina coating on a walled cantilever is shown in Figure 5.6. The non-uniform thickness created by the contact line pinning is highly localized near the wall, while the majority of the coating has a relatively uniform thickness.

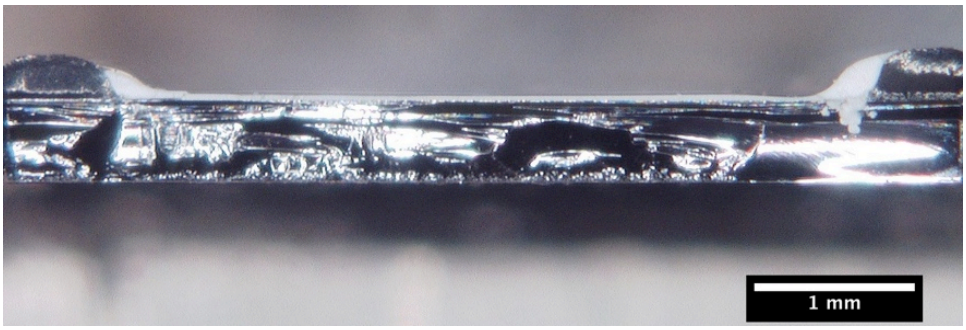

Figure 5.6 Fully dried cross-section of an alumina particle coating dried on a walled cantilever showing localized thickness non-uniformity near the wall.

The stress development curves for the alumina particle coatings prepared on standard and walled cantilevers have noticeable differences, Figures 5.4 and 5.5. For the coating dried on the standard cantilever, stress development begins early during drying and rises gradually before a maximum stress is achieved. For the coating dried on the cantilever with PDMS walls, Figure 5.5, there is an extended stress free period before the stress rises quickly to the maximum value. These differences may be explained considering the development of the coating microstructure and the uniformity in drying.

For both the walled cantilever and the standard cantilever, stress development is related to the formation of the consolidated region. On the standard cantilever, the consolidated region forms early in the drying process and grows inward with time until the suspended region disappears. For the coating dried on the walled cantilever, stress develops once the consolidated region forms, and the stress rises quickly as the consolidated region spreads toward the wall. Comparing the two cases, the fraction of the coating that appears consolidated at the time of the stress maximum is greater for the walled cantilever. Consequently, the maximum stress measured for the coating prepared on a walled cantilever was approximately 2.4 MPa, whereas the maximum stress

measured with the standard cantilever was only 1.1 MPa. Differences in the stress development curves and the measured stresses indicate the importance of uniform drying when measuring stress using the cantilever beam deflection technique.

The influence of lateral drying on the shape of the stress development curve can also be investigated by drying coatings on cantilevers with various widths. Figure 5.7 shows the stress development curves for coatings dried on standard cantilevers and walled cantilevers of various widths. For the standard cantilevers, Figure 5.7a, the lateral drying front must propagate a greater distance on wider cantilevers than on narrower cantilevers. Comparing the two extreme cases, the 5 mm wide cantilever and the 8 mm wide cantilever, there are dramatic differences in the shape of the stress development curves. For both, stress development begins early during drying and builds gradually; however, the gradual increase in stress is accentuated for the 8 mm wide cantilever. For the coatings dried on walled cantilevers, Figure 5.7b, the shape of the stress development curve for the 6 mm wide cantilever is nearly identical to the stress development curve measured for the 8 mm wide cantilever, except for the shift in the stress peak to a longer drying time. Although attempts were made to keep the coating thickness the same between the samples (by changing the volume of suspension deposited), the coating on the 8mm wide cantilever was approximately 23 μm thick compared to a coating thickness of approximately 15 μm on the 6mm wide cantilever. This difference would account for the shift to longer drying times. To further verify this theory, this experiment should be repeated with greater care to ensure that the coating thicknesses are approximately the same.

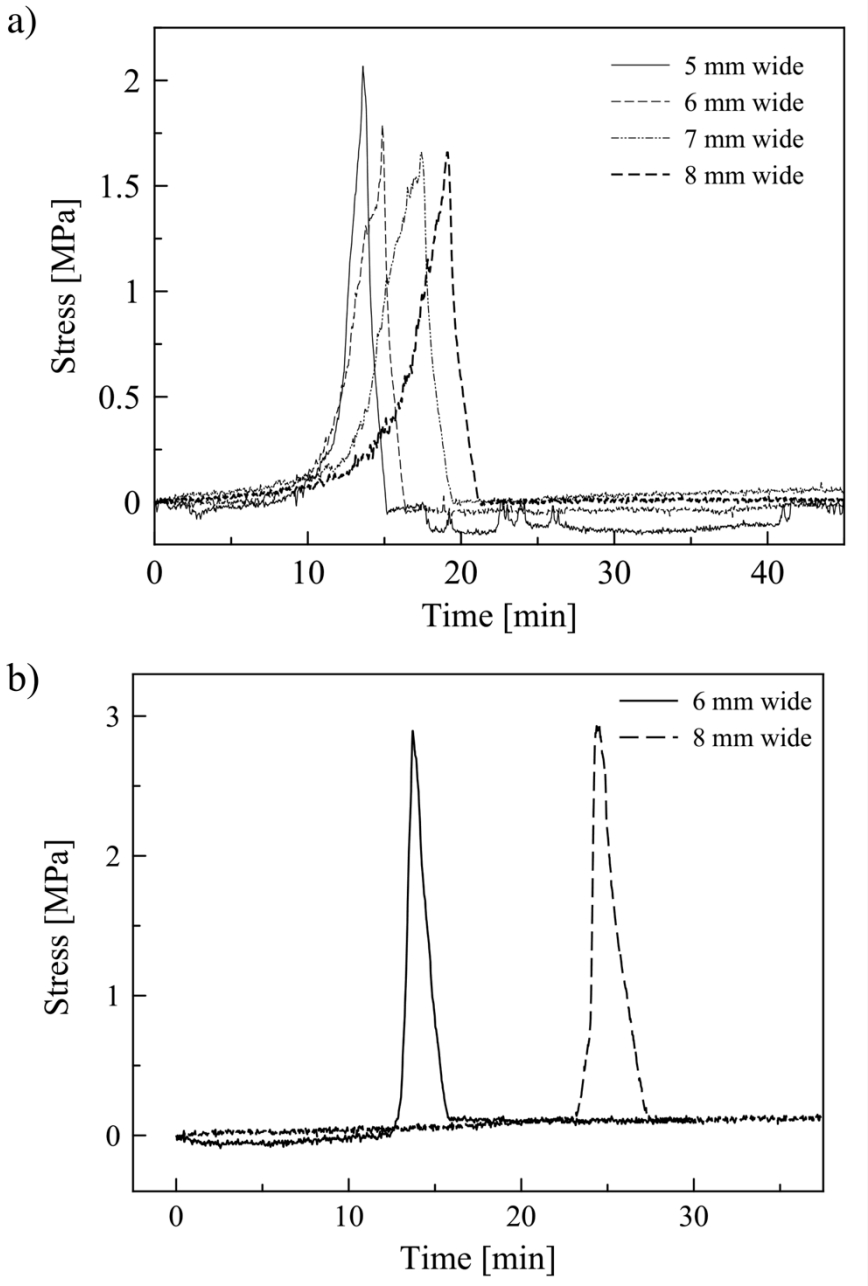

Figure 5.7 a) Stress development curves for alumina particle coatings dried on a) standard cantilevers, and b) walled cantilevers of varying width.

5.3.3 *Microstructure and Stress Development*

Changes in the visual appearance of drying hard particle coatings provide evidence that the coating microstructure is directly related to stress development in the film. However, finding these connections between stress measurements and visual observations is complicated when the microstructure development occurs non-uniformly. The drying uniformity achievable for coatings prepared on walled cantilevers allows direct correlations between the measured stress development in the coating and the development of the microstructure. However, the visual appearance can only provide clues about the developing microstructure in the coating microstructure. Direct high-resolution images of the wet coating microstructure were obtained using a cryoSEM time-sectioning technique. The cryoSEM samples were prepared by freezing samples at various extents of drying, fracturing to expose the cross-section, and imaging the frozen cross-section with an SEM equipped with a sample stage cooled with liquid nitrogen. Using this technique, high-resolution snapshots of the coating microstructure can be used to map stress development in the film to the true conditions of the coating microstructure.

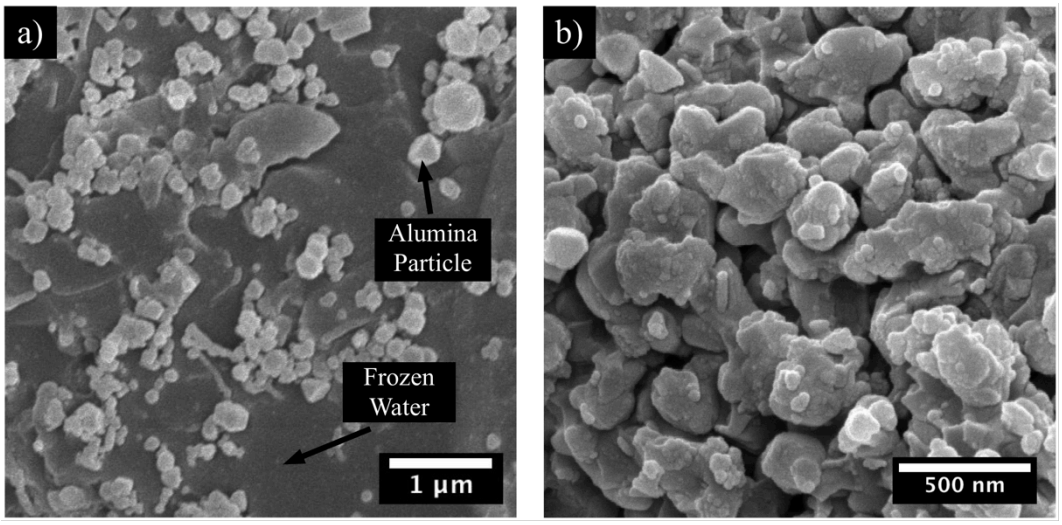

Figure 5.8 CryoSEM cross-sectional micrographs of alumina particle coatings dried on walled cantilevers for a) 7 minutes and b) 30 minutes.

CryoSEM cross-sections for alumina particle coatings frozen during the drying process are shown in Figure 5.8. Figure 5.8a shows the microstructure after 7 minutes of drying; the alumina particles appear to be fully suspended in the frozen water matrix. At this stage of drying, no stress has developed in the coating. Figure 5.8b shows a portion of a frozen cross-section of an alumina coating dried for 30 minutes, just after the peak in stress. From the microstructure shown in Figure 5.8b, it is clear that the alumina particles have formed a consolidated network and that the coating is no longer in the fully saturated state. This is predictable because the peak in stress should correspond to the fully saturated condition. However, discerning the alumina particles from the frozen water is difficult, especially for the later stages of drying. The non-uniform granular particles the broad particle size distribution makes interpretation of the cryoSEM images challenging. Additionally, the smallest alumina particles in the commercial powder are

comparable in size to frost contamination, an artifact of sample preparation. These artifacts were discussed in greater detail in Chapter 3.

To further investigate the relationships between the development of the coating microstructure during drying and stress development using cryoSEM, regularly shaped silica particle coatings were chosen for their monodispersity and larger size (d = 1 μm). The photographs in Figure 5.9 show the changes in appearance for a silica particle coating prepared on a walled cantilever. Similar to the alumina coatings, changes in the visual appearance of the silica coating correlate to the stress development curve, Figure 5.9. After depositing the silica suspension, the appearance of the coating is similar to that of the original dispersion, Figure 5.9a. At this stage of drying, no appreciable stress has developed in the coating. After drying for approximately 15 minutes, the coating takes on a more translucent appearance, Figure 5.9b, which is concurrent with the sharp rise in measured stress in the coating. Like the alumina particle coatings, the translucent appearance is presumed to be associated with the particles forming a consolidated network saturated with water. With further drying, Figures 5.9c-f, the appearance of the coating becomes more opaque and the measured stress decreases. For the silica particle coatings, the cryoSEM time-sectioning technique was again used to further investigate the relationships between stress development and the developing microstructure.

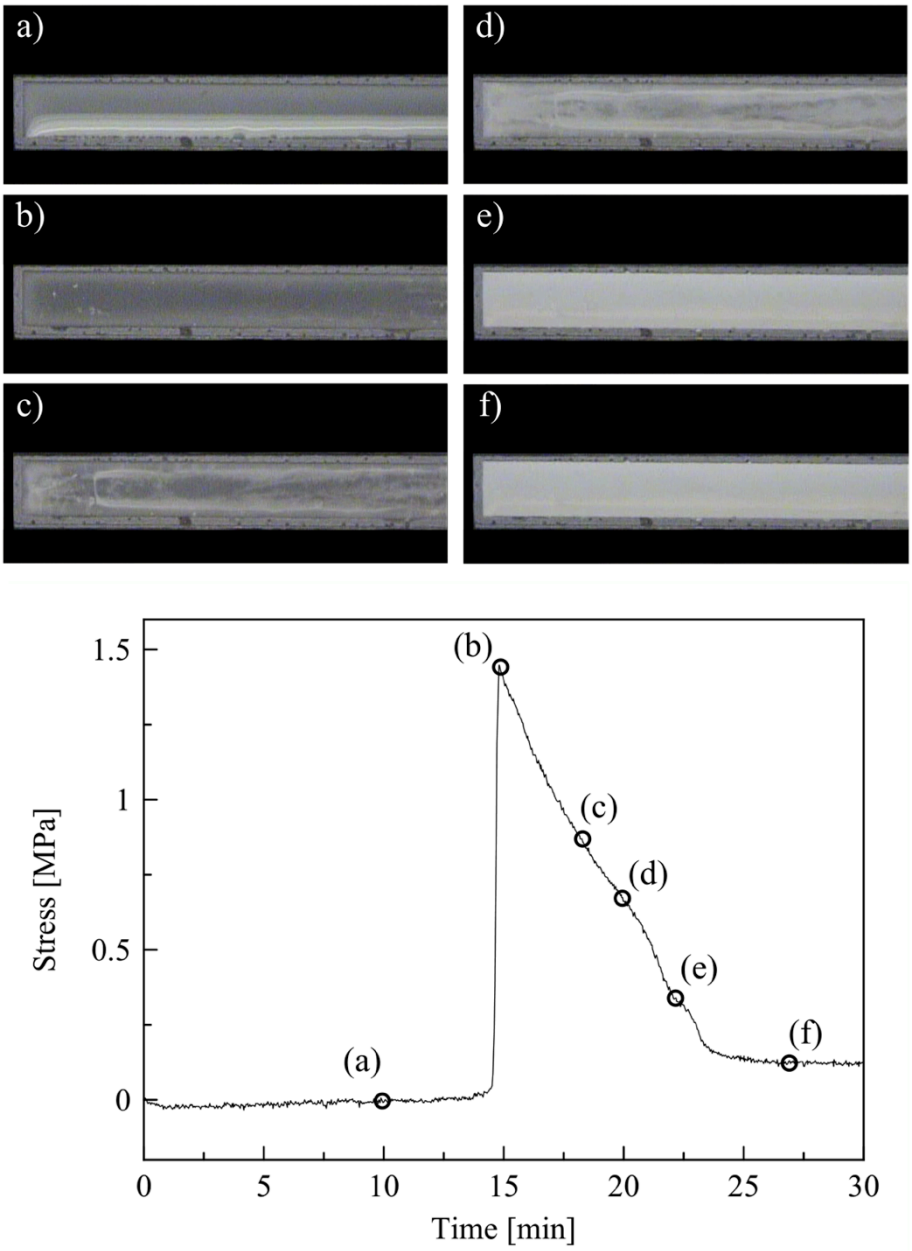

Figure 5.9 Top: Photographs a)-f) show a silica coating dried on a silicon cantilever with PDMS walls after drying for a) 10 minutes, b) 15 minutes, c) 18 minutes, d) 20 minutes, e) 22 minutes, and f) 27 minutes. The black background was added for clarity. Bottom: Stress development curve for the alumina coating is also shown, the corresponding images marked on the plot.

A cryoSEM cross-section for the coating frozen after approximately one minute of drying is shown in Figure 5.10. In the cryoSEM images, some of the silica particles are embedded in the frozen cross-section, while others were removed during the fracture process. If the particles were removed during fracture, crater-like structures on the fracture surface mark the location where a particle was present. The cryoSEM image in Figure 5.10a clearly shows the distribution of particles in the coating near the free surface; the substrate is not visible here. Along the free surface, particle accumulation is evident, Fig 5.10b, which is expected because for this system the dimensionless Peclet number is greater than one, see Chapter 2.[15,21] Additionally, Figure 5.10b shows that although particle accumulation has begun, the liquid air interface remains flat, and particles remain below the free surface. Under the consolidated particle layer at the free surface, Fig 5.10c, the silica particles in the coating appear to be uniformly distributed and fully surrounded by the frozen water. The stress development curve, Figure 5.9, shows that early in the drying process there is negligible stress.

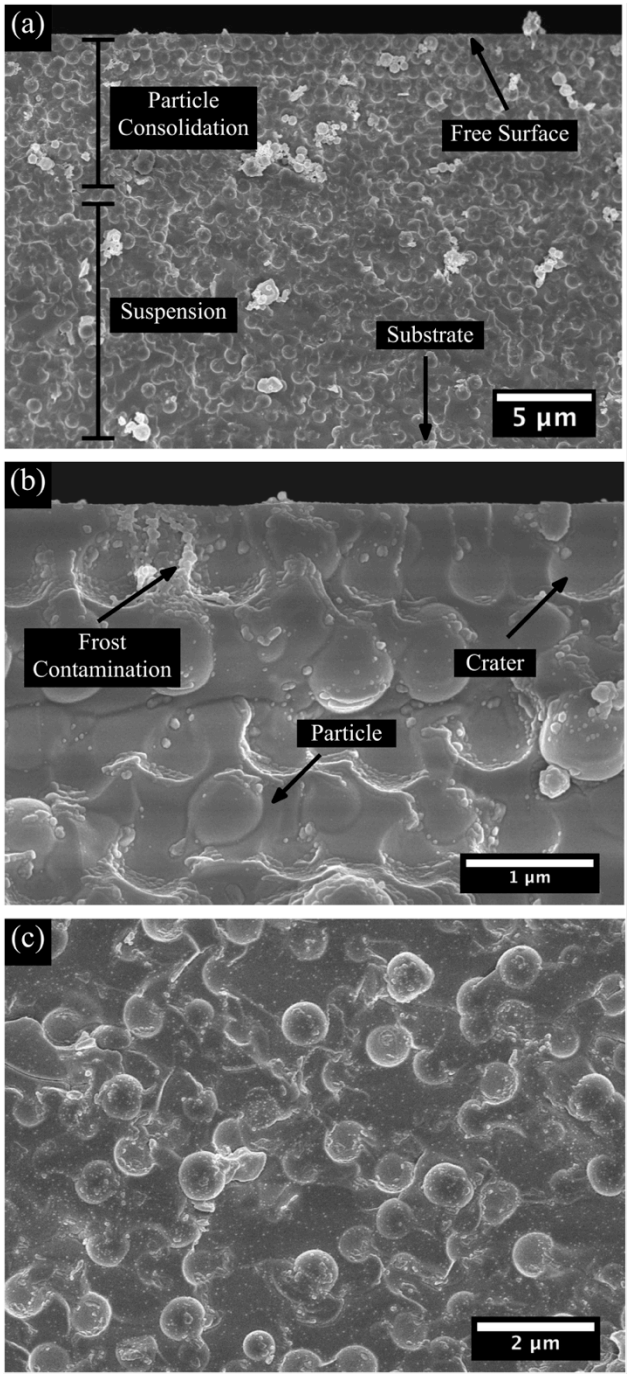

Figure 5.10 CryoSEM cross-sectional images for a silica particle coating dried for 1-minute. a) Low magnification view of the cross-section showing particle distribution in the film. b) Particle consolidation along the free surface. c) Uniform particle distribution below the consolidated region.

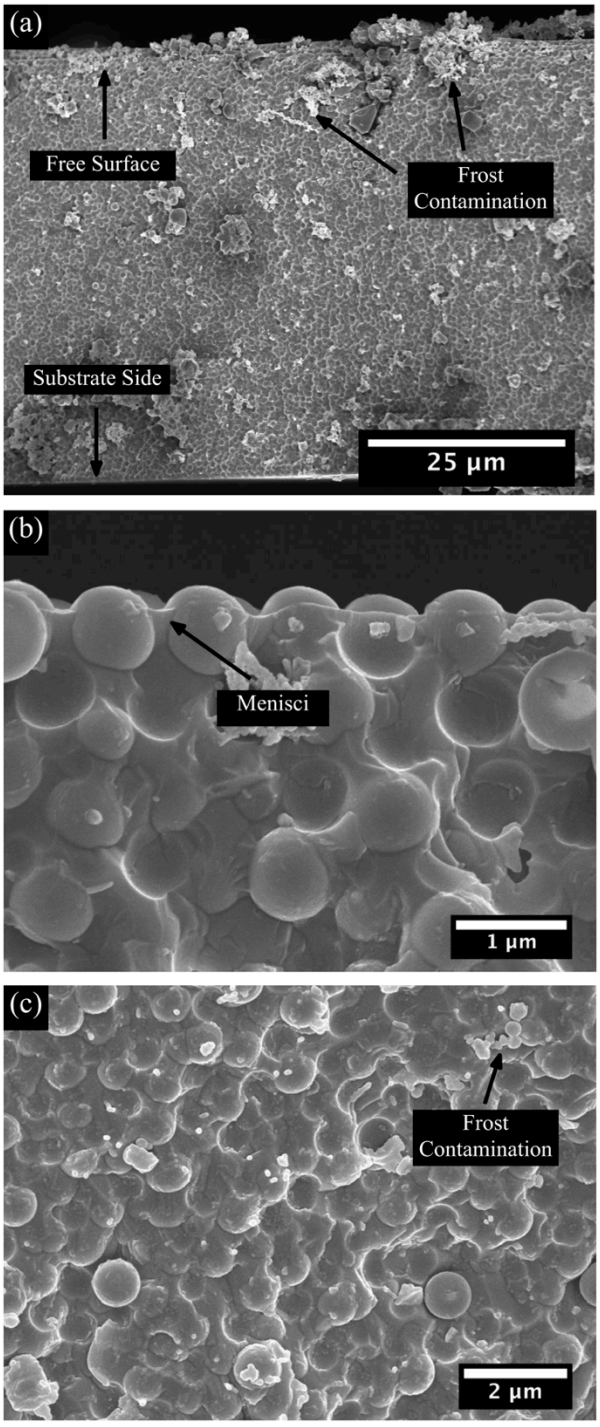

Figure 5.11 CryoSEM cross-sectional images for a silica particle coating dried for 14 minutes. a) Low magnification view of the cross-section showing uniform saturation throughout the coating thickness. b) Curved menisci formed between adjacent particles along the free surface c) Uniform saturation in the consolidated particle packing below the free surface.

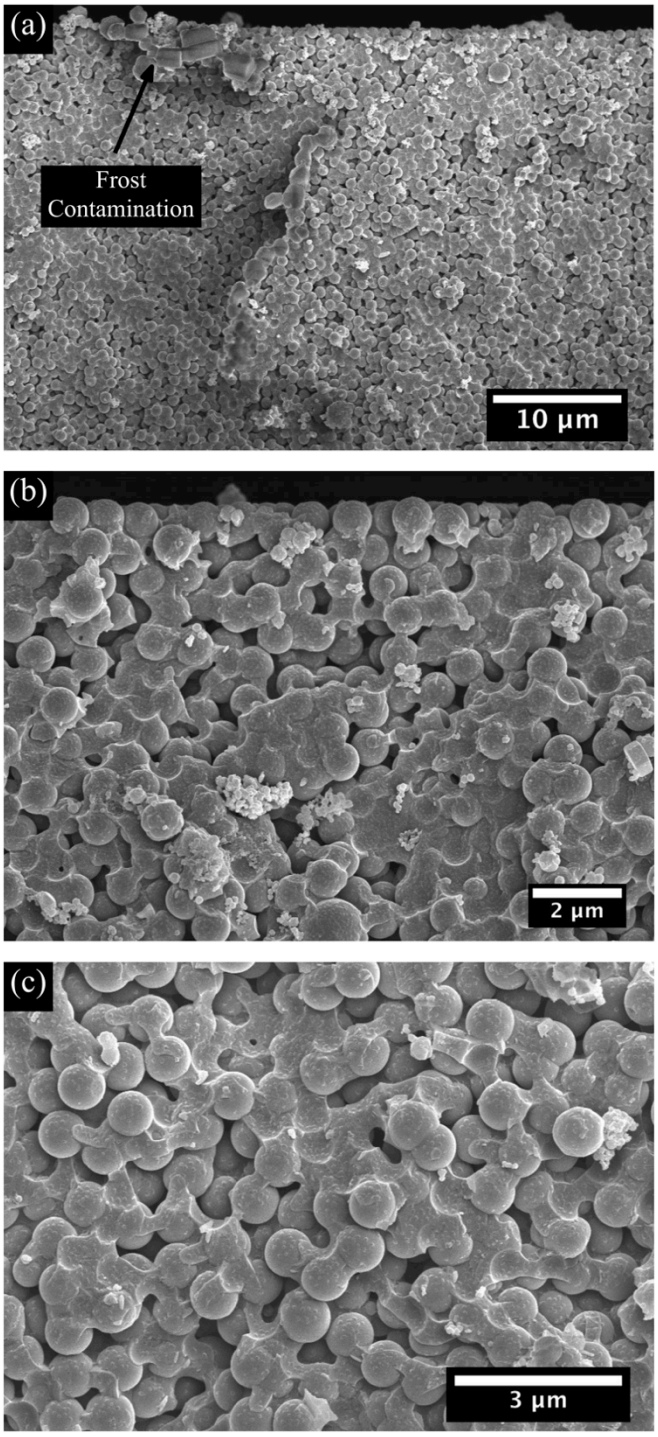

Figure 5.12 CryoSEM cross-sectional images for a silica particle coating dried for 17 minutes. a) Low magnification view of the cross-section showing fingers of air penetrating throughout the coating thickness. b) Air invasion in the particle packing near the free surface c) Air invasion in the particle packing halfway through the coating thickness

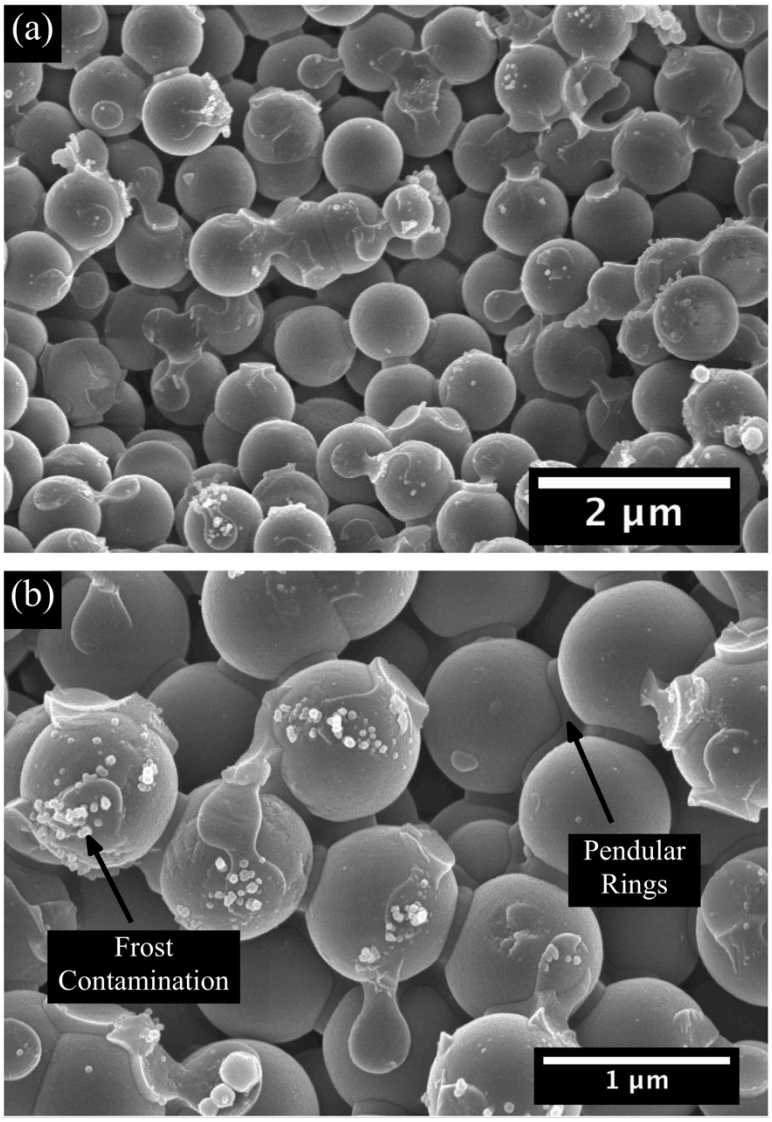

Figure 5.13 CryoSEM cross-sectional images for a silica particle coating dried for 20 minutes. a) Low magnification view of the cross-section showing the distribution of pendular rings of water in the particle packing b) high magnification image of the pendular rings formed between adjacent silica particles.

Figure 5.11 shows cryoSEM images for a silica particle coating dried for 14 minutes. From Figure 5.11a, it appears that the particles are closely packed and the porespace is fully saturated throughout the coating thickness. A closer look at the free surface, Figure 5.11b, reveals that curved menisci have developed between adjacent particles. At this extent of drying, no air invasion was evident from the cryoSEM images. A higher magnification image of the microstructure near the center of the coating, Fig 5.11c, reveals the saturated packed particle network. The images shown in Figure 5.11 represents the condition of the microstructure when the measured stress is at, or nearing, the maximum value, Figure 5.9. Frost contamination, an artifact of sample preparation, is visible in the cryoSEM cross-sections. Several of these artifacts are noted in Figure 5.11; however, many other instances of frost contamination are visible in the cryoSEM images.

A cryoSEM cross-section for a coating dried for 17 minutes is shown in Figure 5.12. Here, the coating has begun to dry and the pores have begun to empty. From the cryoSEM images, air invasion into the particle packing is present from the free surface to the substrate, see Figure 5.12a. Higher magnification images of the microstructure, Figures 5.12b and 5.12c, show that the larger pores have begun to empty while the smaller pores remain filled with frozen water. At this stage in drying, stress measurement, Figure 5.9, reveals that the stress in the coating has begun to decay from the maximum value.

As the coating continues to dry, the remaining water in the coating exists as pendular rings bridging adjacent particles. Figure 5.13 shows cryoSEM cross-sections of the coating microstructure showing the pendular rings of water between the particles.

The measured stress in the coating, Figure 5.9, shows that the stress in the coating continues to decay. Eventually the stress in the coating reaches some residual value. Pendular rings of water between spherical particles has also imaged with environmental SEM;[27] the authors also simultaneously measured stress development for a 2D layer of spherical particles has a function of the relative humidity (i.e. size of the pendular rings). They found that stress increases as the relative humidity was lowered from 100% to 70%. As the relative humidity was lowered further, the stress in the film plateaued until the relative humidity is reduced below approximately 20% where they found a sharp rise in stress at low relative humidity. The residual stress for the silica particle coatings used in this study was not dependent on the relative humidity; however the relative humidity during the experiments was only varied between 20%-60%.

Combining stress measurement and cryoSEM is a powerful technique for investigating the relationships between stress and microstructure. For the silica particle coatings characterized in this section, the results indicate that stress development is related to the degree of saturation in the coating and the capillary pressure in the liquid. Next, the origins of stress development in hard particle coatings will be discussed in light of the results presented here.

5.3.4 *Origins of Stress Development*

Previous investigations of stress development in ceramic particle coatings suggest a capillary origin of stress development and the provide connections between stress development and the degree of saturation.[43,58,98,99] However, the non-uniform microstructure development that occurs during lateral drying complicates the

interpretation of stress measurements. Stress measurement and cryoSEM results indicate that stress develops once the consolidated particle network forms. The results presented here advance the understanding of stress development by providing direct connections between stress development and the wet coating microstructure. The typical stress development profile for a ceramic particle coating includes an initial stress-free period, a period of stress rise, and a period of stress decay.

Immediately after deposition, the coating is a fluid suspension of fully suspended particles. As evaporation begins, volume loss due to evaporation is accompanied by flow of the liquid coating suspension. Therefore, stress development is negligible until a critical volume fraction of particles is achieved and the particles form a saturated consolidated network. For coatings that exhibit non-uniform drying, this condition may be achieved first near the edges as a packing front forms (see Figure 3). For coatings prepared on walled cantilevers, particle consolidation is achieved more uniformly across the substrate, except near the wall where the coating is thicker due to contact line pinning.

Once the particles form a consolidated network, further drying is accompanied by stress development in the coating. As water evaporates from the particle network, menisci form between the particles along the free surface, and a capillary pressure is generated in the liquid that compresses the particle network. Since the coating is adhered to the substrate, in-plane shrinkage of the coating is constrained and a bi-axial tensile stress develops. The results presented in this work demonstrate the importance of drying

uniformity on the shape of the stress development curve measured using the cantilever deflection technique.

Compared to coatings dried on standard cantilevers, the coatings prepared on walled cantilevers dry more uniformly and show a much steeper rise in stress. The gradual rise in stress shown for the alumina coating dried on a standard cantilever (Fig. 4), is related to the non-uniform extents of drying and microstructure development across the substrate. The dramatic rise in stress seen for the silica coating (Fig. 8), is connected to the extremely uniform drying condition. The sharp rise indicates that the coating transitions from a stress-free, fluid dispersion to a saturated packed particle network that supports a stress uniformly over the substrate after a certain amount of drying. The gradual rise in stress shown for coatings that undergo lateral drying is directed related to the non-uniform extents of drying across the substrate.

The size of the pores in the network dictates the maximum curvature of the menisci and the maximum capillary pressures achievable in the liquid.[26] Decreasing the particle size results in smaller pores and higher capillary pressures. The maximum stress measured for silica particle coatings (prepared on walled cantilevers) made from 0.5 μm, 1.01 μm, 1.57 μm particles were 1.4 ± .3 MPa, 1.1 ± .2 MPa and 0.7 ± .1 MPa, respectively. As expected, coatings made with smaller particles achieve higher coating stress during drying. This trend is consistent with results reported by others for alumina particle coatings.[43]

Eventually, the pores begin to empty, and the liquid-air interface moves into the coating. As air invades the particle network, the volume fraction of the coating under the

capillary pressure decreases, and the period of stress decay begins. For the silica particle coatings prepared on walled cantilevers, cryoSEM reveals that fingers of air extend throughout the coating thickness (see Figure 8c). The monodisperse silica particles do not form a closely packed network; hence there is an apparent distribution of pore sizes. The larger pores empty preferentially while water remains where the pore size is smaller.

The decay in stress occurs as water is removed from the particle network. For the alumina particle coatings, stress decays more quickly than for the silica particle coatings. This difference is likely a result of different pore structures in the particle networks. The pore structures are shown in the cryoSEM images shown in Figures 6b and 8c. For the alumina coating, the small, irregularly shaped particles and broad particle size distribution likely results in a narrow distribution of pore sizes in the coating. For the silica particle coating, the large spherical particles result in particle network with larger pores and apparently a broader distribution of pore sizes. With further drying, the remaining water in the coating exists as pendular rings between adjacent particles. The capillary pressure in the pendular rings holds the particle network together as stress decays with further drying. The decay in stress occurs gradually as the remaining water evaporates from the film.

The results shown here indicate that stress development in hard particle coatings depends on the microstructure and state of saturation of the coating. Stress measurements (made using walled cantilevers) and cryoSEM characterization clearly demonstrate the relationship between structure and stress development. The connections made here illustrate the importance of limiting lateral drying and promoting uniform microstructure

development during stress measurements. Non-uniform microstructure development during drying affects both the shape of the stress development curve and the magnitude of the measured stress. CryoSEM is a powerful tool that provides unique insights into the mechanism of stress development; however, cryoSEM characterization can be difficult for some coatings systems. The combination of uniform drying, stress measurement, and microstructure characterization make it possible to investigate the fundamentals of stress development and should advance the knowledge on how stress development leads to stress induced defects, like cracking.

5.4 *Summary*

This Chapter demonstrates the influence of a lateral drying front on stress development measured using the cantilever beam deflection technique. The use of cantilevers with PDMS walls suppresses lateral drying and increases drying uniformity. The uniformity achieved with the walled cantilever makes it possible to correlate stress measurement to the coating microstructure. CryoSEM was used to image the development of the coating microstructure during drying. The combination of stress measurement and cryoSEM revealed that the stress development was directly related to the state of saturation in the coating. The combination of uniform drying, stress measurement, and microstructure characterization make it possible to investigate the fundamentals of stress development and advances the knowledge on how stress development leads to stress induced defects, like cracking.

Chapter 6

STRESS DEVELOPMENT IN LATEX PARTICLE COATINGS

6.1 *Background and Motivation*

Latex coatings are found in a wide array of industrial applications including architectural coatings (paints, floor coatings, roof coatings, etc.), adhesives, and paper coatings. Latex particles are also frequently used as binders in hard particle coatings to suppress cracking and to increase mechanical integrity of the film. A latex, is a suspension of polymer particles synthesized through emulsion polymerization.[109] Waterborne latex coatings can be made relatively cheaply as the emulsion polymerization process does not require the use of expensive (volatile) solvents and high molecular weight particles can be achieved quickly due to rapid polymerization rates.[1] Another advantage to latex coatings is that the viscosity of the dispersion is independent of the molecular weight of the particles.

The process of latex film formation was discussed in Chapter 2; however, a brief discussion is provided here. Latex film formation is commonly divided into three stages: consolidation, compaction, and coalescence.[1,2,29,30] During consolidation, water evaporates from the film at a relatively constant rate until the latex particles reach consolidation. During compaction, the evaporation rate of water slows, as particles begin

to deform, eliminating the void space in the particle network. The forces responsible for particle deformation during film formation have been widely contested and are described in Chapter 2. In this chapter, a capillary mode of particle deformation is assumed. This mode of deformation was first proposed by Brown[18] and was discussed in great detail by Pekurovsky and Scriven.[28]

Regardless of the deformation model that is assumed, most theories conclude that film formation is only possible when the latex particles are sufficiently soft (i.e. particle $T_g < T_{drying}$). This is confirmed by the existence of a minimum film formation temperature (MFFT), defined as the lowest temperature at which a latex coating will dry to form a clear, continuous, crack free film. The MFFT usually lies close to, but is not necessarily identical to, the glass transition temperature (T_g) of the latex particle. Therefore, the T_g of the latex strongly influences the film formation behavior.

Most latex coatings are water-based suspensions; however, the aqueous phase usually contains additives that include: coalescing aids, biocides, defoamers, pH modifiers, and viscosity modifiers. Many of these additives are volatile organic compounds (VOCs), that, when emitted to the environment, can undergo photochemical reactions that produce oxidants that are damaging to the atomosphere.[109] Conventional (volatile) coalescing aids are used to soften or plasticize the polymer particles by lowering the glass transition temperature of the particles, which allows higher T_g particles to undergo film formation at room temperature. A common example of a coalescing aid that is frequently used for architectural paints is 2,2,4-trimethyl-1,3-pentanediol monoisobutyrate (TPM, sold under the trade name of Texanol™). During film formation,

the coalescing aid leaves the film by evaporation and the polymer regains its original T_g and the resulting mechanical properties of the high T_g polymer. Government agencies, such as the US Environmental Protection Agency (EPA), place restrictions on the amounts of VOCs that are allowed in latex coatings. Therefore, it is important to understand how water-based latexes undergo film formation both with and without the use of these additives.

During film formation, stress develops due to constrained shrinkage of the coating imposed by the substrate. The stresses that develop in the film during drying can lead to particle deformation and compaction of the latex particles. Additionally, stress development in the coating may lead to the formation of coating defects such as cracking. Perera and Van den Enyde[110] were the first to study stress development in latex based paints. In other studies, the affects of pigment particles[111] and coalescing aids[112] were also investigated in relation to the stress evolution in the coating. When no coalescing aid was present, the stress increased with drying time until a maximum value was achieved. This was followed by a slight decay in stress from the maximum value. For paint formulations that contained a coalescing aid, a variety of behaviors were observed after the maximum stress was achieved. Perera et al[110] describe stress development in latex coatings as a competition between two opposing processes; one leading to a stress increase due to constrained volume shrinkage of the coating (due to coalescence and loss of volatiles), and one resulting in stress relaxation due to the viscoelastic behavior of the polymers.

More recently, Martinez and Lewis[62] studied the stress development in latex-only coatings as a function of particle T_g. They investigated three latex particles; a low T_g, mid T_g, and high T_g (T_g = -40°C, -6°C, and 19°C, respectively). They found that the maximum stress in the coating increased only slightly as the particle T_g increased. The stress evolution in the films also varied. For the low T_g coating, stress developed gradually over time and there was no apparent 'peak' in stress. For the mid T_g coating, the stress rose more quickly to its maximum value and plateaued for the duration of the experiment. In the high T_g coating, the stress rose to the maximum value (in a similar fashion as the mid T_g latex), which was followed by a slight decay in stress to the residual value. Yow et al.[97] observed a similar dependence on the evolution of stress as a function of the latex MFFT.

Tirumkudulu and Russel[61] studied the role of capillary pressure on the film formation behavior of latex coatings with various particle sizes and glass transition temperatures for various film thicknesses. They found that, regardless of the particle size or particle T_g, thicker films have lower stress magnitudes than thinner films. They subsequently propose a correlation between the crack spacing in the film and the film thickness.[95] The crack spacing was found to be linearly related to film thickness, with greater distances between cracks for thicker films, and not dependent on particle size. Yow et al.[96] confirmed this trend experimentally and confirmed that crack spacing was dependent on coating thickness and independent of latex particle size.

Past studies on stress development in latex coatings have used cantilever deflection techniques. However, latex coatings often dry laterally, which complicates the

interpretation of stress measurement results obtained using this technique. The cantilever deflection technique is not capable of detecting variations in stress across the substrate, and can only yield an average stress in the coating. In this work, stress development was investigated using walled cantilevers, which increase drying uniformity and suppress lateral drying. The use of walled cantilevers and the influence of lateral drying fronts on stress measurement in hard (ceramic) particle coatings was discussed in Chapter 5.

Here, the stress evolution for acrylic latex particles was investigated without complications from lateral drying. The variables explored in this study include the particle T_g, addition of various coalescing aids (conventional, low-VOC), and concentration of the coalescing aid. Results from this work provide insights into the general process of stress development for industrially relevant latex coatings plasticized with a variety of widely used coalescing aids. Additionally, the stress development and film formation behavior of PVDF:acrylic blends was investigated.

6.2 *Materials and Methods*

6.2.1 *Acrylic Latex*

The monodisperse acrylic latexes used in these studies were provided by Dr. Wenjun Wu with Arkema Coating Resins (Cary, NC). The latex particles were synthesized from three common acrylic monomers: butyl acrylate (BA), methyl methacrylate (MMA), and methacrylic acid (MAA). The target T_g was calculated using the Fox equation:[113]

$$\frac{1}{T_g} = \frac{w_1}{T_{g,1}} + \frac{w_2}{T_{g,2}} + \cdots \tag{6.1}$$

where w, represents the weight fraction of the polymer. The T_g of the polymer can be controlled by adjusting the ratio of the monomers present during polymerization. The small amount of acrylic acid is added to provide colloidal stability. Characteristics of the latex samples used in this study are compiled in Table 6.1. The T_g values reported in this paper were obtained from the initial ramp for fast-heat DSC experiments. The MFFT was measured on a rectangular temperature gradient bar, and was identified as the lowest temperature where the latex formed a clear crack-free film,. The volume-averaged (D_v) and number-averaged (D_n) particle sizes were measured using Nanotrac 150 (Microtrac) particle size analyzer.

Table 6.1 Sample Characteristics for Acrylic Latexes

Sample ID	Composition	Fox T_g (Estimated)	MFFT [°C]	Particle Size D_v [nm]	Particle Size D_n [nm]
MBA 1	23.5BA/75.0MMA/1.5MAA	50°C	> 60°C	182	156
MBA 43	46.1BA/52.4MMA/1.5MAA	10.6°C	18°C	177	154
MBA 31	53.3BA/43.2MMA/1.5MAA	0°C	5.2°C	169	150

6.2.2 *PVDF:Acrylic Latex*

The PVDF:acrylic latex blends used in this study were provided by Dr. Kurt Wood with Arkema Fluoropolymers (King of Prussia, PA). The latex particles are composed of poly(vinylidene fluoride) (PVDF) and an acrylic copolymer. PVDF is a semi-crystalline polymer with a T_g = -20°C and a melting temperature (T_m) of 155°C. The acrylic copolymer is a mix of poly(methyl methacrylate) and poly(butyl acrylate) with a

T_g = 50-60°C. These samples are latex-only samples containing no additives (coalescing aids, pigments, etc.). Two PVDF:acrylic blends were studied, a 50:50 blend and a 70:30 blend. A small two-seeded polymerization allows for an intimately blended morphology of PVDF and acrylic polymer within each particle. Nuclear magnetic resonance (NMR) and differential scanning calorimetry (DSC) data collected at Arkema show that the PVDF has approximately 8-10% residual crystallinity.

Table 6.2 Properties of PVDF:Acrylic Blends

Sample ID	Composition	MFFT [°C]	Particle Size [nm]	Total Solids [%]
70:30	70 PVDF/30 Acrylic	26-28°C	150-200	40
50:50	50 PVDF/50 Acrylic	12°C	150-200	40

6.2.3 *Stress Measurement*

Stress development was monitored *in-situ* with the cantilever deflection technique using modified walled cantilevers. The stress measurement apparatus was described in detail in Chapter 3, a schematic diagram of the apparatus is shown in Figure 3.2. To fabricate the walled cantilevers, PDMS (Sylgard® 184, Dow Corning) walls were molded onto silicon cantilevers (6 mm x 60 mm) that were cut from (100) silicon wafers, see Fig 5.2a. The Young's modulus and Poisson's ratio of the cantilevers were taken to be E = 169 GPa, ν = 0.064, repectively.[106] To calculate the stress development from the deflection of the walled cantilever, Eq. 5.2 is applied with the corresponding correction factor.

The details of the stress measurement apparatus and measurement procedure are provided in Chapter 3. During the experiment, 40 μL of the latex suspension was applied to the walled cantilever using a micropipette. The relative humidity and temperature maintained at 21°C ± 1°C, and 40%RH ± 2% during the experiments. A video camera positioned above the experimental apparatus records the appearance of the cantilever during the stress measurement. Following the experiment, the dried coating thickness as measured with a micrometer.

6.2.4 *Minimum Film Formation Temperature (MFFT) Measurement*

For these studies the MFFT was investigated for latex particle coatings on an MFFT90 (Rhopoint) shown in Figure 3.1. The latex suspension was coated onto a PET substrate, which covers a rectangular metal bar over which a temperature gradient exists. The experimental details of the MFFT measurement were discussed in Chapter 3. In this study, the MFFT is defined as the cloudy-clear transition.

6.3 ***Results and Discussion***

6.3.1 *Acrylic Latexes*

First, the stress evolution of latex coatings (with various MFFTs) was investigated using the cantilever deflection technique with walled cantilevers. The characteristics of the latex samples used in this work are compiled in Table 6.1. The MFFT of a latex depends on many variables including the polymer composition, particle size, particle T_g, and plasticizer content (coalescing aid).[109] When a latex coating is dried below the MFFT, the dried film is opaque and often cracked. Below the MFFT, the latex particles

are harder and do not undergo extensive particle deformation upon drying. In this case, the extent of particle deformation is not sufficient to close the void spaces in the particle network. Light scattering from these voids (which are filled with air) give the coating an opaque appearance. Likewise, cracks form because the mechanical strength of the particle-particle contacts are weak due to limited polymer diffusion across particle boundaries when $T_{exp} < T_g$. When the cohesive strength of the particle network is low, it takes minimal strain energy to initiate crack formation.

Latex coatings dried above the MFFT have a transparent, clear appearance and are crack free. Above the MFFT, $T_{exp} > T_g$, the particles are softer and capable of deforming to close the void space in the particle packing, reducing the amount of light scattering from the film. A clear, transparent appearance of the coating does not guarantee that the dried coating is void free, only that the sizes of the voids are smaller than the wavelength of light.[114] Similarly, above the MFFT, polymer diffusion across particle boundaries is more complete and the film can develop sufficient cohesive strength to resist the crack formation.

Stress development in latex particles coatings occurs due to constrained volume shrinkage in-plane of the substrate. When the particle network reaches consolidation, the particle volume fraction may range from $\phi = 0.6 - 0.74$. With further drying, the particles deform, and the particle volume fraction approaches unity. This process requires a volumetric shrinkage of the coating; however, the coating is adhered to the rigid substrate. The constrained shrinkage of the coating in-the-plane of the substrate gives rise to the development of a tensile stress in the film that can be characterized using stress

measurement techniques. Figure 6.1 shows the stress measurement results for latex coatings with various MFFTs dried at room temperature.

Sample MBA1 has an MFFT much greater than room temperature, and therefore does not undergo film formation, and cracks upon drying. The stress development curve, Figure 6.1, shows an initial stress-free period, followed by a sharp increase in stress. The stress plateaus briefly (several small increases and decreases) before rising to the maximum stress. A video recording of the cantilever during the measurement reveals that throughout the plateau period, several small cracks develop near the wall and the coating begins delaminating from the wall (forms a surface crack). Delamination occurs preferentially at the wall because the coating does not adhere well due to the low surface energy of PDMS. Cracking and delamination relieve stress; however, stress is still increasing over the rest of the cantilever. When the stress reaches the maximum value, many cracks begin to form and the stress decays rapidly in the film.

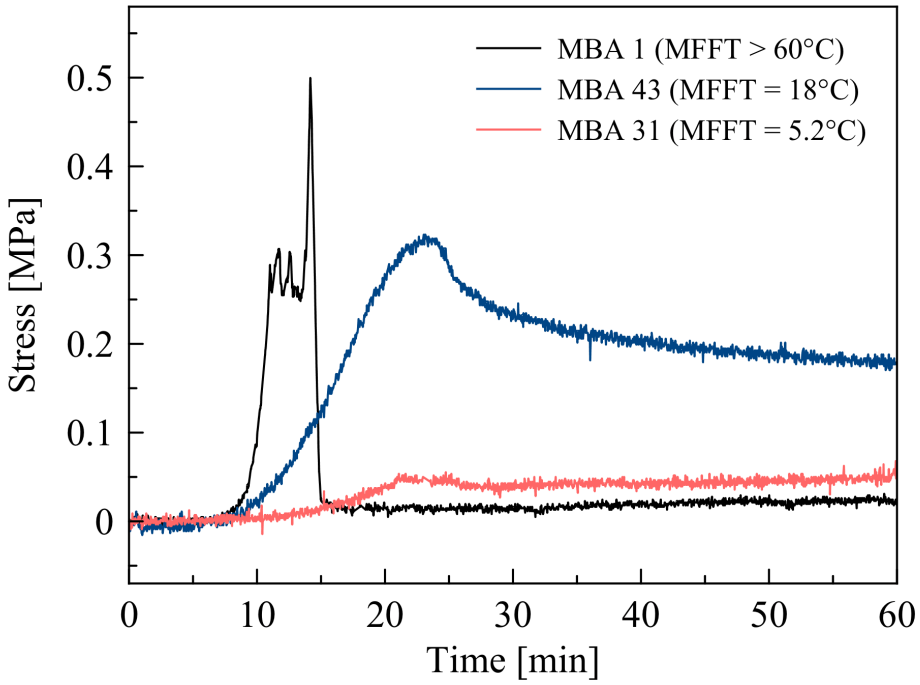

Figure 6.1 Stress development for latex coatings with varying MFFT without coalescing aids. MBA31 and MBA43 form continuous films upon drying at room temperature, whereas MBA1 cracks upon drying.

Stress development curves for samples MBA43 and MBA31 are also shown in Figure 6.1. Both of these latexes form continuous films upon drying at room temperature. The stress development curve for MBA43 has an initial stress-free period followed by a gradual rise in stress, followed by a modest stress relaxation in the coating. For the MBA31 sample, the stress rises very gradually with time and plateaus at a residual stress. The rate of stress development appears to correlate with the MFFT, or rigidity of the latex particles. When the particles are harder (i.e. high MFFT), the stress rises very quickly in the coating. This behavior was also seen in the hard ceramic particle coatings explored in Chapter 5. When the particles do not deform, evaporation causes curved menisci to form between adjacent particles along the free surface. These menisci

quickly reach the maximum curvature (highest capillary pressure) allowed by the porespace. This results in a rapid increase of the capillary pressure in the liquid, and a sharp rise in measured stress to the maximum value.

For softer particles (i.e. lower MFFT), stress development occurs gradually with time. Soft particles can deform as the capillary pressure develops. As the particles deform, the pores close and water is exuded from the coating, this reduces the curvature of the menisci. Not only will the maximum capillary pressure be lower for deformable particles, the elastic modulus of the coating is also lower.

For the latex coatings used in this study, the maximum stress appears to be correlated with the MFFT. This behavior is not unexpected, as the lower MFFT latexes have a lower elastic modulus and should therefore develop less stress for similar strains. Also, the viscoelastic relaxation of stress in the coating will be faster for films with lower T_g polymers (i.e. lower MFFTs). However, this result was not seen in previous studies where the maximum stress was found to be essentially independent of the MFFT.[62,97] It should be noted that past stress measurements were conducted in the presence of lateral drying, which complicates the interpretation of the measured stresses.

Latex particles made from soft, low T_g polymers undergo complete film formation at room temperature; however, the resulting coatings are often tacky and lack the desirable mechanical properties. Likewise, coatings made from hard, high T_g latex particles can provide the desired mechanical properties but cannot form cohesive films at room temperature. One solution to this problem is to mix soft (binder) particles with hard particles (high Tg latex, ceramic particles, etc.); however, the soft binder concentration

must be high enough to give the film sufficient strength.[109] Another solution is the addition of a 'coalescing aid' or 'plasticizer' that effectively lowers the T_g of the latex. Often these additives are volatile molecules (VOCs) that leave the film through evaporation, returning the dried polymer to the original high T_g after film formation has occurred. However, many modern coalescing aids are designed to be low-VOC, reducing the emission of harmful organic compounds into the atmosphere.

The addition of a coalescing aid not only lowers the T_g of the polymer, bust also increases the diffusivity of the polymer chains. Juhue et al.[115] demonstrated this effect by showing the diffusivity of the polymer chains of poly(butyl methacrylate) increased by one order of magnitude when three weight percent coalescing aid (Texanol™) was added to the latex suspension; the diffusivity increased by four orders of magnitude when 12 weight percent was added. More recently, Schroeder et al.[116] showed that the addition of Texanol™ increases the onset of diffusion during the film formation process in common acrylic latex particle coatings.

The effectiveness of a coalescing aid will depend on several factors. First, the volatility or evaporation rate of the coalescent will dictate how long the plasticizing molecules are present in the film. Second, the compatibility of the coalescing aid with the polymer will dictate how efficiently the coalescent will lower the T_g. Third, the solubility of the coalescing aid will dictate where the coalescent molecules will partition themselves in the suspension. For example, Texanol™ is poorly soluble in water, therefore the coalescent will have a higher concentration in the polymer particles. This allows the coalescing aid to promote interdiffusion during the early stages of film

formation when the particles make initial contact. A hydrophobic coalescing aid will partition itself preferentially in the water phase, which means that the coalescing aid becomes more effective during the later stages of film formation when the water content is low. In this study, four coalescing aids were used to investigate the effect of the additives on the MFFT and the stress development of a mid-T_g latex. The details of the coalescing aids are listed in Table 6.3.

Table 6.3 Characteristics of Coalescing Aids

Coalescing Aid	Conventional/Low VOC	Hydrophobic/Hydrophilic
Texanol™	Conventional	Hydrophobic
Optifilm 400	Low VOC	Hydrophobic
Butyl Carbitol	Conventional	Hydrophilic
Benzoflex LC-531	Low VOC	Hydrophilic

Sample MBA43 has an MFFT of 18°C (Table 6.1) when no coalescing aids were added. Figure 6.2 shows the effect of various coalescing aids on the MFFT of the latex coatings. Each of the coalescing aids used in this study was effective at lowering the MFFT at a concentration of three weight percent. Stress development curves for the MBA43 latex with three weight percent coalescing aid are shown in Figure 6.3. From the plot, it is clear that the addition of the coalescing aids decreases the maximum stress attained in the film. At, the concentration levels investigated here, the maximum stress values are very similar for the latex with Texanol™, Optifilm 400, and Benzoflex LC-351. However, the maximum stress was significantly lower for the film containing three weight percent Butyl Carbitol.

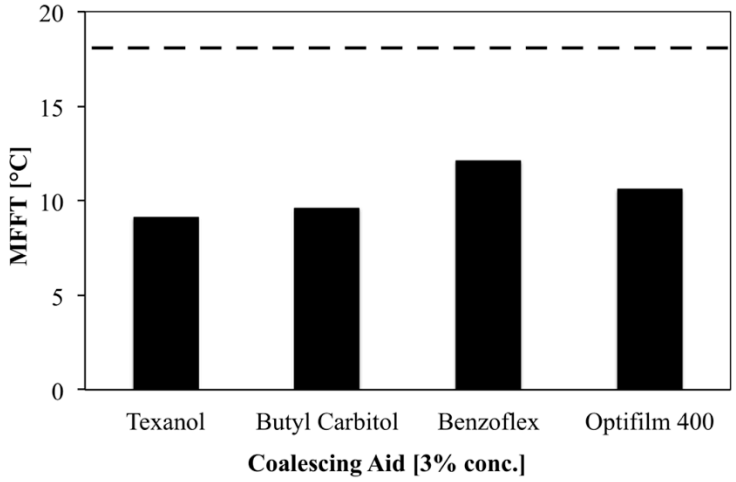

Figure 6.2 Effectiveness of various coalescing aids at lowering the MFFT for MBA43 at a concentration of 3% on the final solids in the coating. Dashed line represents the MFFT of the latex with no coalescing aid.

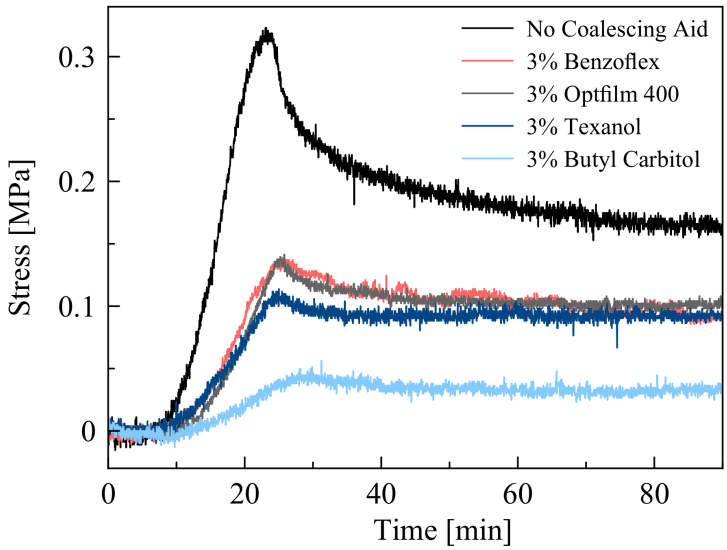

Figure 6.3 Stress development curves for the MBA43 sample (MFFT = 18°C) with various coalescing aids at 3% concentration in the final film.

Additionally, the concentration level of the coalescing aid will also influence the stress development in the drying coating. Texanol™ and Optifilm 400 were used to investigate the influence additive concentration on stress development. In Figure 6.4 the

maximum stress is lowered as the concentration of the coalescing aid increases. Also, the small 'peak' that is present for the film with no coalescing aid begins to disappear as the coalescent level increases. This may be explained by the fact that the particles are becoming softer and can deform to a greater extent as the T_g is lowered with higher concentrations of the coalescing aid.

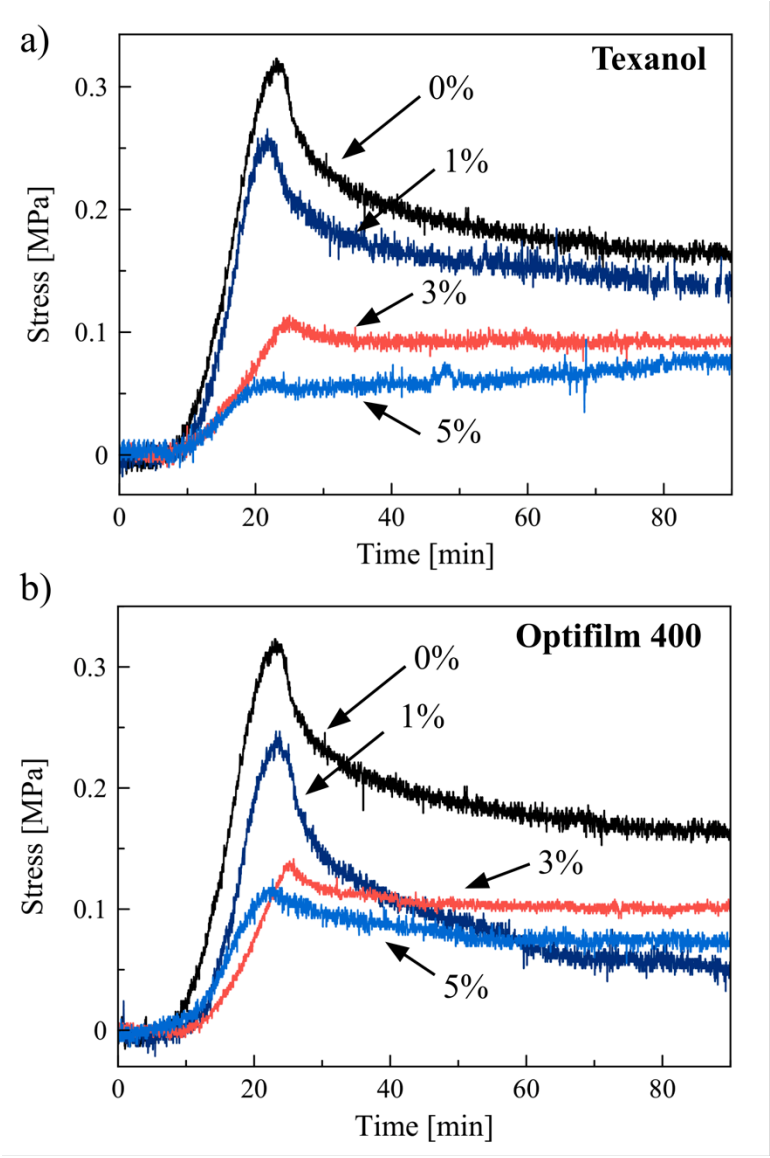

Figure 6.4 Shows the influence of the concentration of a) Texanol™ and b) Optifilm 400 on the stress development in the coating.

6.3.2 *PVDF:Acrylic Blends*

Polymer blend latexes consisting of poly(vinylidene fluoride) (PVDF) and an acrylic copolymer are manufactured at Arkema Fluoropolymers (King of Prussia, PA) and branded as Kynar Aquatec™. These latex materials are used in "cool roof" applications that provide energy savings to customers by reducing cooling costs. The coatings systems are applied as a white polymer coating on rooftops that reflects the majority of solar energy that hits the roof. During weathering test, Kynar Aquatec™ coatings have maintained a solar reflectance and emissivity value of over 0.80 for a period of 7 years after the coating was applied.[9] By reflecting the sun's energy, roof temperatures are reduces providing the customer with lower cooling costs.

Generally speaking, acrylic latexes do not have great UV stability and therefore perform poorly in weathering tests. They also have much lower mildew resistance compared with PVDF coatings. For long-term weatherability and stability, PVDF is preferred for the cool roof applications where the coatings are constantly exposed to harsh environments. However, increasing the PVDF content of the polymer blend increases the MFFT of the latex coating and cracks begin to form when drying at room temperature. This is an unusual phenomenon since PVDF has a much lower T_g (-40°C) than the acrylic polymer in the blended particle. The cause for the increase in the MFFT is thought to be due to small amounts of residual crystallinity in the PVDF polymer. These crystalline regions inhibit polymer diffusion across particle boundaries, which result in weak particle-particle contacts, thereby decreasing the mechanical strength of the particle network. This effect is detrimental as it limits the use of high PVDF content

coatings to OEM (original equipment manufacturer) applications where the coating can be applied at elevated temperatures and controlled drying conditions.

To alleviate the cracking problems encountered at room temperature, a coalescing aid can be added to the formulation or a greater amount of acrylic polymer must be used. Blends of PVDF:acrylic can provide optimal performance without coalescing aids, but the microstructure and film formation behavior of these systems are not fully understood. For these complex latexes, the film formation behavior and stress development is compared for the two PVDF:acrylic particles listed in Table 6.2.

Derek Huang, an undergraduate student, conducted measurements of the MFFT for mixtures of the 50:50 and 70:30 PVDF:acrylic latex particles. By mixing the two particles, a range of overall polymer composition (between the two extremes) in the coating could be achieved. These results were compared with latex blends reported by Katie Crawford,[9] where the 70:30 blended particles were mixed with pure acrylic particles to increase the acrylic content of the coating. The results from the MFFT experiments are shown in Figure 6.5. The MFFT appears to vary linearly between approximately 12°C and 26°C by simply adjusting the ratio of the 50:50 and 70:30 latex particles in the latex mixture.

Increasing the acrylic content of the coating through the addition of pure acrylic particles significantly lowers the MFFT, as shown by the data collected for the PVDF:acrylic – pure acrylic mixtures. This suggests that the while increasing the overall acrylic content in the latex coating is effective in lowering the MFFT and reducing cracking, the distribution of the polymer phases has a more significant

influence. For example, in order to achieve an MFFT below 20°C, the acrylic content of the film would be 40% for the blended systems while the mixed systems could achieve a slightly lower MFFT with only 35% acrylic content. However, for the mixed latex coatings regions of pure acrylic polymer will be present in the final coatings that could prove to be detrimental to the performance of the coating in weathering tests.

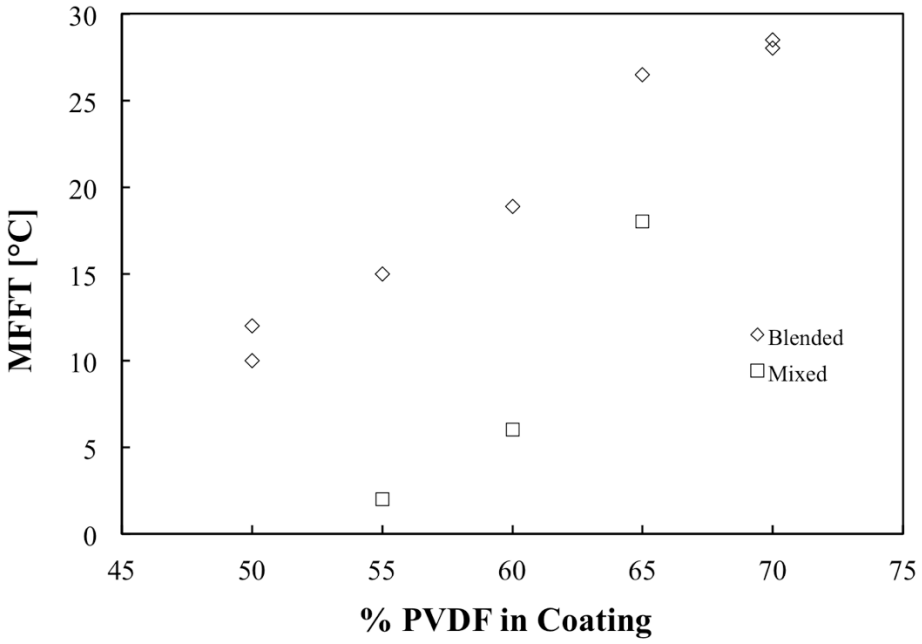

Figure 6.5 Plot showing the MFFT for blends of the PVDF:acrylic latexes (50:50 and 70:30), compared with mixtures of 70:30 PVDF:acrylic particles with pure acrylic particles.

The stress development curves for the two PVDF:acrylic latexes are shown in Figure 6.6 a. The stress development curve for the 70:30 latex, which cracks extensively upon drying, has an initial stress-free period followed by a sharp increase in stress to the first stress peak, followed by a slight relaxation. A video recording of the cantilever during the experiment reveals that the latex coating delaminates from the PDMS wall at this point of dying. Stress relaxes as the delamination propagates; however stress

continues to build across the coating. As the stress magnitude increases, a second stress increase begins and the measured stress rises to its maximum value. When the stress reaches this maximum, cracks form and the stress falls to a negligible value. For the 50:50 latex, the stress development curve has an initial stress-free period followed by a gradual increase in stress to the maximum value followed by only a slight relaxation in stress. The 50:50 film forms a clear crack-free film upon drying. These results indicate the importance of interdiffusion on the cracking behavior of the drying latex coatings. For both latexes, the maximum stress achieved in the coating appears to be about the same. However, only the 70:30 latex forms cracks upon drying. The 50:50 latex has a greater amount of acrylic polymer that can participate in film formation, which increases the mechanical strength of the drying coating. Whereas, the same level of stress in the 70:30 latex causes cracks to form because the limited polymer diffusion across particle boundaries results in an overall weaker coating.

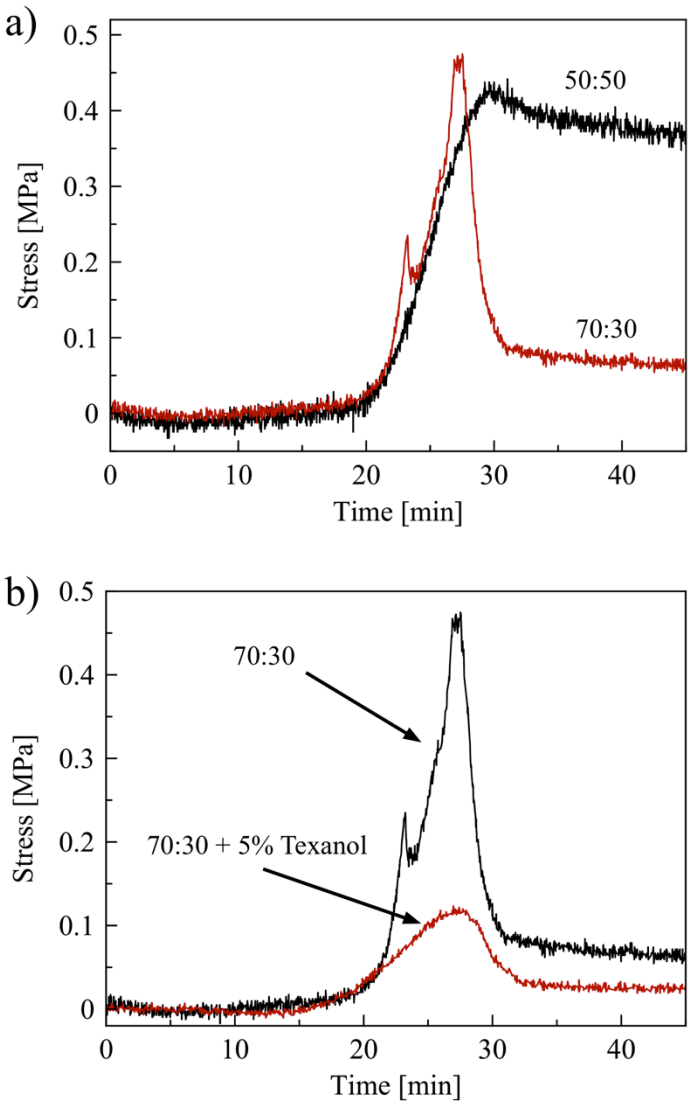

Figure 6.6 Stress development curves for a) the 50:50 and 70:30 PVDF:acrylic latexes, and b) for the 70:30 PVDF latex (with and without Texanol).

Figure 6.6 b, shows the stress development curve for the 70:30 latex, with and without the addition of a coalescing aid. Adding 5% weight Texanol™ lowers the magnitude of stress (by over a factor of 4) that develops during drying, similar to the acrylic latexes discussed in Section 6.3.1. However, the coating still cracks extensively upon drying! One would expect that lowering the magnitude of stress in the film, and increasing the mobility of polymer chains (increasing polymer diffusion), would be

sufficient to alleviate cracking in these latex coatings. However, this may indicate that cracks develop in the coating not due to high stresses, but rather due to the weak particle-particle contacts and low cohesive strength of the particle network. This is an interesting phenomenon that could be investigated further by using various coalescing aids at different concentrations. Characterization of the coating microstructure with cryoSEM may also help reveal the mechanism of crack formation in these coatings.

6.4 *Summary*

Using the cantilever deflection technique with modified walled cantilevers, the stress development of acrylic latex coatings was investigated as a function the MFFT. Additionally, the effect of various coalescing aids and their concentration in the film were investigated as well. Results show that latexes with lower MFFTs develop less stress, more gradually during film formation. This is likely a result of increased particle deformation. The coalescing aids used in this study seemed to have a very similar effect on stress development at a concentration of three weight percent. As the concentration of the coalescing aid increases, the maximum stress in the film decreases as well.

The film formation behavior and stress development was also studied for PVDF:acrylic latexes. The results indicate that the MFFT increases as a function of the PVDF content in the film. However, the distribution of the polymer phases was shown to have a dramatic impact. The MFFT was lowered more effectively (for a film with the same polymer fractions) when pure acrylic particles were blended with the 70:30 PVDF:acrylic particles compared to a film made from a mixture of 50:50 and 70:30 PVDF:acrylic particles. The shape of the stress development curves for the two latexes

had striking differences which could be explained by the fact that the 70:30 latex cracks while the 50:50 does not. When a coalescing aid is added to the 70:30 latex, the maximum stress was lowered; however, the film still cracked upon drying. The film likely cracks due to low cohesive strength in the particle network rather than high levels of stress in the film during drying.

Chapter 7

STRESS DEVELOPMENT AND FILM FORMATION FOR CORE-SHELL LATEX COATINGS[3,4]

7.1 *Background and Motivation*

The ability of isolated latex particles to coalesce and form films underlies a wide variety of industrial applications, including paints, coatings, adhesives, paper coatings, and carpet backing.[1] This process, commonly referred to as latex film formation, dictates many coating properties, and thus the performance of the final products. The complex mechanism of latex film is commonly divided into three stages: consolidation, deformation, and coalescence.[30,109] In the first stage, evaporation brings the latex particles into a consolidated touching network. During the second stage, further drying leads to particle deformation, presumed in this work to be caused by capillary deformation. Throughout the third stage, the film gains mechanical integrity as polymer diffusion eliminates particle boundaries. A more detailed discussion of the latex film formation process can be found in Chapter 2.

3 This chapter was published in adapted form:
Price, K. K.; Wu, W.; Wood, K.; Kong, S.; McCormick, A.; Francis, L. F. Stress Development and Film Formation in Multiphase Composite Latexes. *J. Coatings Technol. Res.*

4 This work received the American Coatings Best Paper Award at the American Coatings Conference, on April 7–9, 2014 in Atlanta, GA

For homogenous latex particles, the film formation behavior varies with the polymer composition.[30,109] Particles containing low glass transition temperature (T_g) polymers easily undergo film formation, but the final films are often tacky and lack desired mechanical properties like film hardness. Particles made from high T_g polymers will form films with sufficient mechanical properties, however film formation is difficult without high temperatures or coalescing aids. Traditional coalescing aids are volatile organic compounds (VOC), which are being phased out due to increasing government regulations and increasing consumer awareness. The conflicting requirements between film formation and performance is often called the 'film formation paradox'.[1] One solution to this problem is to engineer multiphase particles that combine the benefits of both low T_g and high T_g polymers in a single particle, and don't require the use of harmful VOCs to ensure film formation.[117]

Multiphase latex particles can be synthesized to form a wide variety of particle morphologies.[118,119] One the most commonly used morphologies are the core-shell morphology where one phase makes up the core, which is fully surrounded by the second phase. The core-shell particle morphology is often designed with a high T_g core and a low T_g polymer shell.[117] Here, the low T_g polymer in the shell aids in film formation while the high T_g cores give the film mechanical strength. A common characteristic of a latex is the minimum film formation temperature (MFFT), the lowest temperature at which the latex forms a clear, crack-free film upon drying (see Chapter 2 for further details on the MFFT). For composite particles with the hard-core/soft-shell morphology, the MFFT decreases as the thickness of the soft, low T_g polymer shell increases.[120,121] In a separate

study, Juhué and Lang[117] showed that the rate of polymer diffusion between hard-core/soft-shell particles was comparable to that of homogeneous high T_g particles with an added coalescing aid.

When the hard-core/soft-shell morphology is inverted, the low T_g polymer forms the core which is surrounded by a hard, high T_g shell.[122] This morphology (soft-core/hard-shell) has received less attention in the literature because of concerns that high T_g polymer in the shell would will result in poor film formation. Theoretically, the high T_g polymer in the shell not only restricts polymer diffusion across particle boundaries, but also restricts the mobility of the low T_g polymers in the particle core. For example, composite core-shell particles with low T_g poly(n-butyl acrylate) (PBA) cores and high T_g poly(methyl methacrylate) (PMMA) shells, did not undergo film formation below the T_g of PMMA when the shell content was high (50%).[123] Only when the coverage of the shell was incomplete did the composite particles display good film formation.

However, using similar particles, Santos et al.[124] show that particles with a 20% weight shell can undergo film formation at room temperature to form mechanically robust coatings. The combination of coalescent-free film formation and sufficient mechanical properties was attributed microstructure of the dried film: the soft cores formed inclusions in a continuous matrix of densely packed, deformed shells. Thus, the authors concluded that the two conflicting properties can be achieved simultaneously with complete shell coverage; however, the overall shell content of the particles needs to be low. When designed appropriately, the soft-core/hard-shell particle morphology can provide increased film hardness to low VOC architectural paints, because the high T_g

shell limits the amount of the softer, low T_g core polymer that is exposed to the surface. The promise of the soft-core/hard-shell particle morphology has garnered interest in these materials, both in terms of their film formation behavior and also in their application as binders in paint formulations.

During film formation, stress development in the coating has the potential to initiate coating defects and decreases the durability of the coating.[16,61,96,102,125] Many researchers have employed the use a cantilever deflection technique to characterize the stress development in latex coatings throughout the drying process.[60–62,97,126] However, stress development for films made of composite core-shell latex particles has received little attention in the literature. One limitation of the cantilever deflection technique is that only an average stress may be calculated from a measurement of the cantilever deflection. Lateral drying, which is common in latex coatings, results in non-uniform stress development across the cantilever, complicating interpretation of the results.[34,44,55,61,127]

In order to control the lateral drying behavior, many authors alter the drying conditions or the properties of the coating suspension (e.g. solids loadings, viscosity, etc.) to promote a condition of uniform saturation.[43,44,49,102] Another technique that is used to limit lateral drying is to introduce a wall or border along the perimeter of the substrate, this eliminates the thin edges and promotes 'top-down' drying.[73,77,79,80,103] Based on previous results,[8,9,51] walled cantilevers were developed and used that allow stress measurements without the interference from lateral drying.

In this study, the film formation behavior was investigated for a series of soft-core/hard-shell particles as a function of particle size, shell ratio (weight shell / weight particle), and the core and shell T_gs. The film formation behavior of these particles was characterized by stress measurements, cryogenic scanning electron microscopy (cryoSEM), and atomic force microscopy (AFM). Additionally, the core-shell particles were evaluated in a high gloss paint formulation. To our knowledge, the study is the first that attempts to relate the film formation behavior and stress development in the film to the performance of the latexes in a practical paint formulation.

7.2 *Materials and Methods*

7.2.1 *Core-shell Latex*

The core-shell latex samples used for this study were provided by Dr. Wenjun Wu with Arkema Coatings Resins (Cary, NC). Three acrylic monomers: butyl acrylate (BA), methyl methacrylate (MMA), and methacrylic acid (MAA) were used to prepare the multiphase particles. The core-shell morphology was achieved through a semi-continuous, 2-stage emulsion polymerization process enforced by an "inverted" core-shell monomer feed profile.[122] In other words, the first monomer mixture has a higher MMA/BA ratio than the second stage mixture, thus, the first stage is more hydrophilic. The first stage monomer mixture creates the hard, high T_g shell around the soft, low T_g core form from the second stage monomer mixture. A fixed amount of acid monomer was included only in the first stage making the first monomer mixture even more hydrophilic, allowing it to form the outer shell of the particle during polymerization. The glass transition temperatures of the core and shell polymers can be tuned by adjusting the

weight fractions of PMMA and PBA, the resulting T_g can be estimated using the Fox equation, Eq. 6.1.[113] The core-to-shell ratio was varied while keeping the total monomer content and all other process parameters the same.

The characteristics of the latex samples synthesized for this study are compiled in Table 7.1. The T_g values reported in this paper were obtained from the initial ramp for fast-heat DSC experiments. The MFFT was measured on a rectangular temperature gradient bar and is identified as the point where the latex formed a clear and crack-free film (cloudy-clear transition). The reported values for the volume-averaged (D_v) and the number-averaged (D_n) particle sizes were measured using a Nanotrac 150 (Microtrac) particle size analyzer.

Table 7.1: Sample characteristics for soft-core/hard-shell latex

Sample[1]	Measured T_g [°C]		ΔT_g	Particle Size [μm]		Shell Ratio	MFFT
	Core	Shell	°C	D_v	D_n	wt %	[°C]
AL25	-2.8	55.8	58.6	0.146	0.124	25	<0
AL35	-3.4	58.7	62.1	0.142	0.122	35	19.8
AL50	-2.8	56.1	58.9	0.172	0.145	50	34.4
AS25	-3	63.9	66.9	0.063	0.053	25	<0
BL25	10.9	50.4	39.5	0.137	0.120	25	8.5
CL50	19.5	33.5	14.0	0.178	0.156	50	16.9
CS50	11.3	23.2	11.9	0.076	0.065	50	14.7

[1]Sample designation: first letter indicates ΔT_g (A - high, B – medium, C – low); the second letter indicates particle size (L – large, S – small); the number indicates the shell ratio.

7.2.2 *Stress Measurement*

A modified cantilever deflection technique was used to characterize stress development *in-situ* during drying.[55,56] For this study, cantilevers with PDMS walls around the perimeter were used to limit lateral drying and increase uniformity. To fabricate the walled cantilevers, PDMS (Sylgard® 184, Dow Corning) walls were molded onto silicon cantilevers (6 mm x 60 mm) that were cut from (100) silicon wafers, see Fig 5.2a. The Young's modulus and Poisson's ratio of the cantilevers were taken to be E = 169 GPa, $\nu = 0.064$, repectively.[106]

Details of the experimental procedure and a diagram of the experimental apparatus can be found in Chapter 3, Figure 3.2. To calculate the coating stress, a modified version of the Corcoran[55] equation was used, see Eq. 5.2, which accounts for the reduced coating area on the cantilever because of the wall. Throughout the experiment, the temperature and relative humidity are maintained at 22°C ± 1°C and 40%RH ± 2% respectively. After the experiment, the dried coating thickness was measured with a micrometer.

7.2.3 *Microstructure Characterization Methods*

Cryogenic Scanning Electron Microscopy (cryoSEM)

CryoSEM was used in this study to investigate the film formation process during drying. Latex coatings were prepared by drop casting a controlled volume of the suspension onto silicon chips without walls (5 mm x 7 mm) that were pre-scored along their mid-section. Under ambient conditions, the coatings were dried for various times

before plunge freezing into a small bath of liquid ethane that was surrounded by liquid nitrogen. Due to safety concerns, the freezing procedure was conducted in a fume hood. After freezing, the samples were transferred to an Emitech K-1250 preparation chamber, which is held at approximately -169°C under high vacuum. Within the preparation chamber, the samples were fractured along the pre-scored mid-section line, which exposes their cross-sections. For these samples, no intentional sublimation was performed so that the water content in the coating could be observed. Approximately 5 nm of platinum was sputter-coated onto the frozen fracture surface to reduce charging. Samples were transferred to a Hitachi S-4700 FESEM (Hitachi, Pleasanton, CA) and imaged in secondary electron mode at approximately -150°C on a stage cooled by liquid nitrogen.

Scanning Electron Microscopy

Conventional (room temperature) SEM was performed to confirm the core-shell particle morphology and characterize the microstructure of the fully dry films. The core and shell phases of the particle have similar compositions (i.e. same monomers), except the shell phase contains a small amount of methacrylic acid. Uranyl acetate (UA) can be used to preferentially stain polymers or polymer phases that contain acid groups.[128] The staining process also hardens the latex particles and protects against damage from the electron beam.

To investigate the particle morphology, the latex particles were stained prior to film formation. To stain the particles, a diluted latex suspension (0.1% solids) was mixed with equal parts of a dilute UA solution (0.15% UA). After 20 minutes, a small

volume of the mixed suspension was spread onto a silicon chip and allowed to dry under ambient conditions. To characterize the morphology of the dried coating, the latex suspension was dried on a silicon ship, and then fractured under liquid nitrogen to expose the cross-section. The chip (with the fracture surface exposed) was placed in a 0.15% UA solution and stained for 20 minutes. After staining, the film was rinsed with distilled water and allowed to dry. Approximately 5 nm of platinum was sputter coated onto the sample surface to reduce charging. The samples were imaged on either a Hitachi SU-8230 ultra high-resolution FESEM of a Hitachi S-4700 FESEM equipped with a back-scattered electron (BSE) detector. The BSE detector provides enhanced compositional contrast compared to standard secondary electron (SE) detector.

To characterize the surface of the dried latex films, atomic force microscopy (AFM) was used. A summer undergraduate student, Stephanie Kong, who was part of the REU program at the University of Minnesota, performed the AFM measurements. The AFM images were recorded with an Agilent 5500 scanning probe microscope operating in contact mode. Before imaging, the latex coating was prepared on a 5 mm x 7 mm silicon chip, dried completely, and allowed to cure at room temperature for 24 hours prior to the experiment. Analysis of the AFM data was performed with the Gwyddion software package.

7.2.4 *Paint Properties*

The core-shell particles were evaluated in a solvent-free, high gloss formulation with 17% pigment volume concentration (PVC) and 38% volume solids (VS). It is reasonable to anticipate that the differences in the composite particles will be discernible

in a high gloss paint formulation. High-gloss paints have a high binder content, (low pigment content), so it is reasonable to assume that the results can be correlated to the film formation behavior of the latex-only films. The formulation details of the paint can be found in Table 7.2.

Table 7.2. High Gloss Paint Formulation

		Density lbs/gallon	Mass (lbs)	Vol (Gallons)
Common Grind				
Water		8.33	32.0	3.8
Proxel GXL	biocide	9.41	1.5	0.2
BYK 025	defoamer	8.34	0.5	0.1
Tamol 1124	dispersant	9.9	4.2	0.4
Ammonia (28%)	neutralizer	7.7	4.0	0.5
R-706	TiO_2	33.3	210.0	6.3
Water		8.33	53.8	6.5
Total Grind			306.0	17.8
Letdown				
Multiphase polymer	binder	8.85	580.0	65.5
BYK 025	defoamer	8.34	2.0	0.2
Rheloate 278	rheology modifier	8.58	8.0	0.9
Water		8.33	136.0	16.3
Total Paint			1032.0	100.8
Paint Properties				
Weight Solids %		50.2		
Volume Solids %		38.4		
PVC%		17.0		

7.2.5 *Paint Performance Tests*

Block Resistance

Blocking is the tendency for two paint films to stick together when they are placed in contact with each other. The block resistance tests for the paint films were conducted at Arkema Coating Resins (Cary, NC), under ASTM D-4946 specifications. Room temperature and elevated temperature block performance was rated from 0 (poorest) to 10 (best). The test was run in triplicate and the average value was reported. The test paints were prepared on Leneta 3B opacity charts using a 3-mil Bird drawdown bar. The films were dried in a controlled temperature and controlled humidity (CT/CH) chamber for 1 day. For the room temperature (RT) block test, two square strips of 2.54 cm x 2.54 cm were placed together (paint film against paint film) under a load of 454g. After 24 hours, the strips were separated and the block performance was evaluated. For the elevated temperature (ET) block test, the paint strips (after 1-day drying at CT/CH) were placed in a 120ºF oven for 30 minutes under a load of 1000g. The films were allowed to cool for 30 minutes before they were separated, and the block performance was evaluated.

Scrub Resistance

Scrub resistance is a measure of the coatings toughness under mechanical scrubbing, which is often compared to a control sample. The scrub resistance experiments

were conducted at Arkema according to ASTM D-2486 specifications. The relative scrub resistance for the paint samples was evaluated on the Gardner Straight Line Washability and Wear Abrasion Machine. A semi-gloss acrylic paint (23%PVC, 38%VS) was used as a control to minimize the test variability. Both the control paint and the test paints were applied side-by-side at a wet film thickness of 7 mils over Leneta black plastic charts and allowed to dry for 7 days at 77ºF and 50% relative humidity. During the test, nylon bristle brushes are used to scrub the paint films. The brushes were pre-conditioned by running 400 cycles before the test began. 7 mL of a standardized abrasive scrub media (#SC-2 from the Leneta Company) and 5 mL of water were placed on the films at the beginning of the test and again after every 400 cycles until failure. The test was done in triplicate and the number of cycles to failure was recorded. The results were reported as percentage of the control.

7.2.6 *Data Analysis Using JMP*

JMP statistical software (SAS Institute) was used to analyze the MFFT and various application results conducted at Arkema. The experimental results can be modeled using a multiple regression data fitting method, and the morphology parameters displaying a statistically significant impact can be identified.

7.3 *Results and Discussion*

7.3.1 *Core-Shell Particle Morphology*

To investigate the particle morphology, the latex particles were stained in a UA solution, dried, and imaged with an SEM at room temperature. As an example, the core-

shell morphology of the BL25 latex is apparent in the back-scattered electron (BSE) image shown in Figure 7.1a. Back-scattered electrons are elastically scattered from nuclei in the sample and are highly dependent on the atomic number of the atoms in the sample.[128] Heavier atoms (higher atomic number) scatter electrons more effectively; therefore, heavier atoms appear brighter in BSE images. Due to the staining process, uranium atoms are present in the shell polymer; hence, the shell appears bright. From this image, the shell appears to completely surround the core for the BL25 sample.

The morphology of the dried film and the distribution of the core and shell phases were investigated by staining fractured cross-sections of fully dried films and imaging with a BSE detector. Figures 7.1b and 7.1c show the morphology of the dried film for the AL25 and CL50 samples; the films were dried at room temperature and allowed to age for 1 week under ambient conditions before fracture. For the AL25 sample, Figure 7.1b, some particles appear to have a bright shell fully surrounding a darker core. However, for other particles in the film the shell appears discontinuous. In the CL50 film, Figure 7.1c, the core-shell morphology of the particles is clearly evident. The dried film shows a well-ordered structure of bright particle shells surrounding darker cores. Additionally, the shell phase appears to form a continuous network throughout the coating. The CL50 sample has a greater shell ratio (i.e. thicker shell) that is more easily imaged with SEM using the BSE detector. Similar morphologies were observed for the other latexes developed for this study. The images shown in Figure 7.1 give evidence of a core-shell structure for the latexes used in this study. However, the resolution of the BSE detector is limited, which makes it difficult to image the shell phase, especially when the shell

ratio is small, as in the AL25 film. Further confirmation requires the use of high-resolution TEM to image the particles and films in greater detail.

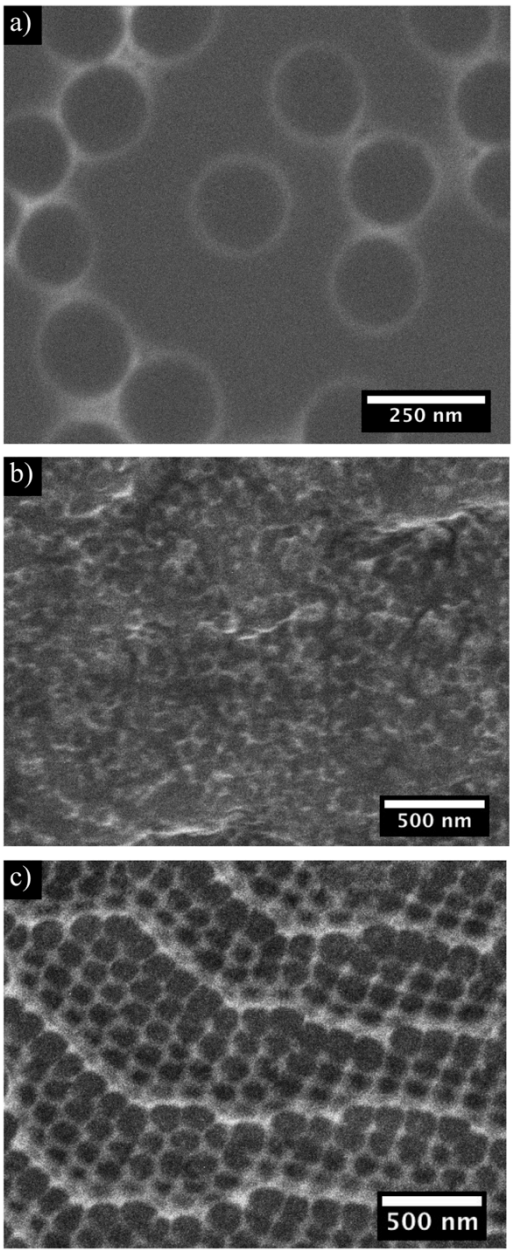

Figure 7.1 Room temperature BSE images of (a) BL25 particles stained in solution for 20 minutes and dried on an SEM stub (b) a stained fracture surface from an AL25 film aged for 1 week, and (c) a stained fracture surface from a CL50 film aged for 1 week.

7.3.2 *Film Formation*

Past studies have shown that the MFFT of a latex is influenced by many factors including the particle size, polymer composition, and particle morphology.[109,120,121,129,130] Determining the MFFT for a latex sample is a relatively simple process, and is commonly used throughout the coatings industry as a standard to describe the film formation behavior of latex particles. While knowledge of the MFFT is useful, a measurement of the MFFT only provides a criterion for bulk film formation and does not provide information on the microscopic behavior of the latex particles. Combining MFFT measurements with other experimental techniques, like cryoSEM and AFM, thus provides a more complete picture of the film formation process. This section explores how the particle size, shell ratio, and composition of the core-shell particles affect the film formation behavior from both the macroscopic and microscopic levels.

On the microscopic level, cryoSEM can be used to visualize the film formation process. CryoSEM is a powerful characterization tool that allows direct, high-resolution imaging of the coating microstructure before it is completely dry.[10,70,104] The sequences of cryoSEM images (obtained using the secondary electron detector) in Figure 7.2 show the evolution of coating microstructure during the film formation process for composite latex particles. A limitation of cryoSEM is that information on particle morphology and phase distribution in the films is not accessible because it is not possible to stain at cryogenic temperatures.

Figures 7.2a and 7.2d are cryoSEM images of the frozen cross-sections of a CL50 and BL25 film early in the film formation process. At this stage of drying the coating is

still wet and the coating suspension is still fluid. Hence, the cryoSEM images show randomly distributed particles fully encased in a frozen ice matrix. The particles in the images appear bright due to their protrusion from the frozen matrix and the resulting high secondary electron emission, not due to any staining procedures. There are also many crater-like structures on the fracture surface that indicate the location where a latex particle once was before the fracture halves were separated. There are also many elongated structures, or "pullouts" that formed during fracture. This unusual deformation is related to the small size of the latex and the constraint of the ice matrix; a complete discussion of these artifacts can be found in Section 2.4.3

CryoSEM cross-sections of the CL50 and the BL25 films in the intermediate stages of drying are shown in Figs. 7.2b and 7.2e. Here, the latex particles form a touching network but the space between particles remains filled with water. Many of the latex particles were removed during fracture; the white arrows indicate the "honeycomb-like" structure of frozen water that fills the spaces between the particles. Figures 7.2c and 7.2f show cryoSEM cross-sections for the coatings in the late stages of film formation. The coatings were dried under ambient conditions and allowed to cure at room temperature for 5 hours, therefore very little water content is expected in these films. The CL50 film (Figure 7.2c) displays a high degree of ordering while the BL25 film (Figure 7.2f) has a more typical appearance where the structure in the film is more disordered. When no water is present, the formation of merged "pullouts" indicates polymer diffusion between neighboring particles.[67] During coalescence, polymer chains diffuse across particle boundaries, greatly increasing the adhesion between adjacent

particles. When the coating is fractured, merged "pullouts" form that bridge the partially coalesced particles. In the BL25 film (Figure 7.2f) there are many merged pullouts; however, in the CL50 film (Figure 7.2c) the pullouts are confined to individual particles. This behavior is expected as the CL50 film has a higher MFFT and should have a lower extent of film formation compared to the BL25 sample.

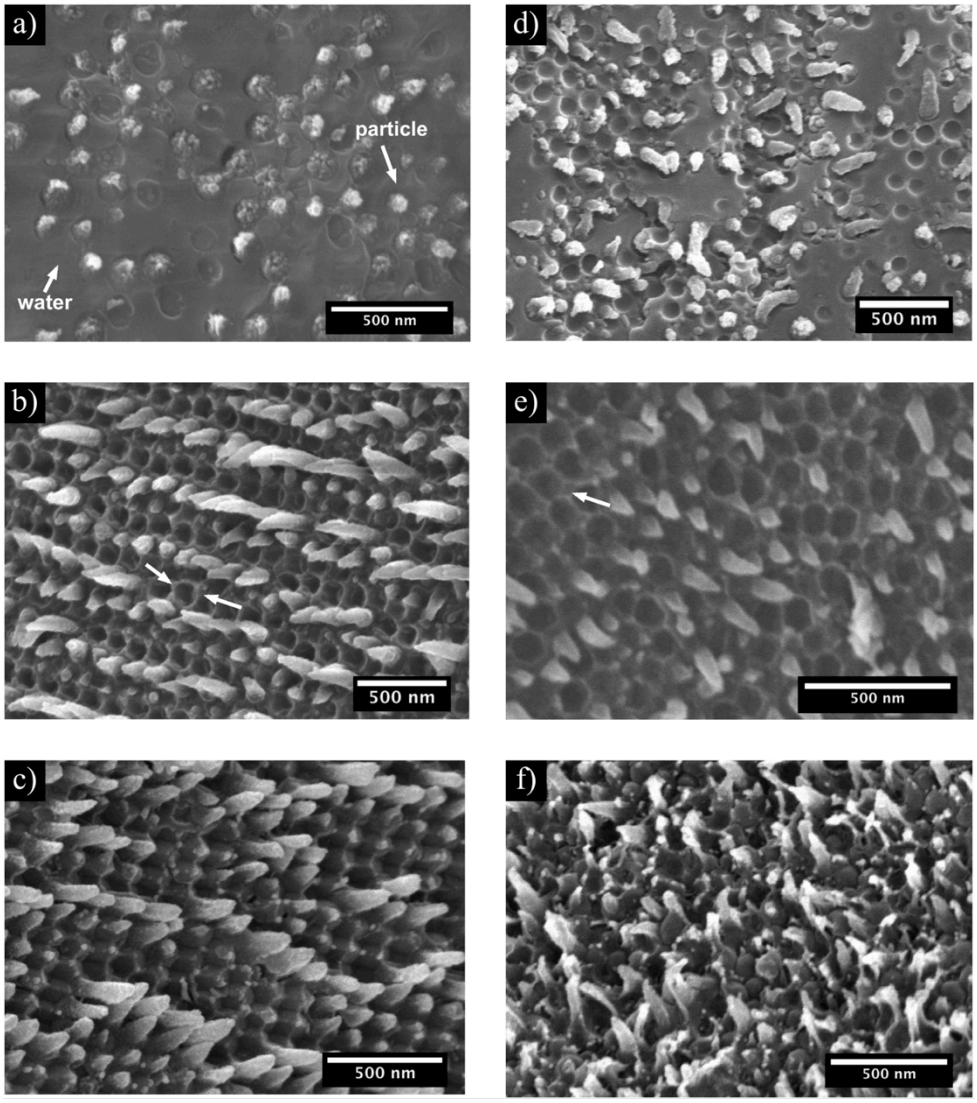

Figure 7.2 CryoSEM cross-sectional images CL50 dried in ambient conditions for (a) 8 min (b) 18 min (c) 5 hrs and BL25 dried for (d) 10 min (e) 20 min (f) 5 hrs. The white arrows in (b) and (e) mark the position of frozen water that filled the space between the particles.

For core-shell composite latex particles, the polymer composition of the shell and the shell thickness strongly influence the MFFT. [120,121,130] The effect of shell ratio on the MFFT is clearly illustrated by comparing the results from the AL25, AL35, and AL50 samples. For a shell ratio of 25% (i.e. AL25) the MFFT is close to the measured core T_g (see Table 7.1); however, as shell ratio increases (i.e. AL50), the MFFT approaches the measured shell T_g. This result suggests that when the shell ratio is low (thin shell), the high T_g shell does not dominate the film formation behavior. However, as the shell ratio increases, the shell becomes thicker and the high T_g shell begins to restrict particle deformation and limit film formation. This explanation is supported by the topographic AFM images of AL25, AL35, and AL50 shown in Figure 7.3. The sequence of AFM images clearly shows that particle deformation and coalescence are strongly affected by the shell ratio. These results are consistent with others using AFM to explore film formation and coalescence for core-shell latex particles.[119,130,131]

The influence of the shell ratio (shell thickness) on both the particle deformation and the MFFT is clear when the difference between the T_g of the core and shell polymers (ΔT_g) is large. However, when the ΔT_g is smaller, the relationships are less well defined. For example, the measured MFFTs for films made from the CS50 and CL50 latexes (smaller ΔT_g) are close to the measured core T_g despite having a high shell ratio. A smaller ΔT_g between the core and shell phases means that there is greater compatibility between the polymers. This increased compatibility may result in an interphase region, or a less defined boundary between the core and shell. This suggests that both the shell ratio and ΔT_g are important variables for the film formation performance of core-shell

latex particles. The MFFT data was analyzed using JMP; the analysis found that the shell ratio as well as the interplay of shell ratio and ΔT_g (the interaction term between shell ratio and ΔT_g) were statistically significant parameters while the particle size was not a main contributor.

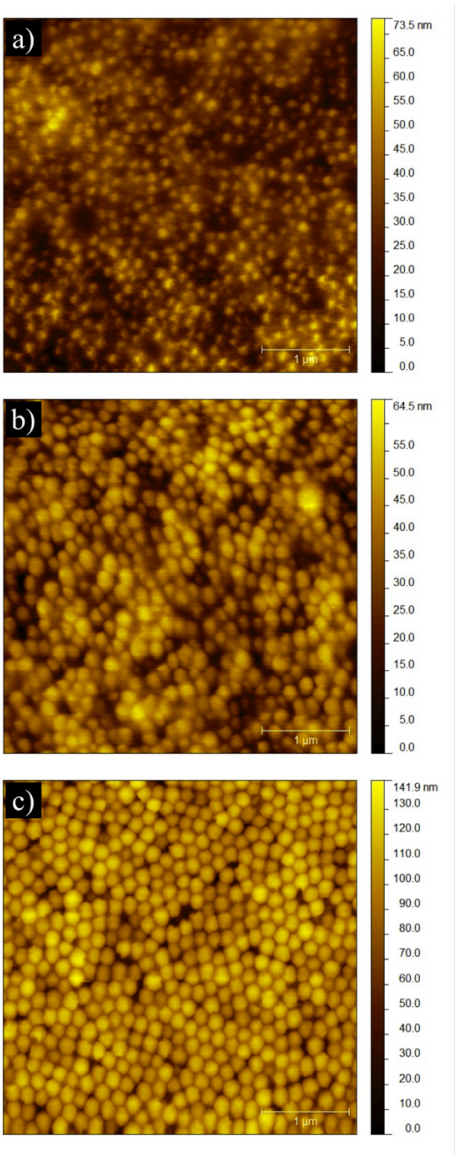

Figure 7.3 Topographic AFM images, obtained in contact mode, of (a) AL25, (b) AL35, and (c) AL50. For a low shell ratio, individual particles become less discernable and the surface becomes smoother. Each image is 4 µm x 4µm.

Previous studies with homogeneous latex particles have shown that smaller particle sizes can significantly lower the MFFT.[129] For the core-shell latexes used for these studies, the MFFT dependence on particle size could not be confirmed between AL25 and AS25 (both have an MFFT < 0°C); however, the MFFT for CS50 (14.7°C) was slightly lower than CL50 (16.9°C). Kendall and Padget[132] proposed that the deforming force during film formation is inversely proportional to the particle radius. As a result, smaller particles tend to deform to a greater extent resulting in smoother films,[133] this behavior is also beneficial for higher gloss development in paint systems.

Figure 7.4 shows topographic AFM images (acquired in contact mode) comparing latex films made from samples with different particle sizes: AL25/AS25 and CL50/CS50. For the films composed of smaller particles (AS25 and CS50), the AFM images have a more uniform (i.e. smoother) appearance than the films composed of larger particles (AL25 and CL50), see Figure 7.4. The roughness of the film surface is often reported by the root mean square (RMS) roughness, which can be calculated from the AFM data. Table 7.3 shows the connections between particle size, MFFT, and surface roughness found from the AFM data. The RMS roughness was found to be lower for film made from smaller particles. The MFFT and AFM data supports the theory that smaller particles undergo film formation more easily than large particles, which results in a smoother film surface.

Table 7.3 MFFT and AFM Roughness Data

Sample ID	RMS Roughness [nm]	MFFT [°C]
AL25	9.54 nm	<0
AS25	2.97 nm	<0
CL50	6.01 nm	16.9
CS50	2.56 nm	14.7

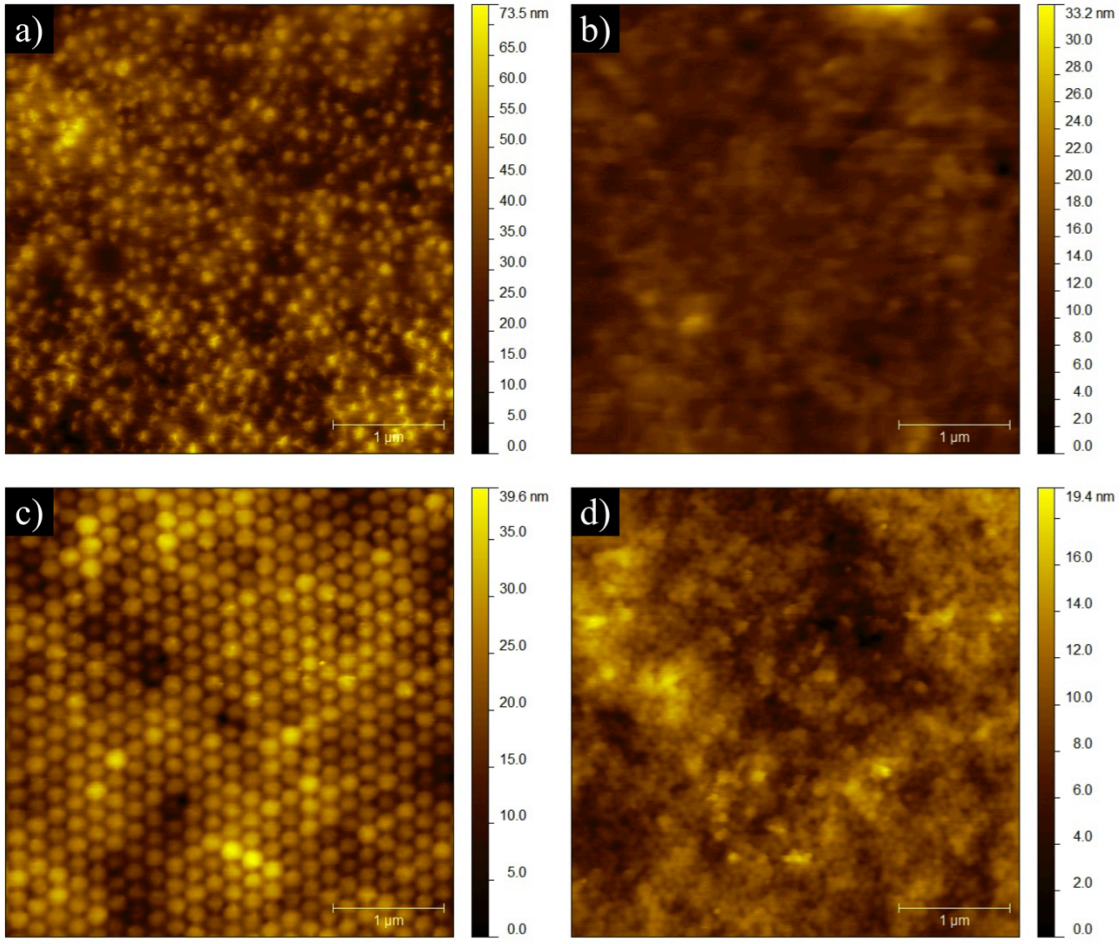

Figure 7.4 Topographical AFM images, obtained in contact mode, of (a) AL25, (b) AS25, (c) CL50, and (d) CS50, illustrate the influence of particle size on the film roughness. Each image is 4 µm x 4µm.

It is clear from the results presented in this section that particle morphology plays an integral role in the film formation behavior of core-shell latex particles. Increasing the shell thickness of the resulted in limited particle deformation and higher MFFTs. While smaller particles and thinner shell thicknesses provided sufficient particle deformation and coalescence at room temperature. To successfully engineer multiphase core-shell latex particles with the desired film formation properties the influence of the shell ratio, $\Delta T_{g,}$ and particle size must be considered.

7.3.3 Stress Development

The evolution of stress in a latex coating during drying has been investigated previously for homogeneous latex particles,[60,61,96,97,126] ceramic-latex blends,[62] and even core-shell latex particles.[60] However, there have been no comprehensive studies on the influence of particle morphology on stress development. Results from previous studies indicate that the magnitude of stress and the stress evolution are affected by the mechanical properties of the particles in the coating.[61,62] For latex particles with core-shell structure, the mechanical behavior of the particles is expected to be governed by the particle morphology. This section explores the effects of particle morphology on stress development during drying.

To suppress lateral drying, the latex coatings were prepared on walled cantilevers for the stress measurements. Without the influence of a lateral drying, the stress development curve for the AL25 sample, a film forming latex, can be divided into three distinct stages, shown in Figure 7.5. During stage I, the coating is stress-free as particles are freely suspended and the coating is fluid. As the coating dries, water evaporates and

the volume fraction of particles (ϕ) increases until the particles form a consolidated (touching) network capable of supporting a stress. In Figure 7.5, stress development appears to begin around six minutes, marking the beginning of stage II. At the start of stage II, the particle volume fraction is estimated (from weight loss data) to be ϕ=0.65, corresponding to a condition of random close packing. If a lateral drying front is present, stress development begins immediately as the coating dries first near the edges. In this situation, the development of stress does not correlate with the particle volume fraction reaching close packing over the entire film.

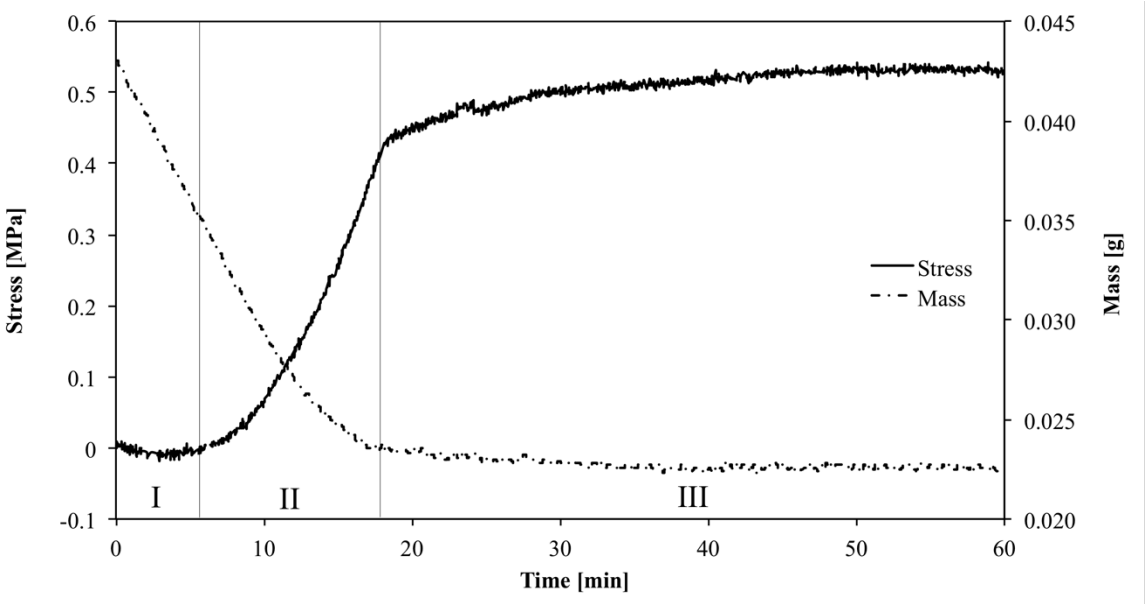

Figure 7.5 Stress development and weight loss data for coatings of AL25 dried at 22°C and 40% RH. The dried thickness of the coating was approximately 80 μm.

During stage II, stress develops gradually and evaporation (mass loss) slow, see Figure 7.5. Stress develops in the coating as water evaporates and capillary pressure builds in the liquid. If this capillary pressure is sufficient to deform the latex particles, they will fill the void spaces in the particle packing.[61] As the particles deform, the

particle volume fraction increases from ϕ=0.65 at the start of stage II and approaches unity (ϕ=1) at the end of drying. Consequently, the elimination of void space in the coating requires an isotropic volume reduction of the film. Normal to the substrate, the coating may freely respond to this shrinkage. However, adhesion of the coating to the substrate constrains the in-plane shrinkage, resulting in the development of a biaxial tensile stress in the coating. The rate of mass loss falls throughout stage II as particles deform and transport of water through the particle network is restricted.

The final stage of drying, stage III, begins once most of water has been removed from the coating and stress development begins to slow considerably. In stage III, further weight loss from the film occurs slowly, suggesting any remaining water leaves the coating through diffusion. Only small increases in stress are associated with the removal of the remaining water. For this material, the residual stress remains in the coating and there is no observable stress relaxation in stage III. However, this behavior will differ depending on the mechanical properties of the polymers in the coating.

To investigate the effect of shell ratio (i.e. shell thickness) on stress development, the evolution of stress for films made from the AL25 and AL50 samples are compared, see Figure 7.6. Coatings made from the AL25 latex form clear, crack-free films upon drying. By contrast, the AL50 latex displays poor film formation and the coatings crack extensively during drying, Figure 7.6a. For AL50, stress generation begins at approximately the same time as AL25, corresponding to the particles forming a close-packed network. Once stress generation begins, stress increases much more rapidly for AL50. A steep increase in stress as the particles reach close packing is typical for

coatings made from hard elastic particles.[61,62] After around 9 minutes of drying, visual inspection of the AL50 coating shows that cracks have formed and the coating has delaminated near the wall. The formation of cracks and crack propagation relieves some of the stress in the coating and slows stress generation. When the maximum stress is reached at approximately 14 minutes a large central crack forms down the center of the cantilever. Stress in the coating is slowly relieved as cracks continue to propagate and the coating delaminates from the substrate.

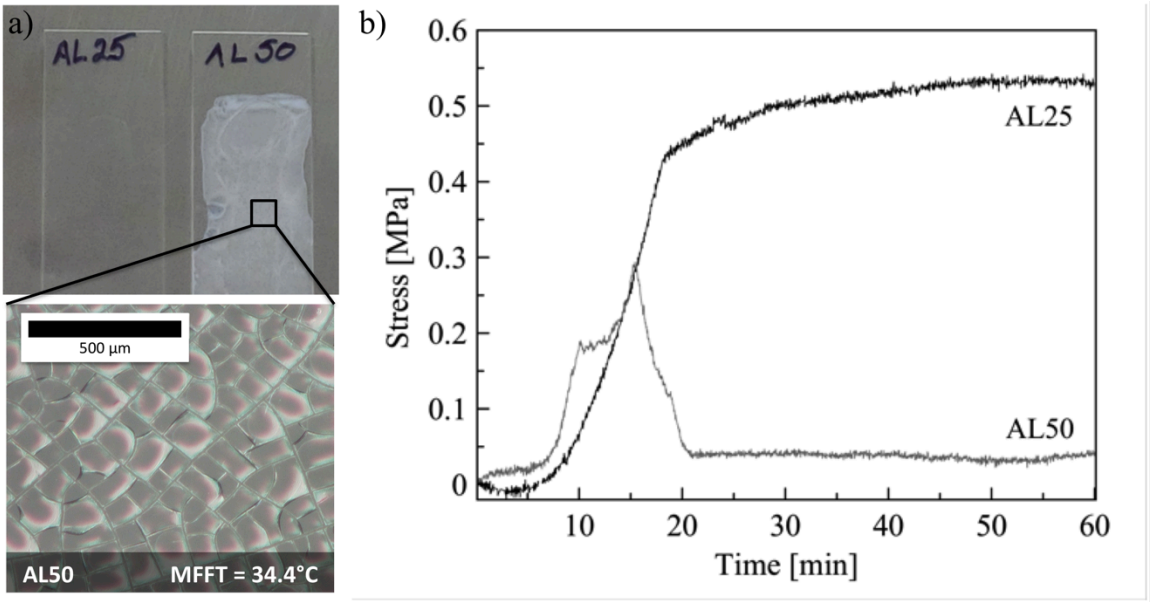

Figure 7.6 (a) Photographs of the films formed from the AL25 and AL50 latex samples. (b) Effect of shell ratio on the stress development profile for AL25, a film forming latex, and AL50, a non-film forming latex. The dried thicknesses of the films are approximately 80 µm.

Cracks form in latex films when the magnitude of the tensile stress reaches a critical level for crack initiation.[95,96,104] The critical stress needed for crack propagation is related to the mechanical properties and thickness of the coating. For the AL25 film, the stress never reaches this critical level and cracks do not form. Conversely, the AL50

film, forms cracks at a critical stress that is lower in magnitude than the maximum stress reached in the AL25 film! This suggests that the AL50 film cracks due to poor cohesive strength of the network rather than due to high levels of stress in the coating. The diffusion behavior of the polymer chains across the particle boundaries should be similar between the AL25 and AL50 because the T_g of the shells are approximately the same. However, particle deformation, as governed by particle morphology, varies greatly as shown by the AFM images in Figure 7.3.

The shell thickness in AL50 is greater than in AL25. For AL50, the thick hard shell restricts particle deformation (see Figure 7.3), which limits the area of the particle-particle contacts in the network. When particles deform, the particles flatten along the particle-particle contacts and achieve intimate contact. For rigid particles, there is little deformation and no flattening at the particle-particle contact points. Additionally, the high T_g polymer in the shell is not expected to extensive diffusion across particle boundaries. This combination of limited deformation and poor coalescence results in a coating that is weaker and more susceptible to cracking. Hence, AL50 cracks at a relatively low stress.

The comparison between AL25 and AL50 indicates that for particles with high T_g shells and low T_g cores, it is possible to achieve good film formation as long as the shell does not greatly restrict particle deformation. Another variable, not explored in this work is the relative T_g of the shell compared to the drying temperature. This difference in these temperatures will affect the ability of particles to undergo film formation, which is evidenced by the existence of an MFFT for latex films.

Another important variable of the particle morphology is the T_g of the core and shell polymers. Figure 7.7 shows the stress development profiles for films of AL25 and BL25, which mainly differ in their core T_g with the other variables remaining fairly constant. Both AL25 and BL25 form continuous films at room temperature; however, BL25 has a higher MFFT. Surprisingly, the film made from the BL25 latex develops much less stress than the AL25 film despite having a higher T_g core and higher MFFT. This unexpected behavior may be the result of increased polymer compatibility between the core and shell polymers in BL25, allowing greater polymer mobility and faster polymer relaxation as stress builds in the film. Stress relaxation in the BL25 film also occurs gradually after the maximum stress is reached; there is no apparent stress relaxation in the AL25 film.

Particle size is another important variable that has the potential to influence stress development. Figure 7.8 plots stress development curves for AL25 and AS25. The two particles have similar structure but have particle diameters of D_v = 146 nm and D_v = 63 nm, respectively. The maximum stress developed in these coatings appears to be independent of particle size. For a network of hard elastic particles, the maximum stress in the coating has been shown to be proportional to the capillary pressure in the liquid, or inversely proportional to the particle size.[43,61] A network of hard particles can support the maximum capillary pressure allowed by the pore structure; however, soft latex particles will deform under a much lower stress. The AL25 and AS25 samples are presumed to be extremely soft at room temperature (MFFT < 0°C), therefore these

particles may deform under very low capillary pressures. This may explain why stress development for these coatings is independent of particle size.

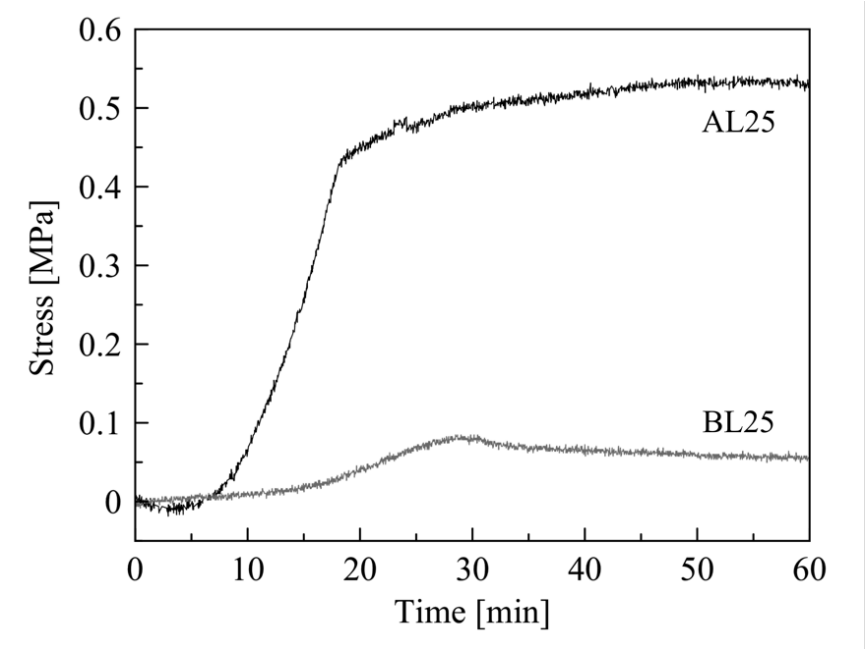

Figure 7.7: Effect of ΔT_g on the stress development profile for AL25 and BL25. BL25 has a smaller ΔT_g compared to AL25. The dried thicknesses of the films are approximately 80 μm.

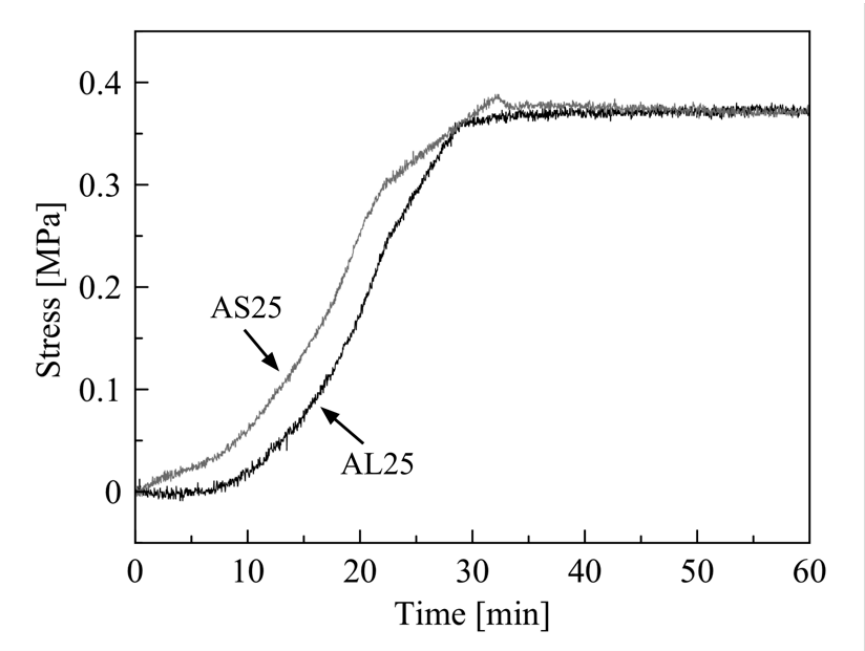

Figure 7.8 Effect of particle size on the stress profiles for AL25 and AS25. AL25 and AS25 have D_v=146 nm and D_v= 63 nm, respectively. The dried thicknesses of the coatings are approximately 80 μm.

7.3.4 *Paint Performance*

This section investigates how the film formation and stress development behavior of the latex-only coatings relate to the performance of the particles in a practical paint formulation. Table 7.4 summarizes some of the key paint performance data that was found for the core-shell particle paints. The gloss performance of a coating is an important measure of the appearance of the paint, which relates directly to the surface roughness of the film. Block resistance is a key performance requirement for gloss and semi-gloss paints and is often viewed as an indication of film hardness. Blocking is the tendency for painted films to stick together; films that display good block resistance can be separated from each other without compromising the integrity of the films. Scrub resistance is another key parameter that is related to the durability of the coating. AL35-

P and AL50-P (the –P denotes the particles in a paint formulation) do not form continuous films upon drying; therefore, gloss readings and block resistance tests were not conducted for these samples.

Table 7.4 Paint Performance Data

Sample ID*	20° Gloss	Block Resistance		Scrub Resistance
	[1-100]	1d - RT	1d - ET	[%]
AL25-P	44.5	9	7	32
AL35-P		Poor film formation		27
AL50-P		Poor film formation		14
AS25-P	49.6	9	8	20
BL25-P	51.3	9	7	100
CL50-P	43.0	10	7	78
CS50-P	54.7	9	7	136

*-P is used to denote the paint formulated with the latex types listed in Table 7.1

As shown in Section 7.3.2, smaller particles sizes display better film formation and reduce the surface roughness of the dried films. Two sets of the test paints investigated here have the latex particle size as the only variable. The results clearly show that smaller latex particles produce higher gloss paint films. The AS25-P sample produced a film with a 20º-gloss value 5-units higher than for AL25-P sample. For the other pair, CS50-P and CL50-P, the 12-unit difference is even more substantial. The CS50 particles displayed a respectable 20º-gloss performance in the mid-50s in the gloss paint formulation. The improvements in gloss performance are consistent with the calculated RMS roughness values measured for the latex films by AFM (Table 7.3).

All of the paint formulations in this study displayed good block resistance with scores greater than 7. The enhanced block resistance of the films can be attributed to the

soft-core/hard-shell morphology. The high T_g polymer in the shell creates a harder film surface for the bulk film, and also restricts interdiffusion between painted surfaces in contact with each other. The AL25-P, BL25-P, and AS25-P formulations demonstrate that good block resistance can be achieved simultaneously from a self-film-forming composite latex.

The latex materials investigated in this study show a wide range of performance in the scrub resistance test. An analysis of the experimental results using JMP recognizes that particle size, shell ratio, and core T_g are the statistically important parameters. The beneficial effect of smaller particle size is understandable because smaller particles display better film formation (smoother films, lower MFFT), which increases the strength of the network and helps improve durability. CL50-P and CS50-P differ only in latex particle size, but the scrub performance of the CS50-P film is nearly twice that of the CL50-P film. The effects of latex particle size on scrub resistance were not realized in the AL25-P and AS25-P films. This effect may be due in part to the residual stress in the film after drying.

Internal stress in the film negatively influences the adhesion of the film to the substrate,[125] which will directly affect the scrub performance. The correlation between internal stress in the film and scrub resistance is found in the AL25-P/AS25-P pair. The two latexes used in these paints have almost identical stress development profiles (Figure 7.8) and both exhibit poor scrub resistance. This is surprising because they are expected to undergo complete film formation at room temperature as their MFFTs are both <0°C. For another comparison, the BL25 film showed a lower residual stress than the AL25

film (Figure 7.7), consequently BL25-P paint exhibits much better scrub resistance. The BL25 particles also have a higher core T_g, which gives the film a higher elastic modulus and increased mechanical strength, which also contributes to the enhanced scrub resistance of the paint film.

7.4 *Summary*

In this Chapter, the film formation behavior of a series of soft-core/hard-shell latex samples was characterized using multiple experimental techniques (MFFT, cryoSEM, and AFM). The results were then correlated with performance of the core-shell latex particles in a practical paint formulation. CryoSEM revealed that a composite latex undergoes the typical film formation sequence and displayed the importance of morphology on wet film microstructure development. The film formation behavior, as investigated through MFFT and AFM experiments, was enhanced for core-shell particles with thinner (hard) shells, lower TV_s, and smaller particle sizes. A modified cantilever deflection technique, using walled cantilevers, was used to investigate the influence of particle morphology on the evolution of stress in the coating during drying. The stress development results show that latex morphologies with a thicker hard shell tend to crack, not due to high stress, but rather from restricted deformation and limited strength development in the particle network during drying. Results from the various techniques experimental techniques are consistent and correlate with the performance of the core-shell particles in a practical paint formulation. The composite particles displayed good performance for several paint properties including gloss and scrub resistance. This work

advances the understanding of the film formation process for core-shell latex particles and reveals the implications of particle morphology on the end-use properties of the paint.

Chapter 8

SUMMARY AND FUTURE DIRECTIONS

8.1 *Summary*

This work presented in this thesis develops connections between stress and structure development in particle-based coatings during drying. Walled cantilevers were shown to suppress lateral drying and increase drying uniformity for particle-based coatings. However, even with walled cantilevers some non-uniformity can remain as a result of contact line pinning at the wall. When extreme uniformity was achieved, stress measurement results were be combined with characterization of the coating microstructure using cryoSEM to reveal the mechanisms of stress development during drying in hard particle coatings. The uniformity achieved with the walled cantilevers also makes the interpretation of stress measurement results easier as complications due to lateral drying are removed.

Stress development in latex particle coatings was also investigated with the cantilever deflection technique using walled cantilevers. Stress development was found to be influenced by the particle composition (i.e. T_g), particle morphology (i.e. homogeneous, composite), and the addition of coalescing aids. The film formation

behavior was also investigated using a variety of characterization techniques including (MFFT, AFM, and cryoSEM). The film formation behavior was also strongly influenced by the particle composition and particle morphology as well as the particle size. The film formation and stress measurement results from the latex-only films of soft core-hard shell latex particles were correlated to the performance of the particles in a practical paint formulation. Several practical performance tests were conducted on the paint films (gloss, scrub resistance, block resistance) and the results were found to be consistent with the film formation behavior and the stress in the final coating.

The use of walled cantilevers provides a robust experimental technique capable of suppressing non-uniform drying. Likewise, with cryoSEM, the intermediate stages of the drying process (i.e. when the coating is still wet) can be imaged directly. By combining these technique a deeper understanding of how stress develops in particle-based is achieved. Moving forward, these techniques can be used to explore stress development for more complex coatings systems.

8.2 *Future Considerations*

8.2.1 *Crack Development and Fracture Toughness in Coatings*

The prevalence and importance of cracking in particle-based coatings provides motivation for further study. The cracking behavior in coatings has been widely studied for various coatings systems (ceramic films, latex films, etc.).[93,95,96,104,108] Cracks develop in coatings that exceed a critical cracking thickness (CCT), above which the

coatings crack spontaneously upon drying.[93,134] In brittle films, the CCT is expected to follow the dependence:[134]

$$CCT = \left(\frac{K_{IC}}{1.4\sigma}\right)^2 \tag{8.1}$$

where σ is the stress at cracking, and K_{IC} is the mode I fracture toughness. The fracture toughness of the coating is related to the mechanical properties of the film, which will depend on variables like particle size, particle interdiffusion, and binder content. Determining the effect of these variables on the fracture toughness can be accomplished by measuring the critical stress and the critical cracking thickness simultaneously.

Using the walled cantilevers described in this thesis, a uniform drying condition can be achieved and stress measurements can be made without the complications of lateral drying. The increased drying uniformity will provide a more accurate measurement of the critical cracking stress in the coating. Likewise, the uniform coating thickness will provide a good measurement of the CCT. This method provides an accurate way to measure the fracture toughness of the coating and affords the ability to investigate the influence of coating variables on the fracture toughness.

8.2.2 *Stress Development in Multi-Layer Coatings*

The coatings investigated in this thesis were simple, single-layer coatings. However, in practice most industrial coatings are much more complex and may include several coating layers. Understanding how stress develops in a single layer is only one aspect of the overall behavior of a multi-layer system. It is also important to understand how these coatings layers interact and how stress is distributed. Shrinkage of the coating

causes stress development only when that shrinkage is constrained by the substrate. The "substrate" in a multi-layer coating system may not be rigid; for instance, the substrate may be elastomeric, which could reduce shrinkage of the top-layer through viscous flow.

To study how stress development is affected, the relevant variables would be the modulus of the substrate (mechanical behavior), the relative thicknesses of the substrate and coatings, the drying conditions, and the ordering of the coating layers.

References

(1) Keddie, J. L.; Routh, A. F. *Fundamentals of Latex Film Formation*; 2010.

(2) Steward, P. a; Hearn, J.; Wilkinson, M. C. An Overview of Polymer Latex Film Formation and Properties. *Adv. Colloid Interface Sci.* **2000**, *86*, 195–267.

(3) Prevo, B. G.; Hon, E. W.; Velev, O. D. Assembly and Characterization of Colloid-Based Antireflective Coatings on Multicrystalline Silicon Solar Cells. *J. Mater. Chem.* **2007**, *17*, 791.

(4) Robertson, J. Ultrathin Carbon Coatings for Magnetic Storage Technology. *Thin Solid Films* **2001**, *383*, 81–88.

(5) Shukla, A.; Fuller, R. C.; Hammond, P. T. Design of Multi-Drug Release Coatings Targeting Infection and Inflammation. *J. Control. Release* **2011**, *155*, 159–166.

(6) Payne, J. Stress Evolution in Solidifying Coatings, University of Minnesota, 1998.

(7) Vaessen, D. Stress and Structure Development in Polymeric Coatings, University of Minnesota, 2001.

(8) Jindal, K. Stress Development in Particulate, Nano-Composite and Polymeric Coatings, University of Minnesota, 2009.

(9) Crawford, K. Microstructure Formation of Complex Latex Coatings, 2011.

(10) Ma, Y.; Davis, H. T.; Scriven, L. E. Microstructure Development in Drying Latex Coatings. *Prog. Org. Coatings* **2005**, *52*, 46–62.

(11) Sutanto, E.; Ma, Y.; Davis, H. T.; Scriven, L. E. Cryogenic Scanning Electron Microscopy of Early Stages of Film Formation in Drying Latex Coatings. *ACS Symp. Ser. Film Form. Coatings* **2001**, 174–192.

(12) Gong, X.; Ted Davis, H.; Scriven, L. E. Role of van Der Waals Force in Latex Film Formation. *J. Coatings Technol. Res.* **2008**, *5*, 271–283.

(13) Ge, H. Microstructure Development in Latex Coatings: High-Resolution Cryo-Scanning Electron Microscopy, University of Minnesota, 2005.

(14) Luo, H.; Cardinal, C. M.; Scriven, L. E.; Francis, L. F. Ceramic Nanoparticle/monodisperse Latex Coatings. *Langmuir* **2008**, *24*, 5552–5561.

(15) Cardinal, C. M. Drying Regime Maps for Particulate Coatings. **2010**, *56*, 2769–2780.

(16) Roberts, C. C.; Francis, L. F. Drying and Cracking of Soft Latex Coatings. *J. Coatings Technol. Res.* **2013**, *10*, 441–451.

(17) Lewis, J. A. Colloidal Processing of Ceramics. *J. Am. Ceram. Soc.* **2000**, *83*, 2341–2359.

(18) Brown, G. L. Formation of Films from Polymer Dispersions. *J. Polym. Sci.* **1956**, *22*, 423–434.

(19) Smith, C. P. Control of Biner Migration in Nonwoven Web Bonding. *TAPPI J.* **1993**, *76*, 183–186.

(20) Hagiwara, H.; Suszynski, W. J.; Francis, L. F. A Raman Spectroscopic Method to Find Binder Distribution in Electrodes during Drying. *J. Coatings Technol. Res.* **2013**, *11*, 11–17.

(21) Routh, A. F.; Zimmerman, W. B. Distribution of Particles during Solvent Evaporation from Films. *Chem. Eng. Sci.* **2004**, *59*, 2961–2968.

(22) Denkov, N. D.; Velev, O. D.; Kralchevsky, P. A.; Ivanov, I. B.; Yoshimura, H.; Nagayama, K. Two-Dimensional Crystallization. *Nature* **1993**, *361*, 26.

(23) Scherer, G. W. Theory of Drying. *J. Am. Ceram. Soc.* **1990**, *73*, 3–14.

(24) Berg, J. C. *An Introduction to Interfaces & Colloids: The Bridge to Nanoscience*; World Scientific: Hackensack, NJ, 2010.

(25) Arlinghaus, E. G. Microflows, Pore and Matrix Evolution in Latex Coatings, University of Minnesota, 2004.

(26) Haines, W. B. Studies in the Physical Properties of Soils: IV. A Further Contribution to the Theory of Capillary Phenomena in Soil. *J. Agric. Sci.* **1927**, *17*, 264.

(27) Lampenscherf, S.; Pompe, W.; Wilkinson, D. S. Stress Development Due to Capillary Condensation in Powder Compacts: A Two-Dimensional Model Study. **2000**, *40*, 1333–1340.

(28) Pekurovsky, L. A.; Scriven, L. E. On Capillary Forces and Stress in Drying Latex Coating. **2001**, 27–40.

(29) Holl, Y.; Keddie, J. L.; Mcdonald, P. J.; Winnik, W. A. Drying Modes of Polymer Colloids. **2001**, 2–26.

(30) Winnik, M. Latex Film Formation. *Curr. Opin. Colloid Interface Sci.* **1997**, *2*, 192–199.

(31) Vanderhoff, J. W.; Tarkowski, H. L.; Jenkins, M. C.; Bradford, E. B. Theoretical Consideration of the Interfacial Forces Involved in the Coalescence of Latex Particles. *J. Macromol. Chem.* **1966**, *1*, 361–397.

(32) Dillon, R. E.; Matheson, L. A.; Bradford, E. B. Sintering of Synthetic Latex Particles. *J. Colloid Sci.* **1951**, *6*, 108–117.

(33) Sheetz, D. P. Formation of Films by Drying of Latex. *J. Appl. Polym. Sci.* **1965**, *9*, 3759–3773.

(34) Eckersley, S. T.; Rudi. Mechanism of Film Formation from Polymer Latexes. *J. Coatings Technol.* **1990**, *62*, 89–100.

(35) Dobler, F.; Pith, T.; Lambla, M.; Holl, Y. Coalescence Mechanisms of Polymer Colloids. *J. Colloid Interface Sci.* **1992**, *152*, 1–11.

(36) Sperry, P. R.; Snyder, B. S.; O'Dowd, M. L.; Lesko, P. M. Role of Water in Particle Deformation and Compaction in Latex Film Formation. *Langmuir* **1994**, *10*, 2619–2628.

(37) Eckersley, S. T.; Rudin, A. Drying Behavior of Acrylic Latexes. *Prog. Org. Coatings* **1994**, *23*, 387–402.

(38) Mason, G. Formation of Films from Lattices a Theoretical Treatment. *Br. Polym. J.* **1973**, *5*, 101–108.

(39) Routh, A. F.; Russel, W. B. A Process Model for Latex Film Formation: Limiting Regimes for Individual Driving Forces. *Langmuir* **1999**, *15*, 7762–7773.

(40) Routh, A. F.; Russel, W. B. Deformation Mechanisms during Latex Film Formation: Experimental Evidence. *Ind. Eng. Chem. Res.* **2001**, *40*, 4302–4308.

(41) Gonzalez, E.; Paulis, M.; Barandiaran, M. J.; Keddie, J. L. Use of a Routh-Russel Deformation Map to Achieve Film Formation of a Latex with a High Glass Transition Temperature. *Langmuir* **2013**, *29*, 2044–2053.

(42) Deegan, R.; Bakajin, O.; Dupont, T.; Huber, G. Capillary Flow as the Cause of Ring Stains from Dried Liquid Drops. *Nature* **1997**, 827–829.

(43) Chiu, R. C.; Cima, M. J. Drying of Granular Ceramic Film: II, Drying Stress and Saturation Uniformity. *J. Am. Ceram. Soc.* **1993**, *76*, 2769–2777.

(44) Routh, A. F.; Russel, W. B. Horizontal Drying Fronts during Solvent Evaporation from Latex Films. *AIChE J.* **1998**, *44*, 2088–2098.

(45) Vanderhoff, J. W.; Bradford, E. B.; Carrington, W. K. The Transport of Water through Latex Films. *J. Polym. Sci. Polym. Symp.* **1973**, 155–174.

(46) Hwa, J. C. H. Mechanism of Film Formation from Lattices. Phenomenon of Flocculation. *J. Polym. Sci. Part A* **1964**, *2*, 785–796.

(47) Winnik, 1996 Latex Blends an Aproach to Low VOC Coatings.pdf.

(48) Parisse, F.; Allain, C. Drying of Colloidal Suspension Droplets: Experimental Study and Profile Renormalisation. *Langmuir* **1997**, *13*, 3598–3602.

(49) Salamanca, J. M.; Ciampi, E.; Faux, D. A.; Glover, P. M.; Mcdonald, P. J.; Routh, A. F.; Peters, A. C. I. A.; Satguru, R.; Keddie, J. L. Lateral Drying in Thick Films of Waterborne Colloidal. **2001**, 3202–3207.

(50) Okubo, M.; Takeya, T.; Tsutsumi, Y.; Kadooka, T.; Matsumoto, T. Asymmetric Porous Emulsion Film. *J. Polym. Sci. Polym. Chem. Ed.* **1981**, *19*, 1–8.

(51) Price, K. K.; McCormick, A. V; Francis, L. F. CryoSEM Investigation of Latex Coatings Dried in Walled Substrates. *Langmuir* **2012**, *28*, 10329–10333.

(52) Hoffman, R. W. Stress Distributions and Thin Film Mechanical Properties. *Surf. Interface Anal.* **1981**, *3*, 62–66.

(53) Lei, H.; Payne, J. A.; Mccormick, A. V; Francis, L. F.; Gerberich, W. W.; Scriven, L. E. Stress Development in Drying Coatings. **2001**, 1000–1013.

(54) Stoney, G. The Tension of Metallic Films Depositted by Electrolysis. *Proccedings R. Soc. London. Ser. A, Contain. Pap. a Math. Phys. Character* **1909**, *82*, 172–175.

(55) Corcoran, E. M. Determining Stresses in Organic Coating Using Plate Beam Defletction. *J. Paint Technol.* **1969**, *41*, 635–640.

(56) Payne, J. A.; McCormick, A. V.; Francis, L. F. In Situ Stress Measurement Apparatus for Liquid Applied Coatings. *Rev. Sci. Instrum.* **1997**, *68*, 4564.

(57) König, A. M.; Johannsmann, D. Stress Fluctuations in Drying Polymer Dispersions. *Langmuir* **2010**, *26*, 9437–9441.

(58) Guo, J. J.; Lewis, J. A. Aggregation Effects on the Compressive Flow Properties and Drying Behavior of Colloidal Silica Suspensions. *J. Am. Ceram. Soc.* **1999**, *82*, 2345–2358.

(59) Lei, H.; Francis, L. Stress Development in Drying Fibers and Spheres. *J. Appl. …* **2003**.

(60) Petersen, C.; Heldmann, C.; Johannsmann, D. Internal Stresses during Film Formation of Polymer Latices. *Langmuir* **1999**, 7745–7751.

(61) Tirumkudulu, M.; Russel, W. Role of Capillary Stresses in Film Formation. *Langmuir* **2004**, *20*, 2947–2961.

(62) Martinez, C. J.; Lewis, J. Shape Evolution and Stress Development during Latex–Silica Film Formation. *Langmuir* **2002**, *18*, 4689–4698.

(63) Timoshenku, S. P.; Gere, J. M. *Theory of Elastic Stability*; McGraw-Hill Book Co., Inc: New York, 1961.

(64) Pechhold, W.; Mayer, U.; Raju, G. B.; Guillon, O. Piezo Rotary and Axial Vibrator (PRAV) Characterization of a Fresh Coating during Its Drying. *Rheol. Acta* **2011**, *50*, 221–229.

(65) Popov, E. P. *Mechanics of Materials*; Prentice Hall: Englewood Cliffs, NJ, 1952.

(66) Muller, T.; Walther, P.; Scheidegger, C.; Reichelt, R.; Muller, S.; Guggenheim, R. Cryo-Preparation and Planar Magentron Sputtering for Low-Temperature Scanning Electron-Microscopy. *Scanning Microsc.* **1990**, *1*, 863.

(67) Luo, H.; Scriven, L. E.; Francis, L. F. Cryo-SEM Studies of Latex/ceramic Nanoparticle Coating Microstructure Development. *J. Colloid Interface Sci.* **2007**, *316*, 500–509.

(68) Ge, H.; Suszynski, W. J.; Davis, H. T.; Scriven, L. E. New Controlled Environment Vitrification System for Preparing Wet Samples for Cryo-SEM. *J. Microsc.* **2008**, *229*, 115–126.

(69) Echlin, P. *Low-Temperature Microscopy and Analysis*; Plenum Press: New York, 1992.

(70) Ge, H.; Zhao, C.; Porzio, S.; Zhuo, L.; Davis, H. T.; January, R. V; Re, V.; Recei, M.; May, V. Fracture Behavior of Colloidal Polymer Particles in Fast-Frozen Suspensions Viewed by Cryo-SEM. *Macromolecules* **2006**, *39*, 5531–5539.

(71) Forrest, S. R. The Path to Ubiquitous and Low-Cost Organic Electronic Appliances on Plastic. *Nature* **2004**, *428*, 911–918.

(72) Soltman, D.; Subramanian, V. Inkjet-Printed Line Morphologies and Temperature Control of the Coffee Ring Effect. *Langmuir* **2008**, *24*, 2224–2231.

(73) Jung, Y.; Kajiya, T.; Yamaue, T.; Doi, M. Film Formation Kinetics in the Drying Process of Polymer Solution Enclosed by Bank. *Jpn. J. Appl. Phys.* **2009**, *48*, 031502.

(74) Choi, S.; Stassi, S.; Pisano, A. P.; Zohdi, T. I. Coffee-Ring Effect-Based Three Dimensional Patterning of Micro/nanoparticle Assembly with a Single Droplet. *Langmuir* **2010**, *26*, 11690–11698.

(75) Hu, H.; Larson, R. G. Marangoni Effect Reverses Coffee-Ring Depositions. *J. Phys. Chem. B* **2006**, *110*, 7090–7094.

(76) Truskett, V. N.; Stebe, K. J. Influence of Surfactants on an Evaporating Drop: Fluorescence Images and Particle Deposition Patterns. *Langmuir* **2003**, *19*, 8271–8279.

(77) Okuzono, T.; Kobayashi, M.; Doi, M. Final Shape of a Drying Thin Film. *Phys. Rev. E* **2009**, *80*, 021603.

(78) Kajiya, T.; Kobayashi, W.; Okuzono, T.; Doi, M. Controlling the Drying and Film Formation Processes of Polymer Solution Droplets with Addition of Small Amount of Surfactants. *J. Phys. Chem. B* **2009**, *113*, 15460–15466.

(79) Pauchard, L.; Abou, B.; Sekimoto, K. Influence of Mechanical Properties of Nanoparticles on Macrocrack Formation. *Langmuir* **2009**, *25*, 6672–6677.

(80) Juillerat, F.; Bowen, P.; Hofmann, H. Formation and Drying of Colloidal Crystals Using Nanosized Silica Particles. *Langmuir* **2006**, *22*, 2249–2257.

(81) Park, J.-H.; Cho, J.-H.; Park, W.; Ryoo, D.; Yoon, S.-J.; Kim, J. H.; Jeong, Y. U.; Lee, S.-Y. Close-Packed SiO2/poly(methyl Methacrylate) Binary Nanoparticles-Coated Polyethylene Separators for Lithium-Ion Batteries. *J. Power Sources* **2010**, *195*, 8306–8310.

(82) Mansoor, I.; Stoeber, B. PIV Measurements of Flow in Drying Polymer Solutions during Solvent Casting. *Exp. Fluids* **2011**, *50*, 1409.

(83) Roberts, C. C. Understanding Particulate Coating Microstructure Development, University of Minnesota, 2010.

(84) Grunlan, J. .; Ma, Y.; Grunlan, M. .; Gerberich, W. .; Francis, L. . Monodisperse Latex with Variable Glass Transition Temperature and Particle Size for Use as Matrix Starting Material for Conductive Polymer Composites. *Polymer (Guildf).* **2001**, *42*, 6913–6921.

(85) Buss, F.; Roberts, C. C.; Crawford, K. S.; Peters, K.; Francis, L. F. Effect of Soluble Polymer Binder on Particle Distribution in a Drying Particulate Coating. *J. Colloid Interface Sci.* **2011**, *359*, 112–120.

(86) Deegan, R.; Bakajin, O.; Dupont, T.; Huber, G.; Nagel, S.; Witten, T. Contact Line Deposits in an Evaporating Drop. *Phys. Rev. E. Stat. Phys. Plasmas. Fluids. Relat. Interdiscip. Topics* **2000**, *62*, 756–765.

(87) Sanders, J. V. Colour of Precious Opal. *Nature* **1964**, *204*, 1151–1153.

(88) Diao, J. J.; Xia, M. G. A Particle Transport Study of Vertical Evaporation-Driven Colloidal Deposition by the Coffee-Ring Theory. *Colloids Surfaces A Physicochem. Eng. Asp.* **2009**, *338*, 167–170.

(89) Chen, C. N.; Chen, C. P.; Dong, T.-Y.; Chang, T. C.; Chen, M. C.; Chen, H. T.; Chen, I. G. Using Nanoparticles as Direct-Injection Printing Ink to Fabricate Conductive Silver Features on a Transparent Flexible PET Substrate at Room Temperature. *Acta Mater.* **2012**, *60*, 5914–5924.

(90) Yan, Y.; Kang, S.-Z.; Mu, J. Preparation of High Quality Ag Film from Ag Nanoparticles. *Appl. Surf. Sci.* **2007**, *253*, 4677–4679.

(91) Yan, G.; Zhang, X.; Huang, P.; Wang, L.; Qi, F.; Feng, B. Influence of Deposition Time on the Morphology and Optical Properties of SiO2-ZnO Composite Photonic Crystals. *Chinese Sci. Bull.* **2011**, *56*, 562–566.

(92) Bardosova, M.; Dillon, F. C.; Pemble, M. E.; Povey, I. M.; Tredgold, R. H. Langmuir-Blodgett Assembly of Colloidal Photonic Crystals Using Silica Particles Prepared without the Use of Surfactant Molecules. *J. Colloid Interface Sci.* **2009**, *333*, 816–819.

(93) Chiu, R. C.; Garino, T. J.; Cima, M. J. Drying of Granular Ceramic Films: I, Effect of Processing Variables on Cracking Behavior. *J. Am. Ceram. Soc.* **1993**, *76*, 2257–2264.

(94) Price, K. K.; Wu, W.; Wood, K.; Kong, S.; McCormick, A.; Francis, L. F. Stress Development and Film Formation in Multiphase Composite Latexes. *J. Coatings Technol. Res.*

(95) Tirumkudulu, M. S.; Russel, W. B. Cracking in Drying Latex Films. *Langmuir* **2005**, *21*, 4938–4948.

(96) Yow, H. N.; Goikoetxea, M.; Goehring, L.; Routh, A. F. Effect of Film Thickness and Particle Size on Cracking Stresses in Drying Latex Films. *J. Colloid Interface Sci.* **2010**, *352*, 542–548.

(97) Yow, H. N.; Beristain, I.; Goikoetxea, M.; Barandiaran, M. J.; Routh, A. F. Evolving Stresses in Latex Films as a Function of Temperature. *Langmuir* **2010**, *26*, 6335–6342.

(98) Wedin, P.; Martinez, C. J.; Lewis, J. a; Daicic, J.; Bergström, L. Stress Development during Drying of Calcium Carbonate Suspensions Containing Carboxymethylcellulose and Latex Particles. *J. Colloid Interface Sci.* **2004**, *272*, 1–9.

(99) Bauer, C.; Cima, M.; Dellert, A.; Roosen, A. Stress Development During Drying of Aqueous Zirconia Based Tape Casting Slurries Measured by Transparent Substrate Deflection Method. *J. Am. Ceram. Soc.* **2009**, *92*, 1178–1185.

(100) Lewis, J. A.; Blackman, K. A.; Ogden, A. L.; Payne, J. A.; Francis, L. F. Rheological Property and Stress Devlopment during Drying of Tape-Cast Ceramic Layers. *J. Am. Ceram. Soc.* **1996**, *79*, 3225–3234.

(101) Lampenscherf, S.; Pompe, W. Mechanical Behaviour of Granular Ceramic Films during Drying. *Zeitschrift fur Met*. **1998**, *89*, 96–105.

(102) Man, W.; Russel, W. Direct Measurements of Critical Stresses and Cracking in Thin Films of Colloid Dispersions. *Phys. Rev. Lett*. **2008**, *100*, 198302.

(103) Lee, W. P.; Routh, A. F. Why Do Drying Films Crack? *Langmuir* **2004**, *20*, 9885–9888.

(104) Roberts, C. C.; Francis, L. F. Drying and Cracking of Soft Latex Coatings. *J. Coatings Technol. Res*. **2012**, *10*, 441–451.

(105) Nozawa, K.; Gailhanou, H.; Raison, L.; Panizza, P.; Ushiki, H.; Sellier, E.; Delville, J. P.; Delville, M. H. Smart Control of Monodisperse Stöber Silica Particles: Effect of Reactant Addition Rate on Growth Process. *Langmuir* **2005**, *21*, 1516–1523.

(106) Hopcroft, M. A.; Nix, W. D.; Kenny, T. W. What Is the Young's Modulus of Silicon? *J. Microelectromechanical Syst*. **2010**, *19*, 229–238.

(107) Holmes, D. M.; Vasant Kumar, R.; Clegg, W. J. Cracking During Lateral Drying of Alumina Suspensions. *J. Am. Ceram. Soc*. **2006**, *89*, 1908–1913.

(108) Holmes, D. M.; Tegeler, F.; Clegg, W. J. Stresses and Strains in Colloidal Films during Lateral Drying. *J. Eur. Ceram. Soc*. **2008**, *28*, 1381–1387.

(109) Keddie, J. Film Formation of Latex. *Mater. Sci. Eng*. **1997**, *21*, 101–170.

(110) Perera, D.; Van den Eynde, D. Considerations on a Cantilever (beam) Method for Measuring the Internal Stress in Organic Coatings. *J. Coatings Technol*. **1981**, *53*, 39–44.

(111) Perera, D.; Eynde, D. Vanden. Effect of Pigmentation on Internal Stress in Latex Coatings. *JCT/Journal coatings Technol*. **1984**, *56*, 47–53.

(112) Perera, D.; Eynde, D. Vanden. Effect of Organic Solvents on Internal Stress in Latex Coatings. *J. coatings Technol*. **1984**, 69–75.

(113) Fox, T. G.; Flory, P. J. Second-Order Transition Temperatures and Related Properties of Polystyrene. I. Influence of Molecular Weight. *J. Appl. Phys*. **1950**, *21*, 581.

(114) Keddie, J. L.; Meredith, P.; Jones, R. A. L.; Donald, A. M. Kinetics of Film Formation in Latex Studied with Ellipsometry and Environmental-SEM. *Macromolecules* **1995**, *28*, 2673–2682.

(115) Juhue, D.; Wang, Y.; Winnik, M. A.; Haley, F. Influence of a Coalescing Aid on Polymer Diffusion in Poly(butyl Methacrylate) Latex Films. *Makromol Chem Rapid Commun* **1993**, *14*, 345–349.

(116) Schroeder, W. F.; Liu, Y.; Tomba, J. P.; Soleimani, M.; Lau, W.; Winnik, M. a. Effect of a Coalescing Aid on the Earliest Stages of Polymer Diffusion in Poly(butyl Acrylate-Co-Methyl Methacrylate) Latex Films. *Polymer (Guildf).* **2011**, *52*, 3984–3993.

(117) Juhue, D.; Lang, J. Film Formation from Dispersion of Core-Shell Latex Particles. *Macromolecules* **1995**, *28*, 1306–1308.

(118) Kirsch, S.; Pfau, A.; Stubbs, J.; Sundberg, D. Control of Particle Morphology and Film Structures of Carboxylated Poly (n Butylacrylate)/poly (methyl Methacrylate) Composite Latex Particles. *Colloids and Surfaces* **2001**, *183-185*, 725–737.

(119) Schuler, B.; Baumstark, R.; Kirsch, S.; Pfau, a.; Sandor, M.; Zosel, a. Structure and Properties of Multiphase Particles and Their Impact on the Performance of Architectural Coatings. *Prog. Org. Coatings* **2000**, *40*, 139–150.

(120) Morgan, L. Multifeed Emulsion Polymers: The Effects of Monomer Feed Sequence and the Use of Seed Emulsion Polymers. *J. Appl. Polym. Sci.* **1982**, *27*, 2033–2042.

(121) Devon, M. J.; Gardon, J. L.; Roberts, G.; Rudin, A. Effects of Core-Shell Latex Morphology on Film Forming Behavior. *J. Appl. Polym. Sci.* **1990**, *39*, 2119–2128.

(122) Lee, D. I.; Ishikawa, T. The Formation of "inverted" Core-shell Latexes. *J. Polym. Sci.* **1983**, *21*, 147–154.

(123) Rajatapiti, P.; Dimonie, V. L.; El-Aasser, M. S.; Vratsanos, M. S. Effects of Compatibilizing Agents in Poly(n-butyl Acrylate)/poly(methyl Methacrylate) Composite Latexes. *J. Appl. Polym. Sci.* **1997**, *63*, 205–219.

(124) Santos, F. D. Dos; Fabre, P.; Drujon, X.; Meunier, G.; Leibler, L. Films from Soft-core/hard-shell Hydrophobic Latexes: Structure and Thermomechanical Properties. *J. Polym. Sci.* **2000**, *38*, 2989–3000.

(125) Perera, D. On Adhesion and Stress in Organic Coatings. *Prog. Org. Coatings* **1996**, *28*, 21–23.

(126) Perera, D. Internal Stress in Latex Coatings. *J. Coatings Technol.* **1984**, *56*, 111–118.

(127) König, A. M.; Bourgeat-Lami, E.; Mellon, V.; von der Ehe, K.; Routh, A. F.; Johannsmann, D. Dilational Lateral Stress in Drying Latex Films. *Langmuir* **2010**, *26*, 3815–3820.

(128) Sawyer, L.; Grubb, D.; Meyers, G. *Polymer Microscopy*; Third Edit.; Springer: New York, NY, 2008.

(129) Jensen, D.; Morgan, L. Particle Size as It Relates to the Minimum Film Formation Temperature of Latices. *J. Appl. Polym. Sci.* **1991**, *42*, 2845–2849.

(130) Mu, Y.; Qiu, T.; Li, X.; Guan, Y.; Zhang, S.; Li, X. Layer-by-Layer Synthesis of Multilayer Core-Shell Latex and the Film Formation Properties. *Langmuir* **2011**, *27*, 4968–4978.

(131) Meincken, M.; Sanderson, R. D. Determination of the Influence of the Polymer Structure and Particle Size on the Film Formation Process of Polymers by Atomic Force Microscopy. *Polymer (Guildf).* **2002**, *43*, 4947–4955.

(132) Kendall, K.; Padget, J. C. Latex Coalescence. *Int. J. Adhes. Adhes.* **1982**, *2*, 149–154.

(133) Goudy, A.; Gee, M.; Biggs, S.; Underwood, S. Atomic Force Microscopy Study of Polystyrene Latex Film Morphology : Effects of Aging and Annealing. *Langmuir* **1995**, *11*, 4454–4459.

(134) Evans, A. G.; Drory, M. D.; Hu, M. S. The Cracking and Decohesion of Thin Films. *J. Mater. Res.* **1988**, *3*, 1043–1049.

Appendix

MODIFICATION OF CORCORAN'S EQUATION FOR WALLED CANTILEVERS

When a coating is applied to a rigid substrate, stress developed during drying will cause the underlying substrate to behave like a plate. Improving upon the early work by Stoney[54], Corcoran[55] used plate theory to derive a relationship between the coating stress and the curvature or deflection of a coated cantilever beam. This analysis considers that the area of the cantilever beam is fully covered with the coating. In this paper, a walled cantilever design is used to prevent lateral drying and increase drying uniformity. However, the presence of the wall reduces the coated area of the cantilever beam. Using Corcoran's approach, a relationship is derived which accounts for the uncoated area of the cantilever beam. Yow et al.[96] proposed a similar relationship for the partially coated cantilevers without walls. To validate this correction factor, finite element analysis and thermal stresses were used to simulate the deflection of cantilevers with and without walls. It was found that this correction factor could be applied to correct the calculated stress values, therefore reducing the error in the calculation.

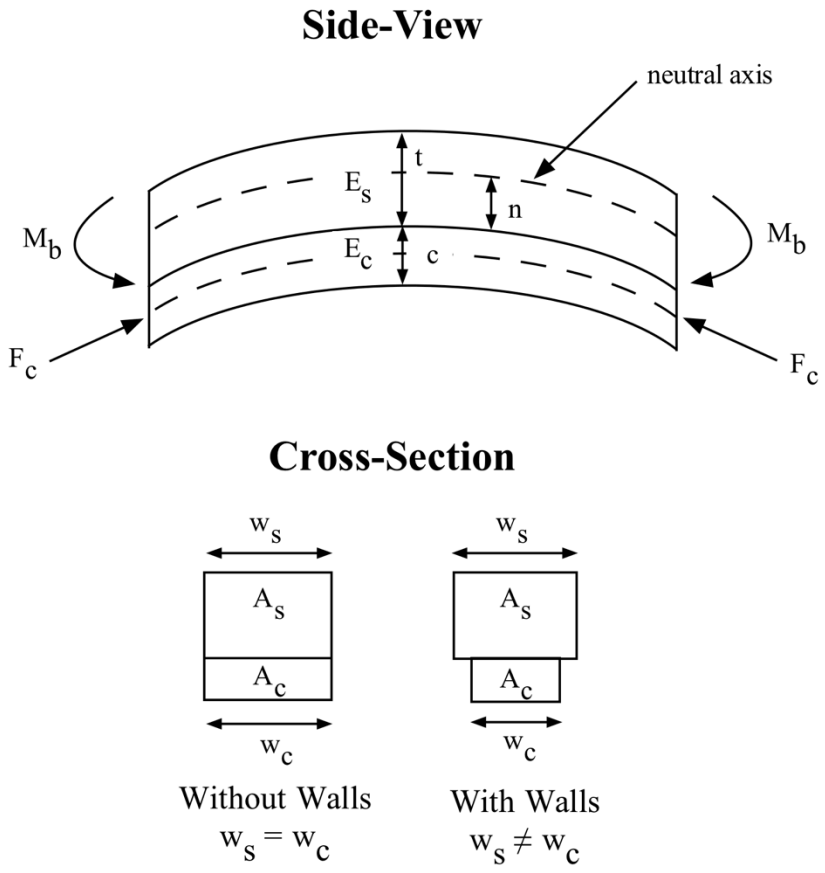

Figure A.1 Deflection in a composite beam due to stress in a coating. Cross-sections show the area of the coating with and without walls.

Using plate theory the curvature, *r*, of a thin plate can be expressed as:

$$\frac{1}{r} = \frac{M}{D_e(1+v)} \tag{A.1}$$

Where M is the bending moment per unit length, v is the Poisson's ratio, and D_e is the flexural rigidity plate, which can be expressed as:

$$D_e = \frac{Et^3}{12(1-v^2)} \tag{A.2}$$

where t, is the thickness of the substrate, and E is the Young's modulus of the plate. If a rectangular plate is rigidly clamped at one end, the radius of curvature for the composite beam can be expressed as[54]:

$$r = \frac{L^2}{2d} \tag{A.3}$$

Where d, is the deflection of the unclamped end, and L is the length of the unclamped section. Combining (A.1-A.3) yields:

$$d = \frac{6ML^2(1-v)}{Et^3} \tag{A.4}$$

Generally, a coating that is applied to a flat plate will cause the plate to bend due to stresses that arise during drying or curing. To relate the coating stress to the curvature of a composite beam, Corcoran[55] treated the problem as if the beam were being bent by equal bending moments acting on each end of the beam. The radius of curvature of the beam due to these bending moments is assumed to be equal to the radius of curvature that would arise due to stresses developed in the coating.

The bending moment, M_b, results from an average force, F_c, acting normal to the cross-section of the coating. The force is applied at a distance of (n + c/2) from the neutral axis, where n is the distance from the neutral axis to the surface of the substrate. Therefore,

$$M_b = F_c\left(n + \frac{c}{2}\right) \tag{A.5}$$

F_c, can be related to the average stress in the coating, σ_{avg}, and the cross-sectional area of the coating through the expression:

$$F_c = \sigma_{avg}(cw_c) \tag{A.6}$$

Where w_c, is the width of the coating and c is the coating thickness. The bending moment is then:

$$M_b = \sigma_{avg}(cw_c)\left(n + \frac{c}{2}\right) \tag{A.7}$$

In equation (A.4), M is expressed as a moment per unit length, which is equal to M_b/w_s, where w_s is the width of the substrate. Combining equations (A.4) and (A.7) :

$$\sigma_{avg} = \frac{Et^3 d}{6cL^2(1-v)(n+\frac{c}{2})}\left(\frac{w_s}{w_c}\right) \tag{A.8}$$

Assuming that the $n \approx t/2$, then:

$$\sigma_{avg} = \frac{Et^3 d}{3cL^2(1-v)(t+c)}\left(\frac{w_s}{w_c}\right) \tag{A.9}$$

Equation (A.9) gives an expression for the average stress in the coating. This expression reduces to Corcoran's equation[54] when the cantilever beam is fully coated, see Figure A.1. The stress, σ_{avg}, is the stress that would be measured from a measurement of the curvature or deflection of the substrate. However, this is not the true stress in the coating. The coating, which is applied to a rigid substrate, will be in a state of stress that is greater than the equilibrium stress σ_{avg}. As the beam bends, the coating relieves some of the stress through deformation. Corcoran[55] derived the full expression for the total stress, σ, by adding a second term to equation (A.9) based on a differential strain from the bent and unbent states:

$$\sigma = \frac{Et^3 d}{3cL^2(1-v)(t+c)}\left(\frac{w_s}{w_c}\right) + \frac{dE_c(t+c)}{L^2(1-v_c)} \tag{A.11}$$

where the subscripts s and c, represent the properties of the substrate and coating, respectively. However, the accurate use of Equation (A.11) requires that one knows the

mechanical properties of the coatings, which are difficult to measure experimentally. If $E_s >> E_c$ and $t >> c$, the second term of Equation (A.11) can be neglected without introducing significant error. Equation (A.11) is the same relationship derived by Corcoran except for the non-dimensional term w_s/w_c, which accounts for the non-coated areas of the beam. For cantilevers without walls, the cantilever surface is fully coated and $w_s = w_c$, see Figure A.1. But, when the wall is present, $w_s > w_c$, and the correction factor $w_s/w_c > 1$. When the coated area is reduced, the deflection of the cantilever is decreased, the correction factor compensates for the reduction in coated area.

Using finite element analysis (ANSYS) and thermal stresses the deflection of cantilever beams with and without PDMS walls were simulated. It was found that the deflection of the cantilever beam with walls was decreased not due to the wall material, but due to the reduction in coating area. Table A.1 summarizes the simulation results and lists the value of the corresponding correction factor.

Table A.1 Finite Element Analysis Data

Wall Width [*mm*]	Simulated Deflection [μm]	d_{walled}/d	*Correction factor (from simulation)*	*Derived Correction* (w_s / w_c)
0	8.3442	1.00	1.00	1.00
0.25	7.6359	.915	1.093	1.09
0.5	6.8361	.819	1.221	1.20
0.75	6.1237	.734	1.363	1.33
1.0	5.3752	.644	1.552	1.5

Table A.1 clearly shows that the correction factor (w_s / w_c) included in equation A.12 accounts for the reduction in deflection and corrects the calculated stress value.

This approach does not account for the uncoated area along the short edges of the cantilever, which accounts for only a small fraction of the reduced area.